THE COSMIC RAY SPECTRUM ABOVE 0.3 EeV

by

Kevin Davis Green

A dissertation submitted to the faculty of
The University of Utah
in partial fulfillment of the requirements for the degree of

Doctor of Philosophy

Department of Physics

The University of Utah

June 1992

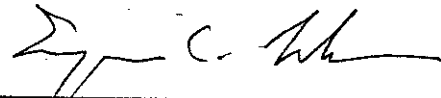THE UNIVERSITY OF UTAH GRADUATE SCHOOL

SUPERVISORY COMMITTEE APPROVAL
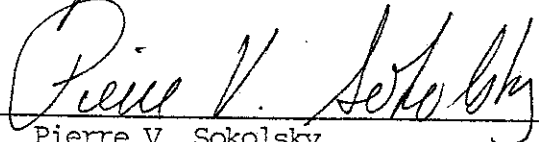
of a dissertation submitted by

Kevin D. Green

This dissertation has been read by each member of the following supervisory committee and by majority vote has been found to be satisfactory.
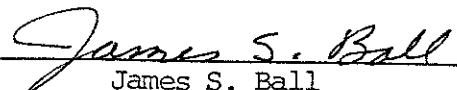
June 5, 1992

Chair: Eugene C. Loh

June 5, 1992

Pierre V. Sokolsky

6-6-1992

David B. Kieda

June 5, 1992

James S. Ball

6-5-92

Bill T. Sutherland

THE UNIVERSITY OF UTAH GRADUATE SCHOOL

FINAL READING APPROVAL

To the Graduate Council of the University of Utah:

I have read the dissertation of _____ Kevin D. Green _____ in its final
form and have found that (1) its format, citations and bibliographic style are consistent
and acceptable; (2) its illustrative materials including figures, tables, and charts are in
place; and (3) the final manuscript is satisfactory to the supervisory committee and is
ready for submission to The Graduate School.

June 5, 1992

Date

Eugene C. Loh
Chair, Supervisory Committee

Approved for the Major Department

P. Craig Taylor
Chair/Dean

Approved for the Graduate Council

B. Gale Dick
Dean of The Graduate School

ABSTRACT

The cosmic ray spectrum above 0.3 EeV is presented
using data from the Fly's Eye experiment. The data are
consistent with a power law spectrum with a spectral index
of -3.0. Extragalactic cosmic rays with energy above 60 EeV
should be attenuated through interaction with relic
blackbody photons. The data are consistent with this
hypothesis and in marginal disagreement with previous
experiments which show a continuation of the spectrum above
100 EeV.

TABLE OF CONTENTS

LIST OF TABLES

LIST OF FIGURES

LIST OF ABBREVIATIONS

EAS – extensive air shower.

EHCR – extremely high energy cosmic ray. A cosmic ray with energy above 1 EeV.

eV – electron volt. A unit of energy. 1 PeV=10^{15} eV and 1 EeV= 10^{18} eV

FE – Fly's Eye. Also used are FE1 and FE2 for Fly's Eye 1 and Fly's Eye 2 respectively.

OMB – ommatidial board.

UHCR – ultra high energy cosmic ray. A cosmic ray with Energy in the range 1 PeV – 1 EeV.

ACKNOWLEDGEMENTS

This dissertation represents only a small part of the Fly's Eye project, but it has benefitted from the efforts of everyone who has worked on the Fly's Eye over the years. It is impossible to thank everyone individually, and I wish to display gratitude for all those who I fail to mention. A good deal of thanks must go to my Committee, but I single out Eugene Loh and Pierre Sokolsky for guidance during my entire graduate studies. Next comes Michael Salamon who critiqued the manuscript as no one else could or did. In addition, thanks also must go to Rose Mary Baltrusaitis and George Cassiday for their support and advice early on. I single out George, who deserves special thanks. Next in line are Ron Cooper, Steve Corbato, Bruce Dawson, Jerry Elbert, Brian Fick, Peter Gerhardy, Dave Kieda, Dave Liebing, Paul Sommers. Also, thanks must go to Charmaine Goff, Sonny Ko, Al Larson, Jeremy Smith, Dave Steck, Stan Thomas, and Bob Wheeler. I also thank Bruce Emerson, Meng Zhi Luo, and Shu Xing Wang for their help. Also deserving mention are many undergraduate students who helped including Sherie Holfeltz, Brian Mecham, Scott Whalen. Thanks goes out to my family and friends as well. In particular, my brothers Kelley and Ross and sister Laura were very

supportive during a time when family support was especially appreciated. Thank you dear friends Carla Conover, Jeff McGough, Julie McFarland, and Tom Saxton.   All of you provided highly appreciated moral support at different stages in my graduate career.

CHAPTER 1

INTRODUCTION

The detailed shape of the cosmic ray spectrum (Figure 1.1) above 1 EeV (1 EeV = 10^{18} eV) is now a relatively old question, and, unfortunately, it has been an elusive one. The difficulty in measuring it becomes apparent when one notices that the flux of cosmic rays from above with energy $\simeq 10^{20}$ eV is on the order of 1 per square kilometer per steradian per century. The flux is a little easier to detect experimentally at 10^{18} eV, because there are $\simeq$ 1 per day through the same fiducial volume, but in either case, the observer must either have a very large detector or must be incredibly patient. Regardless, even with a relatively large detector, patience is a prerequisite, particularly at the highest energies.

The spectrum has some relevance to cosmological and astrophysical theory, however, so a precise measurement is a worthwhile endeavor from a scientific viewpoint, and many scientific groups have attempted to observe it. The Fly's Eye Group[1] has published preliminary versions of the spectrum,[2,3] but another update is in order, because further improvements to the detector have been made and more data have been taken.
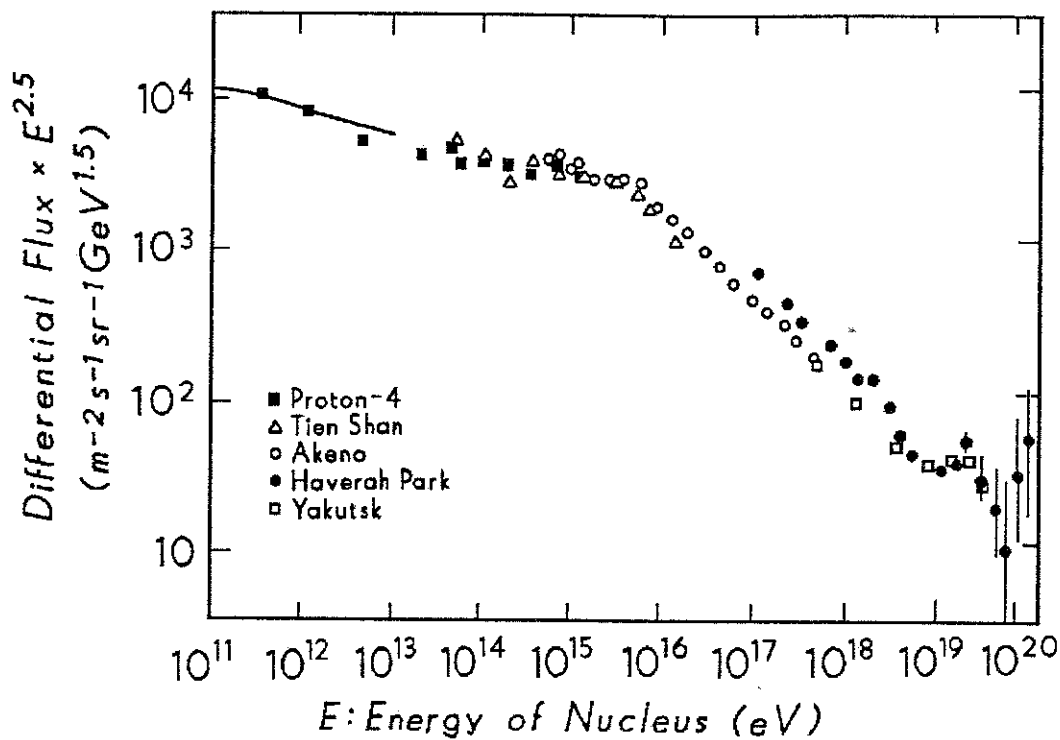
Figure 1.1—The cosmic ray spectrum. It has been similarly compiled by Sokolsky.[4]

This dissertation addresses the topic of the cosmic ray spectrum above 0.3 EeV. It reviews the past measurements of the spectrum, explains why a spectrum measurement is scientifically interesting, comments on the advantages of the Fly's Eye measurement over ground array techniques, describes details of the Fly's Eye, and updates the Fly's Eye's measurement of the spectrum of the highest known energy cosmic rays. It gives for the first time a spectrum from Fly's Eye stereo data (data taken in coincidence with

both Fly's Eye 1 and Fly's Eye 2) which provides an important systematic check of the spectral measurement.

Chapter 2 begins with a review of extremely high energy cosmic rays (EHCRs). Past experimental results and some expectations concerning these highest known energy cosmic rays are included. The chapter begins with a review of EeV energy cosmic ray properties measured by existing and past experiments, and it mentions relevant cosmic ray propagation models. In particular, the Greisen-Zatsepin Mechanism is discussed, because this is the most interesting problem at the highest energies (100 EeV).

Chapter 3 focuses on extensive air showers (EAS), because, it is the EAS that is detected and from which EHCR properties are inferred. This is an important topic, since difficulties in detection could explain why different groups obtain different answers. The ground array method of energy estimation is discussed as are the arrays that have been involved in EHCR physics. The other EAS detection technique for energies exceeding 10^{17} eV is air fluorescence and is the one employed by the Fly's Eye. It is now a well-established tool in EAS physics, though currently only one detector in the world takes advantage of it. The technique provides good EAS calorimetry, which is crucial to determining the energies of the most energetic cosmic rays.

The Fly's Eye detector(s) and its (their) operation are described in Chapter 4. Included is documentation of the major changes done over the years. The primary emphasis

however is on the aspects of operation relevant to EAS reconstruction, since a good description of the Fly's Eye detectors already exists.[1]

Fly's Eye reconstruction algorithms of data from detected EAS are the topic of Chapter 5. The goals of the discussion are to detail exactly how one determines the energy of an EAS detected by the Fly's Eye and to determine the energy resolution from Monte Carlo and stereo viewing techniques.

Finally, in Chapter 6, an update of the cosmic ray spectrum from the Fly's Eye data is given along with a discussion of the implications of the spectrum to the Greisen-Zatsepin hypotheses discussed in Chapter 2. As mentioned, this dissertation gives a spectrum from the stereo data set incorporating simultaneous data from both FE1 and FE2. It also includes the updated FE1 spectrum and incorporates data from previous publications and data taken more recently.

CHAPTER 2

EXTREMELY HIGH ENERGY COSMIC RAYS

How is nature capable of accelerating particles to the truly awesome energy of 10 EeV and higher? This is perhaps the most interesting question posed by extremely high energy cosmic rays (EHCRs). Some information on this problem of origin can be inferred from three measured properties: (1) the particle energy, (2) the arrival direction, and (3) the chemical composition. All of these are useful and are intricately related by different theories, so each of these properties are discussed briefly below.

2.1. EHCR Empirical Data

2.1.1. Spectrum

The cosmic ray spectrum (Figure 1.1) contains some remarkable features. Between $10^{13} - 10^{15}$ eV, the spectrum has a steep power law dependence of $E^{-2.7}$. There is a break in the slope somewhere between $10^{15}-10^{16}$ eV (generally called the "knee") while above this break, the spectrum drops with an even steeper power law of spectral index near -3.0 for at least two decades. It is a striking fact that the spectrum obeys power laws over many decades. Above 10 EeV, the slope is still uncertain due to the poor statistics.

For discussion purposes, it is best to divide the high end of the spectrum into three regions—the region near and above the "knee," the region from 10^{16} eV to 10^{18} eV, and the region above 10^{18} eV.

2.1.1.1 0.1<E<10.0 PeV

There have been many observations of a change in spectral slope in this region,[5,10] and the results show a break in the $2-6 \cdot 10^{15}$ eV region though it has been suggested that the actual position is even higher.[11] The difference of break energy between groups may be due to different methods of determining particle energy from the measured EAS parameters, and the situation is not resolved.

All claims of a "knee" to date have been from EAS detections. The more direct methods of determining spectral properties by balloon and satellite experiments have reached TeV energies,[12,13] but it is doubtful they will be extended to the "knee" and beyond any time soon given the small flux.

The "knee" energy has been interpreted as the energy at which cosmic rays are no longer trapped by magnetic fields within the galaxy and begin to leak out of it.[14] It can also be interpreted as the point at which the acceleration process changes.[15]

2.1.1.2 0.01<E<1.0 EeV

Relatively few have measured the spectrum in the region of $10^{16}-10^{18}$ eV,[6,9,16,17] and again, the results are not completely consistent. All experiments do show a spectral

steepening from 2.7 to 3.0 or higher, but they are slightly different in values of slope and normalization, and all are consistent with a spectral "desert," because no significant deviation from a simple power law has been resolved.

Table 2.1 summarizes spectral features in this region from more recent experiments. It is difficult to understand why the Moscow result is different in slope. The problem is "fundamental," because even the "raw" electron shower size intensities are different. Further, the Moscow spectrum has difficulty "lining up" with the measured spectra in the EeV region. The fact that their flux is too low is not fatal, for the normalization can change with different conversion factors from electron size to incident particle energy. Nonetheless, there is a significant discrepancy.

2.1.1.3 E>1.0 EeV

Figure 2.1(a)-(e) shows the most recent spectrum measurements from different experiments throughout the world, and Table 2.2 lists the spectral slopes. Some details of the different experiments can be found in Chapter 3. To date, the Fly's Eye and the Yakutsk spectra are the only ones that are based in one form or another on calorimetric energy estimation techniques with the Fly's Eye measurement being almost exclusively so. The others are based on EAS model assumptions (Chapter 3).

One agreement between most of the different experiments is that there appears to be a deviation from the $E^{-3.0}$ slope

Table 2.1. Differential slope β [$j(E) = aE^{-\beta}$] from the knee to 1.0 EeV from the different experiments done in this energy range. No systematic errors on the slope have been quoted.

Energy Range (PeV)	Group		
	Akeno	HP	Moscow
β:			
10.-100.	3.02±.05	–	3.3±.04
100-1000.	"	3.05±.05	–

Table 2.2. Differential slope β [$j(E) = aE^{-\beta}$] above 0.1 EeV from the different experiments done in this energy range. References are given in Figure 2.1.

Energy Range (EeV)	Group				
	FE(1985)	Yakutsk	Akeno	HP	Sydney
β:					
1.0-10.	2.94±.02	>3.0	3.39±.06	3.14±.05	3.19±.01
10.-50.	2.42±.27	< 3.0	2.0±.2	2.31±.10	2.99±.13
> 50	–	–	–	"	"

Spectra (E > 0.1 EeV)
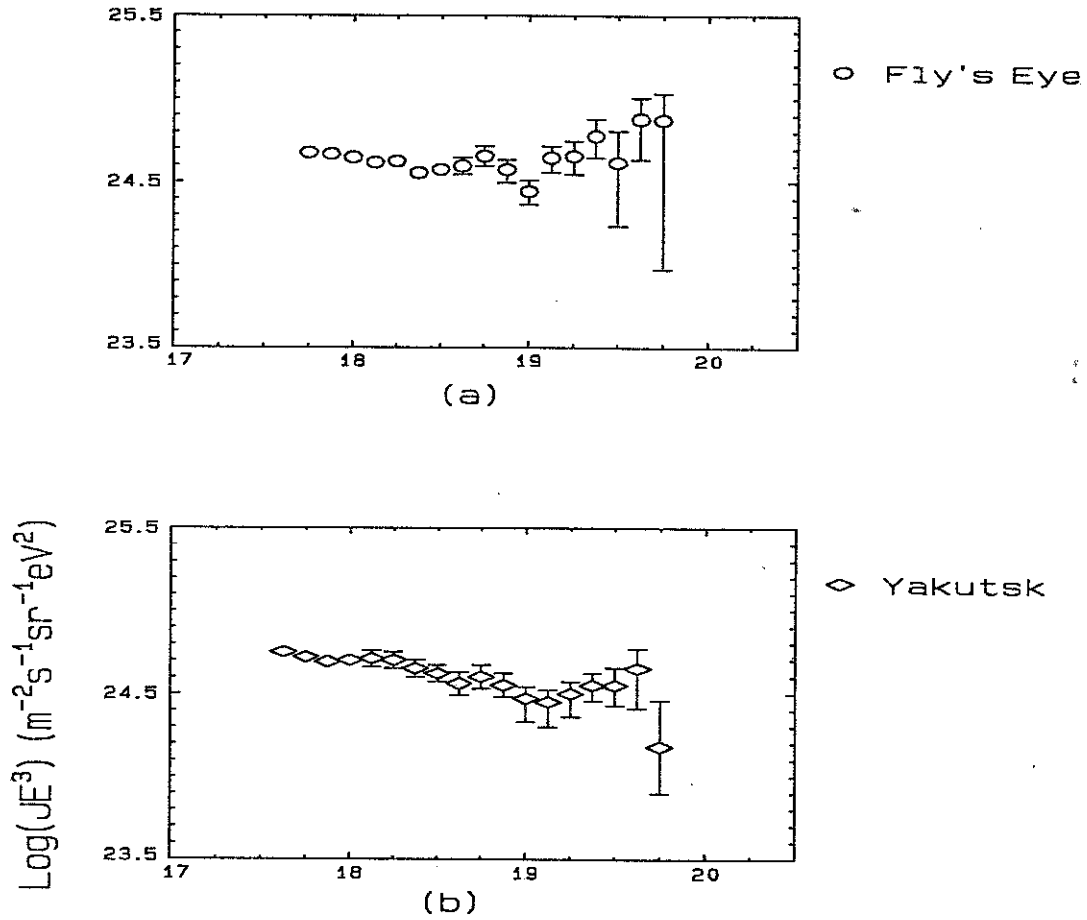
Figure 2.1—The differential cosmic ray spectrum above 0.1 EeV from (a) The Fly's Eye,[18] (b) Yakutsk,[19] (c) Akeno,[20] (d) Haverah Park,[21] and (e) Sydney.[22] There are three groups that see no events above $\simeq$ 80 EeV, while two others do. Not shown is the Volcano Ranch[23] spectrum that also claims there is a continuation in the spectrum above 100 EeV.

(c)

Log(E_0 eV)

△ Akeno

(d)

□ Haverah Park

(e)
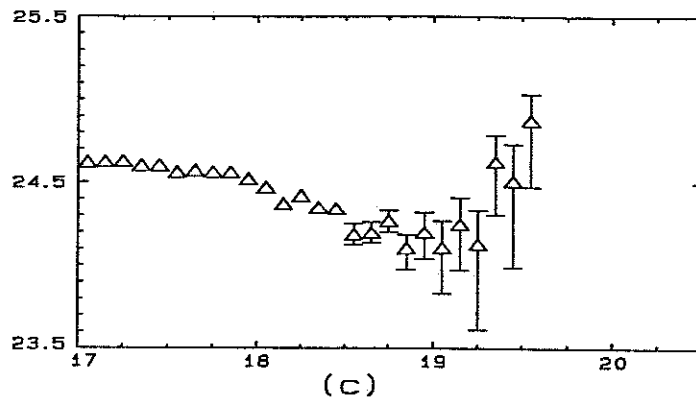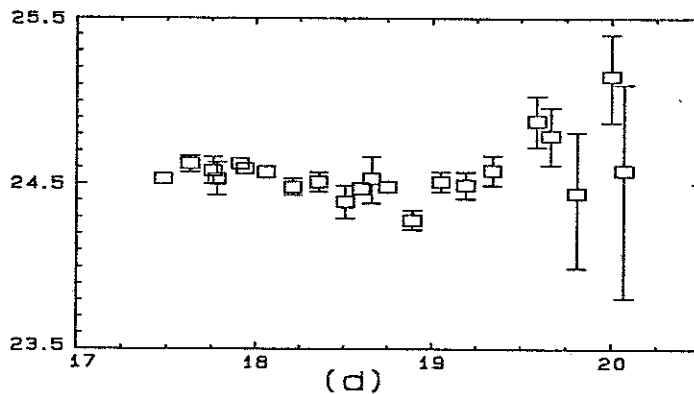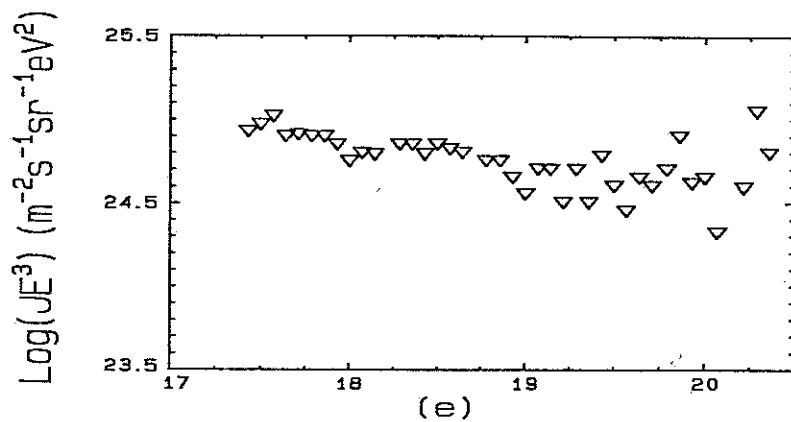
Log(E_0 eV)

▽ Sydney

Log(JE^3) (m^{-2}s^{-1}sr^{-1}eV^2)

in the neighborhood of 10 EeV and perhaps earlier. The results need to be discussed one by one.

The Fly's Eye first published results in 1985 showing a spectral slope of 2.94±.02 in the region 0.1 - 10 EeV. If a fit was made to data above 10 EeV, the slope was 2.42±.27. At that time, no events had an energy > 60 EeV, and 62 events were seen above 10 EeV which is consistent with the Greisen-Zatespin mechanism (see below). The spectrum was updated in 1987, and the spectral index steepened with the new analysis to ≈3.1. Data with E < 0.75 EeV were not included in the analysis, because it had been determined that the aperture calculation was most reliable above that energy. The highest energy event in that sample was 80 EeV.

The final Haverah Park spectrum is consistent with a spectral slope of 3.0 below 1.0 EeV but shows a slight spectral softening at 1.0 EeV from the 3.0 spectral index to 3.14±.05. If the true spectrum continues with a 3.0 slope, then from 3.5 to 10.0 EeV, they should have detected 380 events, but 303 events were detected giving a 3.9σ deficit.

Haverah Park also supports a spectral hardening above 40 EeV with 15 detected and 8.3 expected (prob=.012), though if one takes all events above 10 EeV, then there is a good agreement with a 3.0 slope (106 observed and 94.8 expected). Unlike the Fly's Eye data, there is no consistency with a cutoff. Their spectrum continues beyond 80 EeV with 5 events above that energy.

The Yakutsk data also are consistent with a cutoff around E < 100 EeV. There is a rise in slope above 10 EeV, and their highest energy particle is at 64 EeV. Assuming the Haverah Park Integral flux of $I(> 100$ EeV$) = 3^{+2}_{-1} \, 10^{-16}$ $m^{-2}s^{-1}sr^{-1}$ presented in 1985, they should have detected 5-6 showers above 100 EeV, so Yakutsk is also in mild contradiction with the Haverah Park data at the highest end.

At lower energies, recent mention[24] is made of a possible deviation of the spectral slope near 1.0 EeV in the Yakutsk dataset, and their data are in general consistency with the Haverah Park result in that region (see Figure 2.1), although the energy at which a change occurs is slightly different.

The Akeno group are newcomers to the EeV region. They reported a complex spectrum with a dip beginning at 1.0 EeV at the Moscow International Cosmic Ray Conference (ICRC) in 1987, but reported in the Adelaide ICRC (1990) that there is no significant deviation from 3.0 in the spectral slope above 10^{16} eV. They are consistent with a bump above 10 EeV, however, and detect no events above 100 EeV. This is not yet in contradiction with the Haverah Park measurement.

The Sydney group are in agreement with Haverah Park at the highest end. However, this detector unfortunately had problems with phototube afterpulsing which has made interpretation of their results difficult.

The Greisen-Zatsepin mechanism (Section 2.2) predicts a cutoff at an energy ≈ 60 EeV, so any conclusively

demonstrated extension of the spectrum above this region is very important. The fact that the different experiments have slightly different normalizations in the region of 1 EeV implies that calibration and possibly other systematic effects might still be prevalent in the different experiments which makes a simple cross-comparison of the different results difficult.

Despite the fact all experiments see some change, the "ankle" or "dip" or "bump" at 10 EeV is not yet an established feature of the spectrum. It could be an artifact of the limited statistics involved, or it could be "spill-up" from lower energies. The Fly's Eye data above 10 EeV in 1985 consisted of only 62 events. The final Haverah Park sample above 10 EeV is 106 events with only 15 above 40 EeV. Given the systematics in ground array measurements (Chapter 3), it is reasonable to say that the data are not inconsistent with a 3.0 spectral index.

2.1.2. Anisotropy

2.1.2.1 Large Scale Anisotropies

Directional anisotropies of EHCRs have been reported in the literature, but they are as yet not too convincing.[25,26] This is probably the most frustrating property of cosmic rays, but it gives us one property: the vast majority of the cosmic rays are charged particles whose directional information has been lost due to the magnetic fields

encountered during propagation. It also shows that the gamma-ray component from discrete sources is small.

The Fly's Eye has placed limits on large scale anisotropies.[27] No statistically significant anisotropy has been found on the large scale. Table 2.3 lists percentage excesses from six coarsly binned sky areas shown in Figure 2.2. The anisotropies for $E > 0.125$ EeV are plotted in Figure 2.3.

Wdowczyk and Wolfendale[28] propose a different type of anisotropy analysis to look specifically at the galactic plane as a possible extended source of cosmic rays. They propose using a model of form:

$$I(b) = I_0 \cdot [(1 - f_e) + f_e \exp(-b^2)] \tag{2.1}$$

where b is the galactic latitude in radians, f_e is a galactic latitude enhancement factor (a function of energy), $I(b)$ is the number of cosmic rays observed in the galactic latitude bin, and I_0 is the number expected in the isotropic background.

Fly's Eye data give little support for a galactic enhancement.[29] The Haverah Park data are consistent with $f_e = 0.3$, but there is no significant evidence for an enhancement.[30] The Fly's Eye upper limits on f_e are 0.06 ± 0.02 for $0.4 < E < 1.0$ EeV, 0.15 ± 0.21 for $1.0 < E < 3.0$ EeV, and 0.1 ± 0.3 for $3.0 < E < 10.0$ EeV. When interpreting these results, it is important to remember that the Fly's Eye does not view the Galactic center.

Table 2.3. Percentage excesses of anisotropy from 6 sky regions. N – North galactic pole, S – South galactic pole, C – galactic Center, A – galactic Anticenter, F – Forward along solar circle, B – Backward along solar circle. See Figure 2.2 for a pictorial explanation.

	Energy Region	
Direction(EeV)	.125–.50 EeV	0.50–32. EeV
N	−1.4±1.8 %	−1.6±2.2 %
S	2.2±4.8	9.3±4.4
C	−6.7±6.0	2.0±5.7
A	0.6±1.6	−2.5±1.8
F	0.6±1.2	0.4±1.8
B	8.7±16.1	13.7±12.1
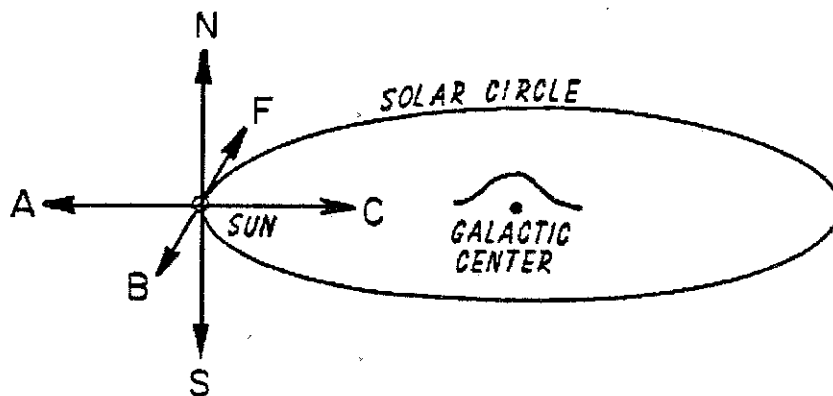
Figure 2.2—Pictorial representation of large scale bins for which directional anisotropies were obtained.
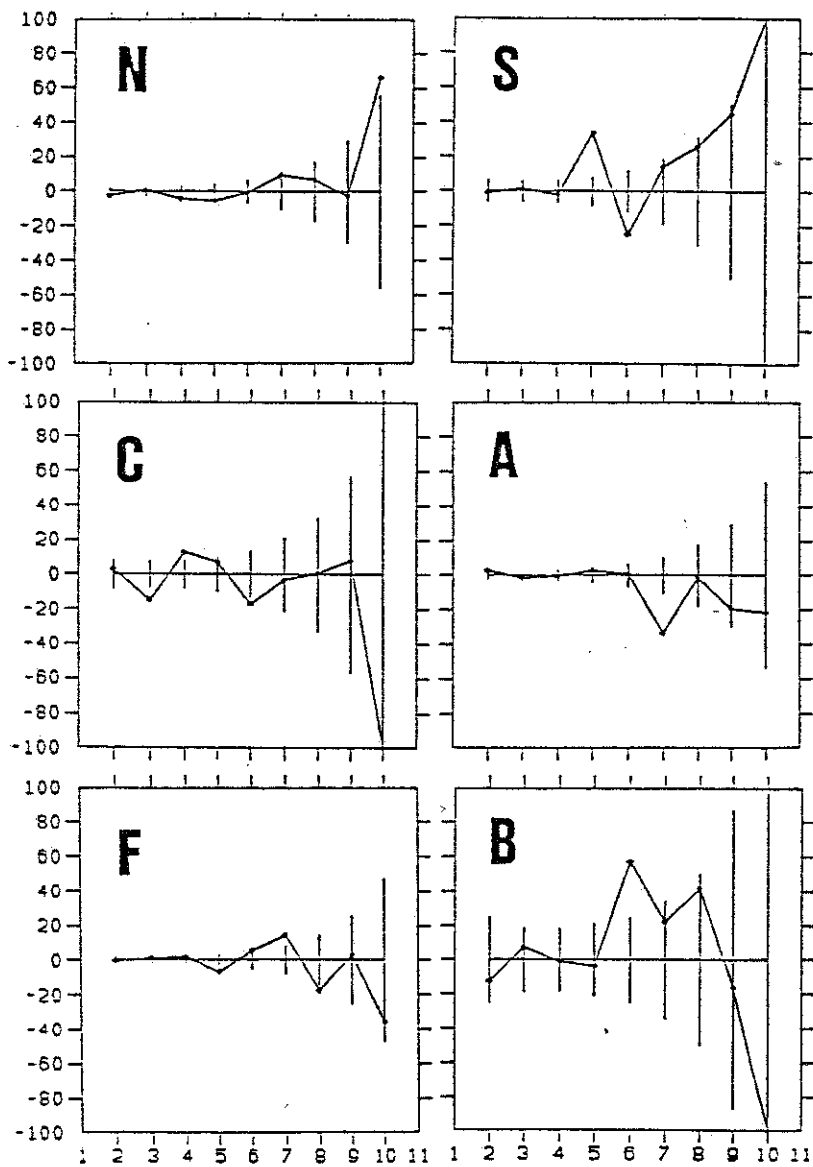
Figure 2.3—Coarse grain anisotropies as a function of energy.

Haverah Park does have some evidence (40%±20% based on a sample of 50 events) for an anisotropy from the direction normal to the galactic plane above 30 EeV, but no claim of statistically significance anisotropy is made.

The anisotropy results are puzzling. For ≈ 1 EeV protons originating in the galactic disk, there should be anisotropy in the galactic direction, because for 1 EeV protons, the Larmor radius is ≈ 1 kpc for residual fields of $\approx 10^{-6}$ Gauss. The composition could be heavy. An anisotropy would be absent until ≈ 10 EeV where data are scarce. It could also mean EHCRs originate outside our galaxy.

2.1.2.2 Point Sources

Weak point anisotropies have been detected in the ultra high energy (UHE) region of 10^{14} to 10^{16} eV, but it is important to point out that all such detections to date have been marginally statistically significant.[31,32] If these reported detections at PeV energies are not just statistical flukes, then as Hillas[6] showed, these PeV (1 PeV = $1 \cdot 10^{15}$ eV) sources (in particular Cygnus X-3) are good candidates for EeV cosmic ray acceleration.

The Fly's Eye group has reported an excess of cosmic ray particles with E > 0.5 EeV from the direction of Cygnus X-3—one of the PeV candidates.[33] The measured flux is $(2.0 \pm 0.6) \cdot 10^{-17}$ particles $cm^{-2}s^{-1}$, and has a probability of $6.4 \cdot 10^{-4}$ of being a random deviation from isotropy.

Recently, the Akeno group have also reported a 3.5σ excess of > 0.5 EeV showers from the same region[34] with a flux of $(1.8\pm0.7)\cdot10^{-17}$ $cm^{-2}s^{-1}$ above 0.5 EeV. The air showers that comprise the Akeno signal have normal muon content that would favor neutron primaries.

However, the Haverah Park Group[35] did not see an excess, which makes the experimental situation murky. At 95% confidence level, they quote an upper limit of $4\cdot10^{-18}$ particles $cm^{-2}s^{-1}$, though the limit is reduced to $8\cdot10^{-18}$ photons $cm^{-2}s^{-1}$ for γ-ray primaries. The difference in the limits for nucleons and γ-rays is due to a composition induced detector triggering bias.

The statistical significance of deviation from isotropy from either experiment is not overwhelming, and further confirmation of detection is needed before this EeV compact source candidate is established as a cosmic ray accelerator.

2.1.3. Composition

The cosmic ray compositions have been measured with good precision at much lower energies.[36] Around the knee and beyond, the composition is still not established. The Fly's Eye group has measured the shower X_{max} distribution, and the composition can be inferred from it.[37] From elaborate Monte Carlo calculations, showers from pure Fe nuclei of energy above 0.3 EeV detected by the Fly's Eye should have an average X_{max} value of 705 ± 3 g cm^{-2} and should have a width of 66 ± 2 (the large width due principly to

reconstruction errors). For pure protons, $<X_{max}>$ should be 803±2 g cm^{-2} and should have a width of 80±1 g cm^{-2}. The data have $<X_{max})$ = 690±3±20 g cm^{-2} and a width of 85±2 g cm^{-2}. The measured value of $<X_{max}>$ is low even for Fe, and the broad width is inconsistent with a single component model.

$<X_{max}>$ vs energy is plotted in Figure 2.4, while the distribution for E > 0.3 EeV is plotted in Figure 2.5. $<X_{max}>$ increases by 69±5 g cm^{-2} per decade of energy.

The composition is not known above 10^{19} eV, which is where it must be to fully test the Greisen-Zatsepin theory.

2.1.4 Conclusion

From the discussion above, it looks like there is still plenty to learn about EHCRs. There are disagreements on the spectral shape, there is one marginal source candidate, and the composition is not known. This leaves many challenges for the experimentalist and gives plenty of open ground for the theorists to roam.

2.2. EHCR Propagation and Origin: Spectrum Implications

Because the spectrum has significant impact on the theory of what happens to EHCRs during travel, the discussion will start with propagation. What happens to cosmic rays that travel intergalactic distances is different from those only traveling from some location inside the galaxy (from a source like Cygnus X-3 for example).
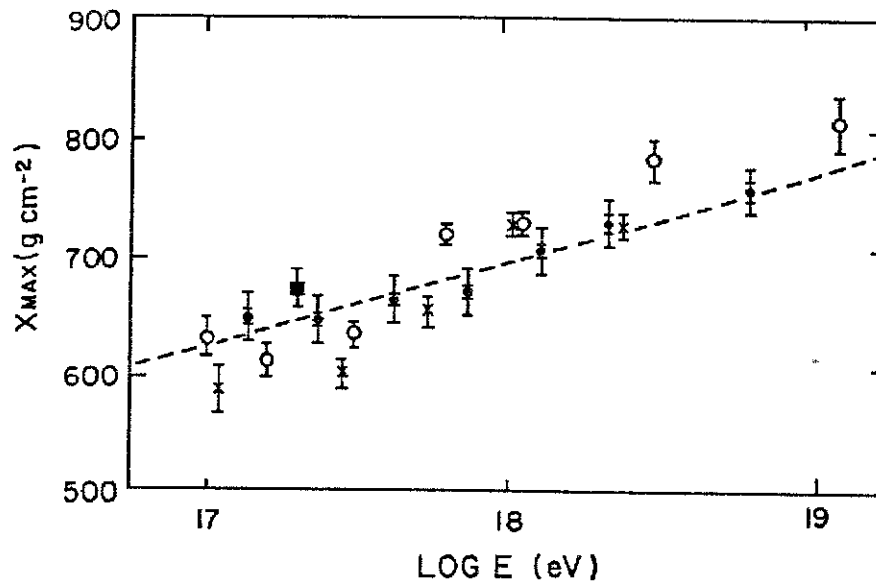
Figure 2.4—X_{max} Elongation as measured by the Fly's Eye and other experiments. See text for references.
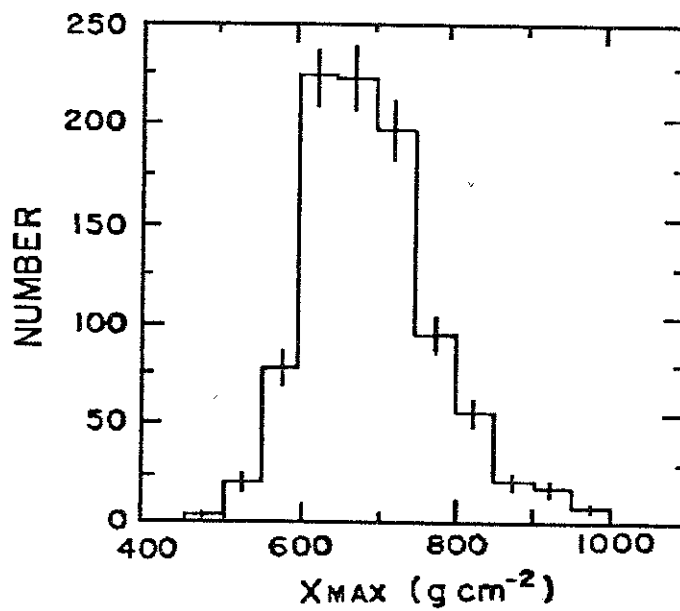
Figure 2.5—The distribution of X_{max} for stereo viewed showers above 0.3 EeV.

2.2.1. The Greisen-Zatsepin Mechanism

The measurement and confirmation of the 2.7°K blackbody radiation[38,39] was quickly realized by Greisen[40] and independently by Zatsepin and Kuz'min[41] to have an effect on cosmic rays if EHCRs are of extra-galactic origin. Both papers show that nucleons of energy > 100 EeV have enough energy to photoproduce a pion through the reaction

$$\gamma p \longrightarrow \Delta^+(1232) \longrightarrow n\pi^+$$
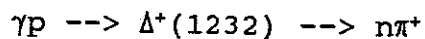
if one collides with a 2.7°K photon. (The cross section for this reaction peaks at $\simeq .5$ mbarn.) The end result implies 100 EeV cosmic rays will not survive propagation through the extra-galactic medium if (1) they originate far enough away, and (2) if the blackbody radiation is indeed universal.

A more detailed calculation of a proton propagating through the intergalactic medium has since been done by Stecker.[42] (Almost all of the physics, though, can be found in Greisen's seminal letter.) Stecker folded in the blackbody spectrum, the changing cross section, and the measured elasticity of the γ-p interaction. Figure 2.6 plots the proton lifetime and propagation distance for protons with energies > 10 EeV. The major conclusion from Stecker's analysis is that a 100 EeV proton could travel from the local supercluster (10-15 Mpc) essentially unattenuated, but not from distances beyond.

2.2.2. Cosmic Ray Spectra Propagation

Hill and Schramm[43] carried cosmic ray propagation one step further by numerically solving the transport equations
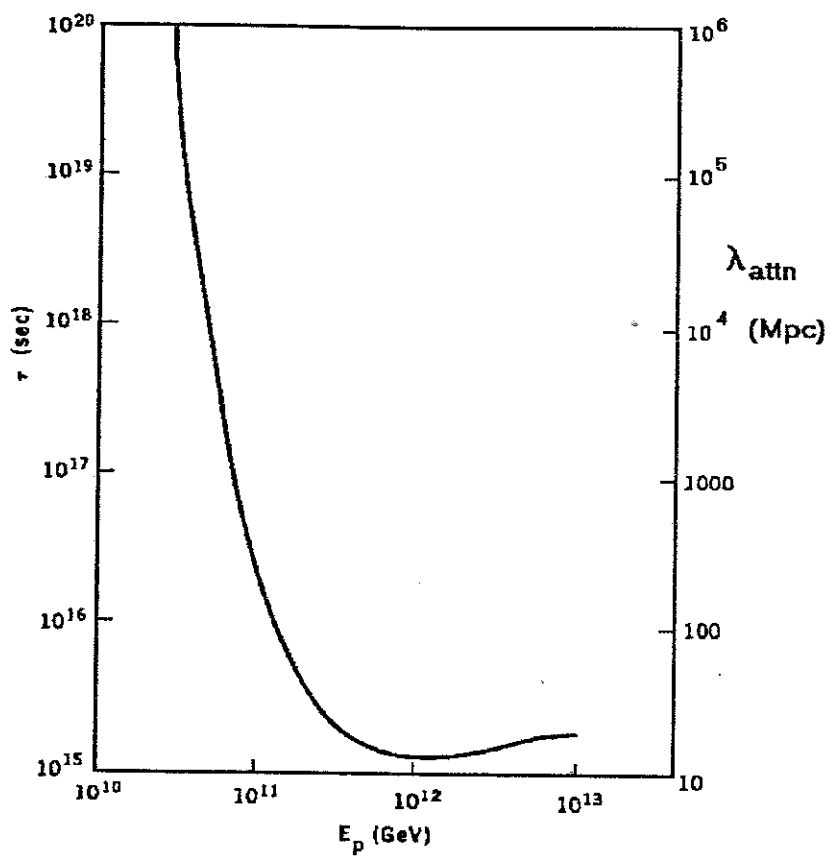
Figure 2.6—EHCR proton lifetimes and mean free paths as a function of energy.

for spectra of EHCR protons. They chose to examine spectral indices of $E^{-2.0}$, $E^{-2.5}$, and $E^{-3.0}$. For spectral indices of -2.0 and -2.5, a pile-up of cosmic rays occurs just before a cutoff—the actual cutoff energy and shape depending on the source distance and spectral index. Figure 2.7 shows an evolved $E^{-2.5}$ spectrum for different source distances.

One can extend Hill and Schramm's work further by folding in many sources. Berezinsky and Grigor'eva[44] have done similar work, and they obtain results in qualitative agreement with Hill and Schramm.

2.2.3. Composition and Propagation

A cutoff can also form if the cosmic rays are heavy nuclei.[45] Due to photo-disintegration from infrared photons in and outside the galaxy, heavier nuclei will cutoff sooner than the Greisen-Zatsepin proton cutoff, because the threshold for photodisintegration is about 5 EeV/nucleon, and near 10 EeV/nucleon, most of the photons excite the giant dipole resonance whose cross section is on the order of 0.1 barn! So, only if the heavy cosmic rays are produced copiously locally is it possible to detect them.[46]

2.2.4. EHCR Production

Different theories of UHCR acceleration have been eloquently reviewed in an article by Hillas.[47] Sokolsky has done the same recently.[48] The latest review is by Wdowczyk and Wolfendale.[49] A review of compact source acceleration mechanisms is given by Harding.[50]
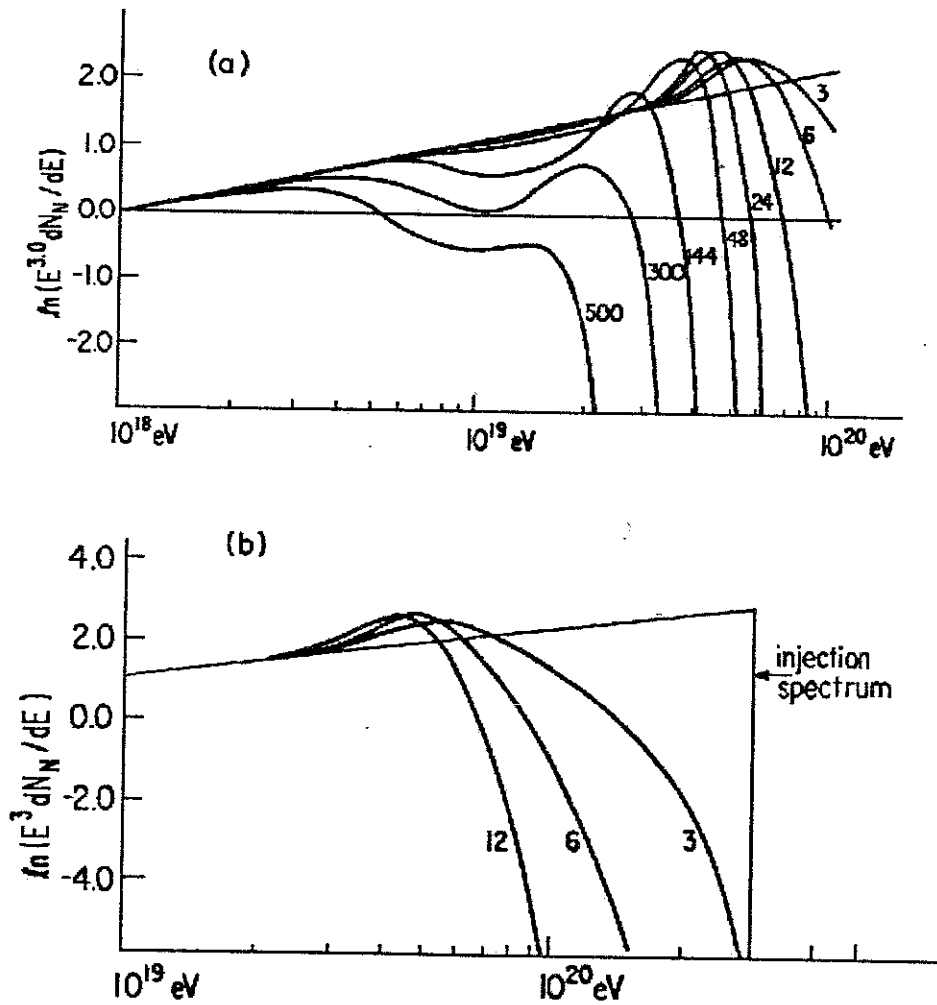
Figure 2.7—Evolved E$^{-2.5}$ proton spectra. **(a)** Source distances are labelled in attenuation lengths. **(b)** The high energy behavior of E$^{-2.5}$ protons.

CHAPTER 3

EHCR DETECTION: THE EXTENSIVE AIR SHOWER

When a cosmic ray strikes the earth's atmosphere, a cascade of particles results. This cascade is termed an Extensive Air Shower (EAS). EASs were discovered by Auger[51] and collegues in the late 1930s when they found that radiation detectors separated up to 300 meters recorded triggers coincident in time that exceeded the expected accidental rate. They are the ones that correctly inferred that these extensive showers were the result of cosmic rays interacting with particles high up in the atmosphere.

Since their discovery, EASs have been used to extend our knowledge of cosmic rays. In fact, at the highest energies, EASs are the only practical way of obtaining information of them. The extremely low flux of these particles prevents any "direct" measurements, which makes the enterprise somewhat difficult, because one has to also worry about the properties of the EAS.

Our concern is not the EAS itself, but to fully appreciate the difficulties involved in measuring the cosmic ray spectrum at the highest energies, the theory and parameterizations of the EAS and the methods of detecting it must be understood. One difficulty has already been

mentioned—that is the very low flux. However, many
outstanding questions in EHCR physics are in fact the result
of inadequately understood EAS phenomenology.

This chapter reviews how the different components of
the EAS are used to determine information about cosmic rays,
and it points out some of the reliances on EAS models that
are necessary for ground arrays especially but partly by the
Fly's Eye as well. A brief description of the ground arrays
is given as is a review of air fluorescence.

3.1 EAS: Models

When describing an EAS, it is useful to break up the
particle shower into a longitudinal distribution and a
lateral distribution. The longitudinal profile describes
the distribution of particles along the EAS trajectory
through the atmosphere. The lateral distribution refers to
the distribution of particles perpendicular to the EAS
trajectory at any point along the profile. Ground arrays
sample the lateral distribution at some point along the
trajectory, whereas the Fly's Eye measures portions of the
longitudinal profile. Ground arrays are also capable of
infering an average longitudinal profile,[52] but the Fly's
Eye can measure it on an event by event basis.

Discussions of the longitudinal development usually
involve describing electromagnetic and hadronic particle
cascades from the beginning of the shower to the end.
Models of lateral profiles detail the distribution of

electrons, muons, and Cherenkov light—all of which are used by ground array experiments to detect air showers.

3.1.1 Longitudinal Development

As previously mentioned, EASs are the results of particle cascades produced by cosmic rays impinging on the atmosphere. The exact point of initial interaction (X_0) depends on the cosmic rays's interaction length (hence, the nucleus-air inelastic cross section, $\sigma_{N\text{-air}}$) in the nitrogen (and oxygen) target. These cross sections for EeV range primaries are still not known well. This energy range corresponds to 10 TeV and higher center of mass energies. Since this energy regime is still above existing accelerator energies, no direct measurement of cross sections has been done. The closest thing to a direct measurement is the distribution of shower maxima by the Fly's Eye group[53] giving $\sigma^{inel}_{p\text{-air}} = 530 \pm 66$ mb with a nucleon-air interaction length of $\lambda_{n\text{-air}} = 45 \pm 5$ g·cm^{-2}.

Following the initial interaction, the shower particle size (N_T) grows due to subsequent interaction and decay of the particles produced in the initial interaction. Energy must be conserved, so as the shower grows, the energy per particle declines. The number of particles reaches a maximum shower size (N_{max}) at some depth (X_{max}) in the atmosphere (Figure 3.1). The shower size at maximum quoted is effectively the number of electrons (and positrons), since this overwhelmly dominates the other components.

Gaisser–Hillas Profile
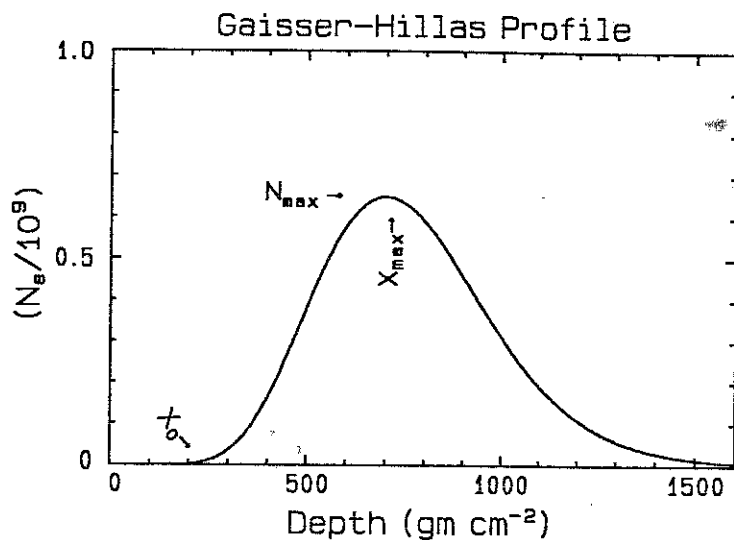
Figure 3.1—Theoretical longitudinal profile of the number of electrons in an extensive air shower resulting from a 1.0 EeV primary proton. The graph shows X_0, N_{max} and X_{max}—the three parameters that describe the profile. The line is a parameterization by Gaisser and Hillas.[54] The parameterization is based on Monte Carlo simulations, and its functional form is given in Equation 3.6.

In contrast to N_{max} and the shower tail, the depth of shower maximum, X_{max}, and the rising edge of the shower development can vary significantly. X_{max} depends on X_0, and on the inelasticity and cross sections of the first and subsequent interactions of the remnant nucleon. Exactly where the X_{max} occurs relative to the initial interaction depends heavily on parameters like the multiplicity and

inelasticity of the interacting particles which, like $\sigma^{inel}{}_{p\text{-}air}$, are also uncertain at these energies.

Fortunately, our concern is the shower energy, which can be expressed in a manner that is not too dependent on the uncertainties in cascade models. Monte Carlo and analytic calculations of cascades as well as direct measurements of the longitudinal profile[55] all show that N_{max} is proportional to the energy of the incident particle. This relationship has little dependence on the uncertain interaction parameters and is composition independent. The reason is that the longitudinal profile of the EAS is dominated by the electromagnetic interactions.

A serious experimental problem remains with this technique however. While it is true that the shower energy can be determined from N_{max}, one still has to measure N_{max}. For ground arrays, this is not so easy. Only a slice of the shower is measured at ground level and exactly where X_{max} is relative to the ground is uncertain for any given shower measured by the ground array alone.

3.1.1.1 The Hadronic Cascade

Details of the hadronic cascade have been discussed in detail elsewhere,[56] but it is useful to discuss some of the qualitative aspects to see more reasons why measuring only the lateral profile at a single depth is not as useful as sampling the longitudinal profile. Some important Monte

Carlo assumptions will also be mentioned. These assumptions may not be valid at the highest energies.

The hadronic cascade resulting from an incident nucleon or nucleus can be pictured as the producer of a series of electromagnetic cascades produced from fragments of the initial interaction. The hadronic core continuously feeds the EAS through decays to electromagnetic channels until the shower maximum point, when it has little left to give. After maximum, the shower size decreases exponentially with an attenuation length of 200 $gm \cdot cm^{-2}$.[57]

The main channels through which the hadronic development yields electromagnetic cascades is through the decay of π^0s and, less importantly, $\pi^{\pm}$s. The π^0 lifetime[58] is $8.4 \cdot 10^{-17}$ sec, so it decays almost immediately into two photons. However, when the particle energy becomes large, time dilation can extend the distance the π^0 travels. A 5 EeV π^0 can travel approximately 1 kilometer before decaying. Hence, the lifetime can be an important contribution to shower development if the π^0 has an energy $> 10^{18}$ eV. (This can occur in showers with initial energies of roughly two to three orders of magnitude higher.) So, this lifetime supression of development must be considered at the highest energies. This was first pointed out by Greisen,[59] but has also been considered recently by Dedenko and Zheleznykh.[60]

The composition of the incident cosmic ray also affects the hadronic shower development. Lighter nuclei tend to have longer interaction lengths than do heavier nuclei,

since cross sections are smaller for lighter nuclei. The lighter nuclei tend to have profiles that develop deeper in the atmosphere and that fluctuate more.

Another important composition related factor is that there are more hadronic constituents in a heavier nucleus, so when it fragments, it will fragment into proportionately more nucleons, which will in turn produce hadronic subshowers—each with a proportionately lower energy. In the simplest picture, a nucleus with A composite nucleons will break into A different nucleons each with energy E_0/A. Being of lower energy, these will reach maximum shower development sooner than one nucleon containing all the initial energy E_0. Thus, heavier nuclei will have a shallower $<X_{max}>$ than lighter nuclei of the same incident energy. The X_{max} distribution has been measured,[61] but its interpretation with regards to composition is subject to debate.

Problems are associated with measuring a slice of the air shower as ground arrays do. Fluctuations can arise from many sources. Even if the average shower is modelled correctly (which may not be the case since some physics is not known), the implicit or natural fluctuations could be enough to mis-measure the shower parameters.

3.1.1.2 The Electromagnetic Cascade

The electromagnetic shower development is often parameterized using a quantity known as the shower age[62]

$$N_e = 0.31 \cdot y^{-1/2} \cdot \exp[\ t \cdot (1 - 1.5 \cdot \ln s)\ ] \qquad (3.1)$$

where N_e is the number of electrons, t is the depth in radiation lengths, $y = \ln(E_0/\varepsilon_0)$ where ε_0 is the critical energy (the energy where losses by ionization equals losses by bremmstrahlung) and E_0 is the incident energy, and $s=3/[1+2y/t]$ is the shower age. The shower age is a measure of the development stage. If s=1, then the shower is at its maximum development, and if s<1, it is before maximum, and if s>1, it is after maximum.

For the highest known γ-ray induced shower energies, there is a correction that must be taken into account due to the Landau-Pomeranchuk-Migdal (LPM) effect.[63,64] It results in a delay in shower development because of a reduction in bremsstrahlung and pair production cross sections. This effect is not a concern for most of the observed air showers, because the effect does not turn on in air until the incident photon has an energy > 2 EeV. However, if these photons are produced in the early interactions of an incident nucleon with E > 100 EeV, then it is conceivable that the effect cannot be neglected, and it definitely cannot be neglected if the incident particle is a gamma ray.

Recently[65] has the LPM effect been incorporated into EAS parameterizations of longitudinal cascades. The results are a significant shift to deeper X_{max} positions with the elongation increasing with energy.

The LPM effect has not been observed in air showers.

3.1.1.3 The Muonic Cascade

Muons result mainly from the decay of charged pions produced from the hadronic cascade. The number of muons in an air shower is small compared to the number of electrons. They can be detected with ground arrays, however, and a good deal of work has been done on the lateral distributions of the muons in air showers. Muons were not observable by the Fly's Eye detector until the recent installment of the Michigan Muon Array (see Chapter 4). A small subset of showers are now detected by both the Fly's Eye and the array. The amount of energy going into the muonic and other nonelectronic channels is important for the Fly's Eye measurement, since this energy is not detected.

3.1.1.4 Longitudinal Profile Parameterization

For electromagnetic showers, the longitudinal profile can be parameterized in a straightforward manner and is done in Equation 3.1 above. The form for the electromagnetic profile was influenced by the theoretical investigations by Rossi.[66] The form is not convenient for air showers if for no other reason that the shower age is not a well-defined quantity for nucleon initiated showers.

There has been extensive Monte Carlo modeling of electromagnetic showers by the high-energy physics community.[67] The result from this program (EGS) is a formula for the longitudinal distribution of electromagnetic cascades in materials which is based on the gamma distribution. Linsley[68] has suggested applying the gamma

distribution to air showers. From known measured properties of air showers, he obtains a longitudinal profile based on the EGS parameterization:

$$N(X) = N_0 \cdot \xi^q \cdot \exp(-q\xi) \tag{3.2}$$

where

$$\xi = (X-X_0)/(X_{max}-X_0), \tag{3.3}$$

$$q = (X_{max}-X_0)/\lambda \tag{3.4}$$

$$N_{max} = N_0 e^{-q}. \tag{3.5}$$

From air shower data, he determines that $\lambda \simeq 58$ g·cm^{-2}.

As with photon-induced showers, there is a parameterization for proton showers that is moderately successful in fitting actual profiles. It is called the Gaisser-Hillas parameterization,[54] and has the form

$$N(X) = N_{max} \left[\frac{X - X_0}{X_{max} - X_0} \right]^{(X_{max}-X_0)/\lambda} \cdot \exp[(X_{max}-X)/\lambda] \tag{3.6}$$

where $\lambda = 70$ gm, and X is the depth at any point along the longitudinal profile. The parameterization is based on Monte Carlo simulations of proton induced air showers with E < 10 EeV. Note the similarity of this expression to that derived by Linsley. They are identical except for the value of λ.

The Fly's Eye group uses a phenomenological gaussian shaped longitudinal profile that also works reasonably well. The reason, no doubt, that it works so well is the still "poor" resolution of the Fly's Eye detectors. It is expected that the next generation detector will allow one to be a little more discriminating is this regard. With good enough imaging, information on composition and high energy cross sections can be obtained.[69]

Figure 3.2 shows a typical measurement of the electromagnetic component of an EAS by the Fly's Eye.

3.1.2 The Lateral Distributions

Lateral distribution functions describe particle densities as a functions of distance from the shower axis and number of particles in the EAS. Ground array detector groups that do EeV physics use the lateral distribution function.

Empirically, the local density of particles as a function of distance from the shower axis in a shower of total particle size N is given by[70]

$$\rho(N,r) = \frac{0.4 \cdot N}{r_M^2} \left[\frac{r_M}{r} \right]^{3/4} \left[\frac{r_M}{r + r_M} \right]^{3.25} \left(1. + \frac{r}{11.4 \cdot r_M} \right)$$

$$(3.7)$$

where r_M is the Moliere scattering unit. Neglecting the last factor, this agrees quite well with the electromagnetic

Evt # 2586.   Date: 3/1/87

$R_p = 3.01 \pm .22$ km $\theta_z = 37.9 \pm 1.6$ deg

$E = 0.59 \pm 0.03$ EeV
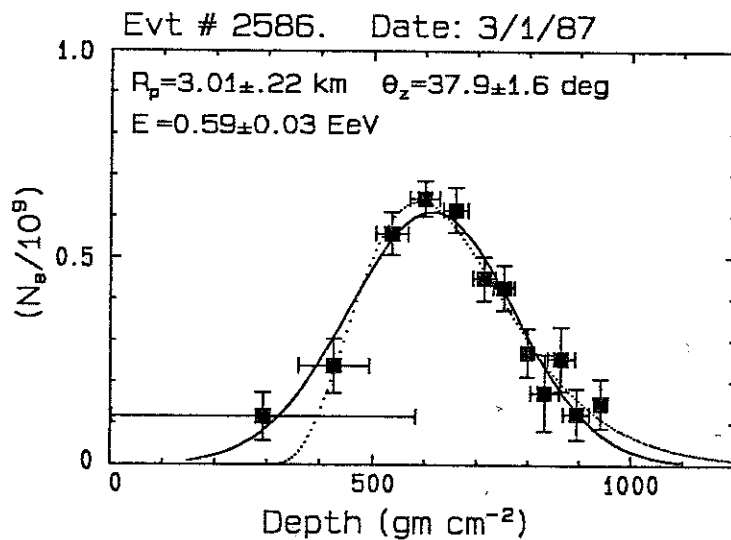
Figure 3.2—A typical electromagnetic longitudinal profile from the Fly's Eye experiment. The solid line is the least-squares gaussian fit while the dotted line is the least-squares Gaisser-Hillas fit. R_p and θ_z are described in Chapter 5. The estimated energy is the energy of the incident cosmic ray and not just the electromagnetic component.

cascade formula derived by Nishimura and Kamata[71] if the "average" shower has a shower age of s = 1.25. A remarkable fact of Equation 3.7 is that it is in excellent agreement with average shower data for shower sizes ranging from $2 \cdot 10^3$ to $2 \cdot 10^9$ electrons at atmospheric depths ranging from 537 $gm \cdot cm^{-2}$ to 1800 $gm \cdot cm^{-2}$, and at distances from the shower axis ranging from very close to the shower core (< 1m) to over 1.5 km! However, the formula is for an average shower. On a shower by shower basis, the fluctuation in density can be quite large.[72]

3.1.3.1 The Electron Lateral Distribution

From cascade theory, Nishimura and Kamata derived the lateral distribution function for an electromagnetic shower. They obtained the relation:

$$f(s, r/r_M) = \frac{\Gamma(4.5-s)}{2\pi \, \Gamma(s)\Gamma(4.5-2s)} \left(\frac{r}{r_M} \right)^{s-2} \left(1 + \frac{r}{r_M} \right)^{s-4.5}$$

(3.8)

for showers with age in the range 0.5 < s < 1.5. With s=1.25, this equation becomes quite similar to the one obtained empirically. The only major difference is the term at the end of the empirical equation to describe lateral distributions at large distances from the shower core.

3.1.3.2 The Muon Lateral Distribution

Experimentally,[73] for EAS, the muon lateral distribution is given by the relation

$$\rho(N_\mu, r) = 18 \, (N/10^6) \, r^{-3/4} \, [1 + (r/320)]^{-2.5}$$

(3.9)

Far from the core, the particles in the shower are mostly muons. Muons are almost exclusively from charged pion decay which in turn are products of nuclear interactions. In principle, the number of muons is composition dependent.

3.1.3.3. The Cherenkov Lateral Distribution

The Cherenkov light from air showers was first detected by Galbraith and Jelley in 1952.[74] Since the original measurements, many experiments have taken advantage of Cherenkov light to aid in understanding extensive air showers. The important experiment for this discussion is the group at Yakutsk who use Cherenkov light as an important energy calibration.

The distribution of Cherenkov light has an added importance, for the amount of light reaching the ground is an integral over the previous history of the shower and is not just proportional to the local particle density.

3.2. EHCR Ground Array Detectors

The study of cosmic rays via the ground array detection of EAS was pioneered by Rossi in the late 1940s.[75] Linsley extended the technique by creating an array which covered an area of almost 10 square kilometers.[76] He was the first to detect events with energies above 10 EeV.

There have been and are now many ground arrays in the world which utilize the lateral distribution, but most of them are designed for PeV cosmic ray air showers. Only those dedicated to studies of the upper end of the spectrum

are detailed below. Table 3.1 summarizes the arrays—both past and present—dedicated to studies of primaries with energy above 0.1 EeV and their method of detection.

Ground arrays are typically an array of scintillation counters spread out on the surface of the Earth over an area of 10-100 km^2. The detector area and spacing determine the EAS size threshold and resolution.

3.2.1. Ground Array Energy Estimation

Historically, two methods have been used to estimate the primary energy from the lateral distribution. The first method fits a lateral distribution function to obtain the total number of electrons in the shower and then converts this $N(X_{ground})$ to N_{max} from an average elongation formula. From N_{max}, the energy is then determined by a linear factor from the experimenter's favorite model. The pitfalls of this method are (1) average formulae are used, and (2) the lateral distribution is not always known well for EeV showers due to the wide spacing of array counters, and the part near the shower core is not well sampled. However, the particle distribution near the core must be well measured for a good profile to be fit.

The second method derived originally by Hillas[77] and associates uses the density of particles at a "compromise" distance from the shower core—typically 600 meters. The energy is determined by Monte Carlo studies that typically involved different composition and interaction models.

Table 3.1—Ground arrays for EeV physics. The Michigan
array is used only in conjunction with the Fly's Eye.

Array (Running period)	Location	Area (km^2)	Types of Detector
Volcano Ranch (1960–1972)	USA	8	Scintillation Counters
Haverah Park (1967–1987)	England	10	Water Cherenkov
SUGAR (1968–1979)	Australia	200	Muon Counters
Yakutsk (1974–)	USSR	20	Scintillation Counters; Atmos. Cherenkov; Muon Counters
Akeno (1984–)	Japan	20–100	Scintillation Counters; Muon Counters
Michigan (1988–)	Dugway	2–5	Muon Counters in coincidence with FE

These studies indicate that the particle density at 600 meters from the core at ground level is sensitive mainly to initial particle energy and is insensitive to the position of X_0 and composition.

3.2.2. Past and Existing Ground Arrays

3.2.2.1. Volcano Ranch

The Volcano Ranch experiment[78] was the ground breaker in the EeV field. It was the first to detect EAS whose parent cosmic ray with E>10 EeV and also to claim to see events exceeding 100 EeV. The air fluorescence technique was shown feasible with the aid of the Volcano Ranch array.

3.2.2.2. Haverah Park

The Haverah Park array[79] was operated principally by the group from the University of Leeds led by A. Watson. It operated from 1962 until 1987 when it was turned off.

The principle detection mechanism was energy deposition in water tanks. The Cherenkov light generated was proportional to the amount of energy the EAS lost while passing through the detector.

As previously described, the primary energy was estimated by the relationship between the particle density at 600 meters, $\rho(600)$, and the primary energy.

3.2.2.3. SUGAR Array

The SUGAR array[80] was operated by the U. of Sydney. The detector consisted of muon counters with an effective

area of 100 km^2. Similarly to the other ground arrays, the SUGAR array used Monte Carlos to estimate the energy of primaries.

This detector unfortunately had problems with phototube afterpulsing which has made interpretation difficult.

3.2.2.4. Yakutsk

As ground arrays in the EeV region go, the Yakutsk array[81] is probably the most thorough. The Yakutsk array consists of surface electron counters, muon detectors, and, during clear moonless nights, Cherenkov light detectors. The array has an effective area of 20 km^2 which is slightly larger than the Haverah Park array.

Another important advantage is the Cherenkov light, which allows an important calibration of their S(600) quantity (the shower size density at 600 meters). The Yakutsk array does not need to rely on the Monte Carlo calculations to determine the normalization factor for their S(600) parameter.

3.2.2.5. Akeno

The Akeno array[82] now consists of a 1 km^2 closly packed array (for lower energy studies) and an less-densly spaced 20 km^2 array. It consists of electron and muon counters. Their energy estimation is based on the electron density 600 meters from the core, S(600). Their conversion factor is based on standard QCD based Monte Carlo simulations[83] of different energies (10^{17}, 10^{18}, 10^{19} eV), composition (P, CNO,

Fe) and zenith angles (secθ=1.0,1.1,1.2,1.3,1.4,1.5). They
obtained the relation between primary energy and S(600) to
be

$$E_0(eV) = (2.3\pm0.10)\cdot10^{17} \, S(600)^{1.02\pm.02} \qquad (3.10)$$

at the Akeno depth. When they convert their formula to sea
level to compare with Yakutsk and Haverah Park, they get a
formula that is not inconsistent with the other two groups.

The Akeno array was recently expanded to 100 km^2.

3.2.2.6 Michigan-Utah

This detector is designed to resolve uncertainties in
PeV energy gamma-ray astronomy and is not optimized for EeV
physics. With the Fly's Eye nearby, the array has an
effective aperture much larger than its outer boundaries,
The Fly's Eye thus provides the important shower parameters
needed for adequate reconstruction. The array will be
useful in verifying the estimation of the undetected energy
of the Fly's Eye measurement. It has already shown the
energy calibration is close to Yakutsk.[84]

3.3. Light Production in EAS

There are difficulties with using light from EAS: (1)
there is an enourmous background problem, and (2) the
detector duty cycle is quite low (< 10%). The great
advantages in using light are calorimetry and aperture. The
dependence on model assumptions is not as crucial for

determining shower parameters as it is for ground arrays, and there is a larger collecting area in the atmosphere.

Excellent treatises have been written discussing the optimization of signal to noise for light detection methods. Signal to noise considerations for Cherenkov detectors are described well by Jelley.[85] For atmospheric fluorescence, a good discussion is available in [1].

The Fly's Eye detects both angularly distributed Cherenkov light and isotropically emitted atmospheric fluorescence light, but due to current FE detector resolution and model uncertainties, the Cherenkov component cannot be used too reliably. Fortunately, this component not a significant one for showers > 1.5 km away from the Fly's Eye or for parts of the shower viewed at large emission angles. The Fly's Eye dominant signal is nitrogen fluorescence, so this technique is explored in full detail. To insure Cherenkov light is not a problem, a discussion of it is included as well.

3.3.1 Atmospheric Fluorescence

The air fluorescence technique was proposed independently in the early 1960s by Greisen,[86,87] Suga,[88] and Chudakov.[89] The first attempt to detect EAS by air fluorescence was tried by Greisen[90] and his group at Cornell in 1965. The noble attempt was unsuccessful.

The first successful detection was made by the Utah group[91] in conjunction with the Volcano Ranch ground array.

Since late 1981, the Fly's Eye has been in operation at Dugway, Utah.

The fluorescence technique is based on the ionization of the N_2 molecules in the atmosphere. Almost all of the optical fluorescence is from the 2P band of molecular nitrogen and the 1N band of the N_2^+ ion.[92-94] The measured optical fluorescence spectrum is shown in Figure 3.3. The fluorescent yield has slight altitude and temperature dependences (Figure 3.4), though, remarkably, there is not a strong altitude dependence. The near constancy of net light output is a result of two effects that tend to cancel. The yield increases with decreasing height, because the number of excitations per unit path length is proportional to the atmospheric pressure. However, the fluoresence efficiency is also inversely proportional to the pressure, because there are more de-excitations from collisions, and the number of collisions increases with increasing pressure.

The number of fluorescence photons produced by an electron in an EAS is given by

$$N_\gamma(\rho, h) = (\varepsilon_0/X_0) \cdot \rho(h) \cdot E(p) \tag{3.11}$$

where N_γ is measured in MeV/electron/meter, ε_0/X_0 is the ratio of the electron critical energy (in MeV) to its radiation length in air (grams/cm^2), $\rho(h)$ is the atmospheric density in grams/cm^3 as a function of height h above sea
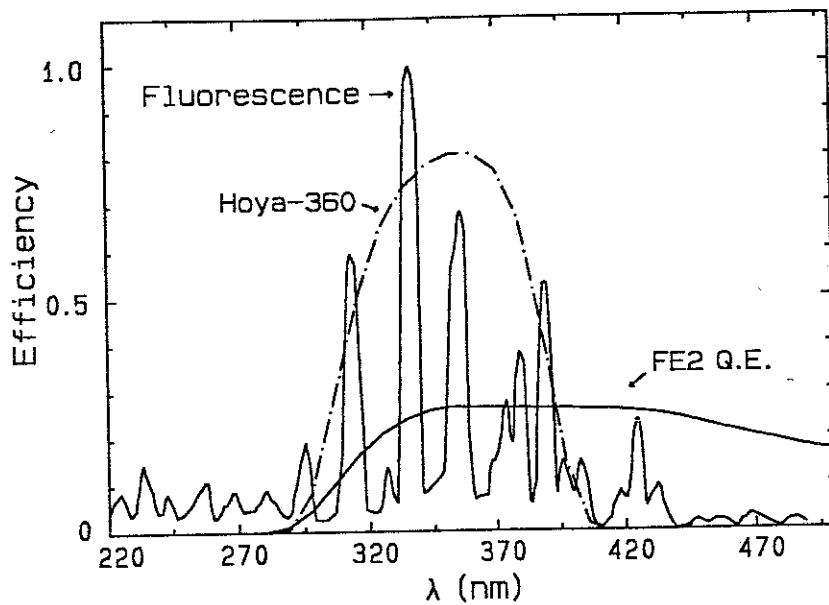
Figure 3.3—The atmospheric fluorescence efficiency curve along with the UV-pass filter used by the Fly's Eye as well as the FE2 tube quantum efficiency.
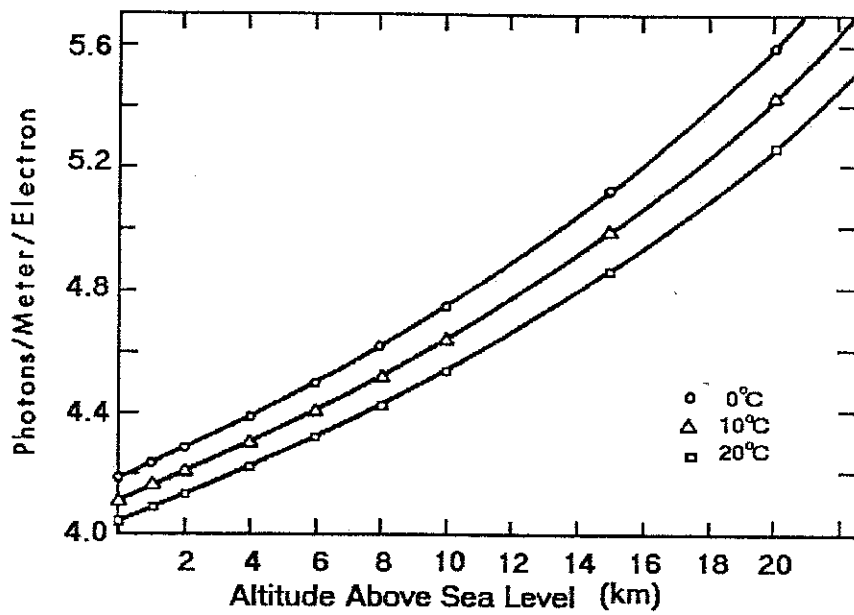
Figure 3.4—The fluorescence efficiency as a function of altitude and temperature (reference [1]).

level, and E(p) is the fluorescence efficiency, which is a function of pressure.

ε_0, X_0 have been determined[95] to be 81 MeV and 31.7 gm$\cdot$cm^{-2} respectively yielding a ratio of 2.18 MeV$\cdot$cm^2/gm. Others have determined consistent values for ε_0, X_0[62,96] but this ratio still contributes to a possible systematic error in the Fly's Eye result.

The pressure, temperature, and atmospheric density $\rho(h)$ variation with height, calculated from the ideal gas law and the isothermal atmosphere approximation, are respectively

$$p(h) = p_0 \left[1 - \frac{a \cdot h}{T_0} \right]^{[(gM/aR)]} \tag{3.12}$$

$$T(h) = T - a \cdot h \tag{3.13}$$

$$\rho(h) = \frac{M \cdot p_0}{R \cdot T_0} \left[1 - \frac{a \cdot h}{T_0} \right]^{[(gM/aR)-1]} \tag{3.14}$$

where a $\simeq$ 6°K/km and is the isothermal decrease in temperature with height, g is the gravitational acceleration (9.8 m$\cdot$sec^{-2}), M is the molecular weight of air (29), R is the gas constant (8.32 j/(mole°K)). p_0 and T_0 are the reference pressure and temperature whose values are chosen to be sea level pressure and 300°K respectively.

The fluorescence efficiency has been thoroughly analyzed by Bunner.[97] The efficiency for photon production is given by

$$E(p) = \sum_{i=1}^{N_{bands}} \frac{E(\lambda_i)}{1 + p/p_i'} \tag{3.15}$$

where $E(\lambda_i)$ is the efficiency for the excitation nitrogen band at λ_i in the absence of quenching, and p_i' is a constant which depends on the excitation band. p_i' has a dependence on temperature whose value increases with the square root power.

Putting in the temperature and pressure dependences gives

$$\rho(h) \cdot E_i(h) = \frac{E(\lambda_i) \quad \dfrac{M \cdot p_0}{R \cdot T_0} \quad \left[1 - \dfrac{a \cdot h}{T_0} \right]^{[(gM/aR)-1]}}{1 + \dfrac{p_0}{p_i'(T_0)} \left[1 - \dfrac{a \cdot h}{T_0} \right]^{[(gM/aR)+1/2]}} \cdot \tag{3.16}$$

If the approximation $p(h) \gg p_i'(T_0)$ is made (which is valid for $h \leq 10$ km), the expression simplifies considerably. The fluorescent yield becomes

$$N_\gamma(T_0,h) = \frac{\varepsilon_0 \cdot M}{X_0 \cdot R \cdot T_0 \cdot (1 - a \cdot h/T_0)^{1/2}} \sum_i^{Nband} \{ p_i'(T_0) \cdot E(\lambda_i) \} \tag{3.17}$$

in units of MeV/cm/particle which, converted to
photons/cm/particle, gives

$$N_\gamma(T_0,h) = \frac{\varepsilon_0 \cdot M}{X_0 \cdot R \cdot T_0 \cdot (1 - a \cdot h/T_0)^{1/2}} \sum_i^{Nband} \{\lambda_i \cdot p_i'(T_0) \cdot E(\lambda_i)/.124\}$$

(3.18)

where λ_i is in nm. The values of λ_i, $E(\lambda_i)$, and p_i' were
compiled by Bunner, and they are listed in Table 3.2.

The amount of light generated by each electron in the
EAS is small. However, 0.1 EeV primaries produce showers
with more than 10^8 electrons near the maximum; enough light
is produced even with only 0.6% fluorescence efficiency.

So far, the assumptions about temperature have been
that it decreases linearly with height, and that its value
at sea level is 300 °K. For natural temperature variations,
the yield changes slightly due to pressure changes, and p_i'
has a temperature dependence whose value increases as the
square root of the temperature.[98] So,

$$N_\gamma(T,h) \propto (T)^{1/2}/[\ T \cdot (1-a \cdot h/T)^{1/2}\ ]\ .$$

(3.19)

Thus,

$$N_\gamma(T,h) = N_\gamma(T_0,0) \cdot [\ T_0/(T-a \cdot h)\ ]^{1/2}$$

(3.20)

gives the temperature and altitude dependence of the
fluorescence yield where h and T are the height from sea

Table 3.2. Atmospheric fluorescence efficiencies compiled by Bunner[99] and used by Fly's Eye.

Band		λ (nm)	$E(\lambda_i)$ %	p_i' (mm Hg)	$E_i(p_0, T_0)$ $(\cdot 10^{-4})$
1N	0-0	391.4	.33	1.0	4.33
	0-1	427.8	.11		1.44
	0-2	470.9	.020		.26
	0-3	522.8	.003		.039
2P	0-0	337.1	.0820	15	15.9
	0-1	355.7	.0615		11.9
	0-2	380.5	.0213		4.12
	0-3	405.9	.0067		1.30
	0-4	434.4	.0019		.37
	0-5	466.7	.0004		.077
	1-0	315.9	.050	6.5	4.3
	1-1	333.9	.0041		.35
	1-2	353.7	.0290		2.48
	1-3	375.6	.0271		2.31
	1-4	399.8	.0160		1.36
	1-5	427.0	.0035		.30
	1-6	457.4	.0016		.14
	1-7	491.7	.0004		.034
	2-0	297.7	.016	4.6	.96
	2-1	313.6	.029		1.74
	2-2	330.9	.0020		.12
	2-3	350.0	.0040		.24
	2-4	371.1	.0100		.60
	2-5	394.3	.0064		.38
	2-6	420.1	.0046		.28
	2-7	449.0	.0015		.09
	2-8	481.5	.0008		.05
	3-0	282.0	.011	2.5	.36
	3-1	296.2	.014		.46
	3-2	311.7	.005		.16
	3-3	328.5	.0154		.50
	3-4	346.9	.0063		.21
	3-5	367.2	.0046		.15
	3-6	389.4	.003		.10
	3-7	414.1	.0017		.056
	3-8	441.6	.0007		.023

level and the sea level temperature. This is the formula used for the Fly's Eye data.

3.3.2 Atmospheric Cherenkov Production

Thorough discussions of the Cherenkov light production in EAS can be found in the literature.[1,62] How Cherenkov light is handled for Fly's Eye data is detailed in Chapter 5. Here, only a brief introduction is given to Cherenkov light in the atmosphere. The discussion is similar to that in [1].

Cherenkov light is produced principally by electrons in the shower. The light is highly collimated along the EAS axis, and the amount at any time depends on past number of electrons in the shower as well as the current number. Here we consider the number produced by a distribution of relativistic electrons like those in air showers.

A single electron produces N_c Cherenkov photon in unit length dl according to

$$\frac{dN_c}{dl} = 2\pi\alpha \int \left(1 - 1/(\beta n)^2 \right) d(1/\lambda) \tag{3.21}$$

where λ is the wavelength of the Cherenkov photon, n is the index of refraction, $\beta^2 = v^2/c^2 = 1 - 1/\gamma^2$ where $\gamma = mc^2/E_e^2$, and α is the fine structure constant. The rate of photons produced for a distribution of electrons in a shower will be

$$\frac{dN_c}{dl} = 2\pi\alpha N_e \int d(1/\lambda) \int_E^\infty f(E')\left(1 - 1/(\beta n)^2 \right) dE'$$

$$\tag{3.22}$$

if the electrons have an energy distribution of form

$$F(E) = \int_E^\infty f(E') \, dE' \quad .$$

(3.23)

Hillas[62] has studied the distribution of electrons as a function of energy in air showers. Near shower maximum, the electrons have a distribution given by

$$F(E) = \frac{34.8}{(40.4 + E)(1 + 10^{-4}E)^2}$$

(3.24)

where $F(E)$ is the fraction above energy E (Mev). Using an isothermal atmosphere and realizing that the index of refraction (n) is near unity,

$$\delta(h) = (n-1) \cdot \exp(-h/H_0) = \delta_0 \cdot \exp(-h/H_0)$$

(3.25)

where H_0 is the atmospheric scale height ($\simeq 7.3$ km), $\delta_0 = 2.4 \cdot 10^{-4}$, the value at the FE1 altitude. Then, Equation (3.22) can be written as

$$\frac{dN_c}{dl} = 2\pi\alpha N_e \int d(1/\lambda) \int_{E_t}^\infty f(E') \left(2\delta - m^2c^4/E^2 \right) dE'$$

(3.26)

where

$$\int_{E_t}^\infty f(E') \left(2\delta - m^2c^4/E^2 \right) dE' = 2\delta \cdot F(1.57 \cdot E_t)$$

(3.27)

giving the equation

$$\frac{dN_c}{dl} = 2\pi\alpha N_e \int 2\delta \cdot F(1.57 \cdot E_t) \ d(1/\lambda) \qquad (3.28)$$

The integral range begins at the threshold energy for Cherenkov production which is $E_t = m \cdot c^2/(2\delta)^{1/2}$.

More importantly for the Fly's Eye is the angular distribution of Cherenkov light. The angular distribution is discussed in Chapter 5.

CHAPTER 4

THE FLY'S EYE DETECTORS

4.1. Introduction

The Fly's Eye detectors have been described in detail elsewhere.[1,100,101] This chapter is designed to augment the published descriptions by explaining many operational aspects and detector parameters in further detail. Details related to the energy calibration are emphasized.

Fly's Eye 1 (FE1) consists of 880 photomultiplier tubes and Winston light collectors distributed among 67 62-inch spherical section front aluminized mirrors in groups of 12 and 14 (Figures 4.1, 4.2). Fly's Eye 2 (FE2) is similar to FE1 except it has 36 mirrors and thus a smaller aperture.

During operation each mirror system is turned towards a section of the night sky, so the entire night sky is viewed by FE1, and a significant fraction is covered by FE2. Figure 4.3 gives an idea of tube apertures and their coverage of the night sky.

Observations must be restricted to clear moonless nights yielding a low duty cycle of only 8.5 %. Later duty cycles have been higher. The low duty cycle is compensated somewhat by the relatively large detector aperture.
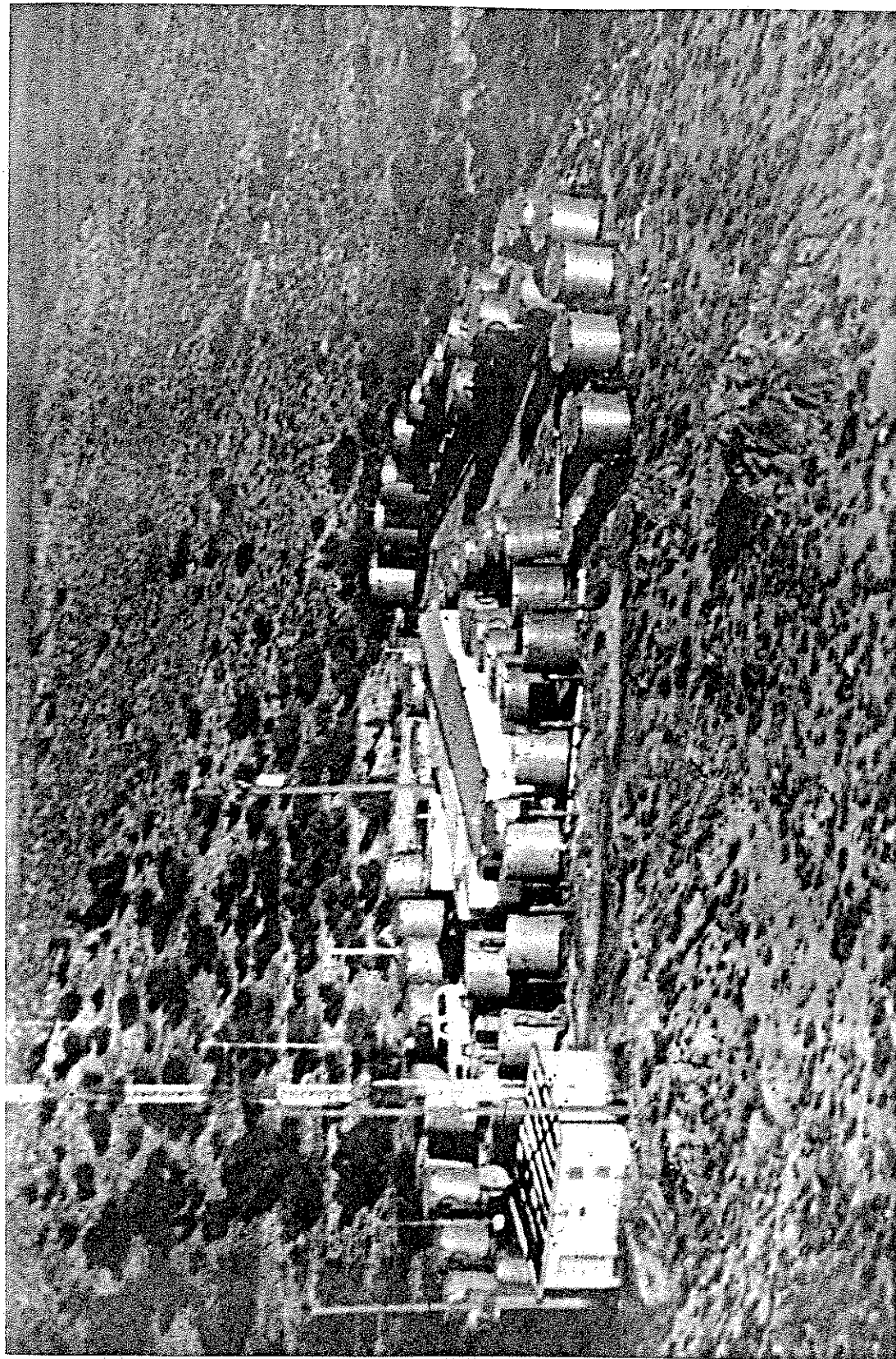
Figure 4.1—A view of FE1 and the pristine Dugway environment.
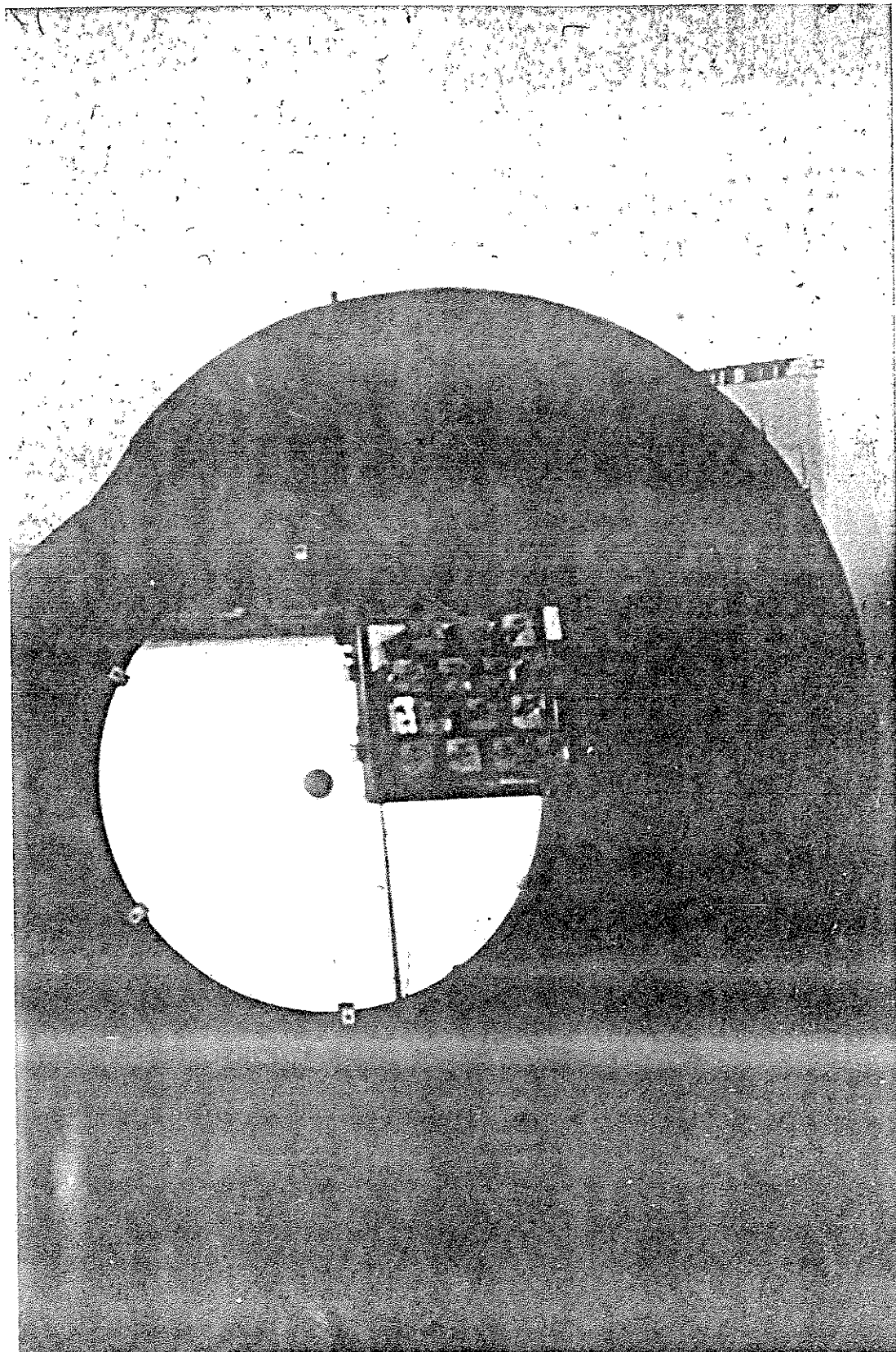
Figure 4.2. A Fly's Eye 'can' with a view of the phototube cluster and mirror.
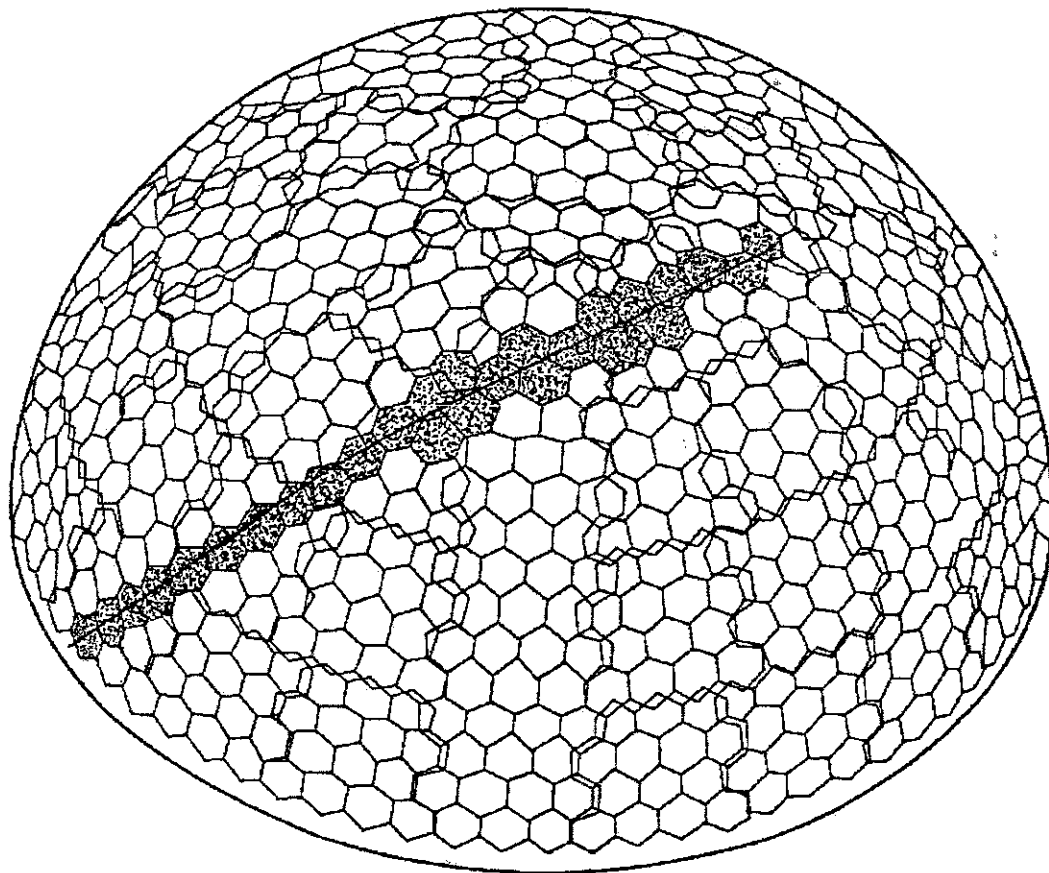
Figure 4.3—A side-view of the Fly's Eye tube apertures.

The detectors are located at Dugway, Utah, and are separated by 3.4 km. FE1 stands atop a small hill (called Little Granite Mountain) while FE2 is in the valley floor approximately Northeast in direction from FE1. Table 4.1 lists some important physical parameters of the detectors.

4.2 Fly's Eye Electronics

The Fly's Eye electronics layout is described pictorially by Figures 4.4 and 4.5. Both eyes have the same general layout, with only slight differences between the two detectors. The electronics for each eye are controlled with a PDP 11/34 computer containing 128 Kwords of memory and a peripheral 30 Mbyte Winchester disk. The operating system used is DEC's RSX-11M V4.0. DEC's DR11 parallel interface is used for unibus connection to many 16 bit I/O external data busses. Data acquisition occurs when the Master coincidence triggering requirements are met. The software written for data acquisition and diagnostics has been detailed elsewhere.[102]

The data acquisition of an event following a master coincidence consists of reading in (1) digitized integrals of triggering channels, (2) trigger thresholds of triggering channels, (3) firing times of triggering channels, and (4) the time of triggering from a WWVB clock with ± 1 ms resolution. Trigger rates are typically < 1 sec^{-1}. The time to process an event is typically 1-10 msec, so the dead time is usually < 1%.

Table 4.1 Important Fly's Eye Detector parameters.

Parameters	FE1	FE2
Latitude	40°11′47.78″	40°13′18.00″
Longitude	112°50′9.25″	112°48′59.07″
Height above Sea Level (m)	1593.	1459.
Atmospheric Depth (g)	852	867
Number of mirrors	67	36
Number of PMTs	880	464
PMT	EMI-9861B	EMI-9793B
PMT peak q.e.	0.17	0.26

Similar features	Value
Mirror diameter	1.575 m
Focal Length	1.52 m
Mirror obscuration	13 %
PMT-Winston cone aperture	6.57 msr
Standard Mirror eff.(< 7,87)	0.70
(> 7,87)	0.90
Standard Winston cone eff.	0.80
UV-pass filter	Hoya U-360
Peak filter transmission (350 nm)	.81

FE1 to FE2 vector: (1.668,2.942,−0.134) (km)
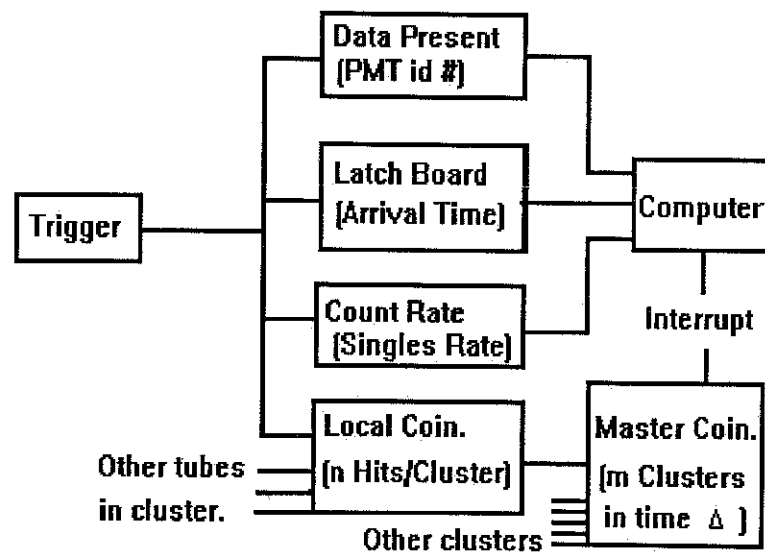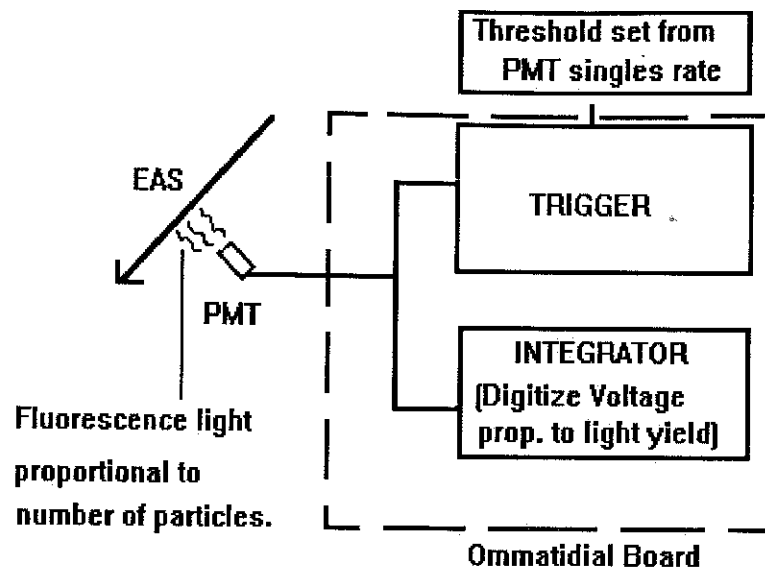
Figure 4.4—Global Fly's Eye electronics layout.
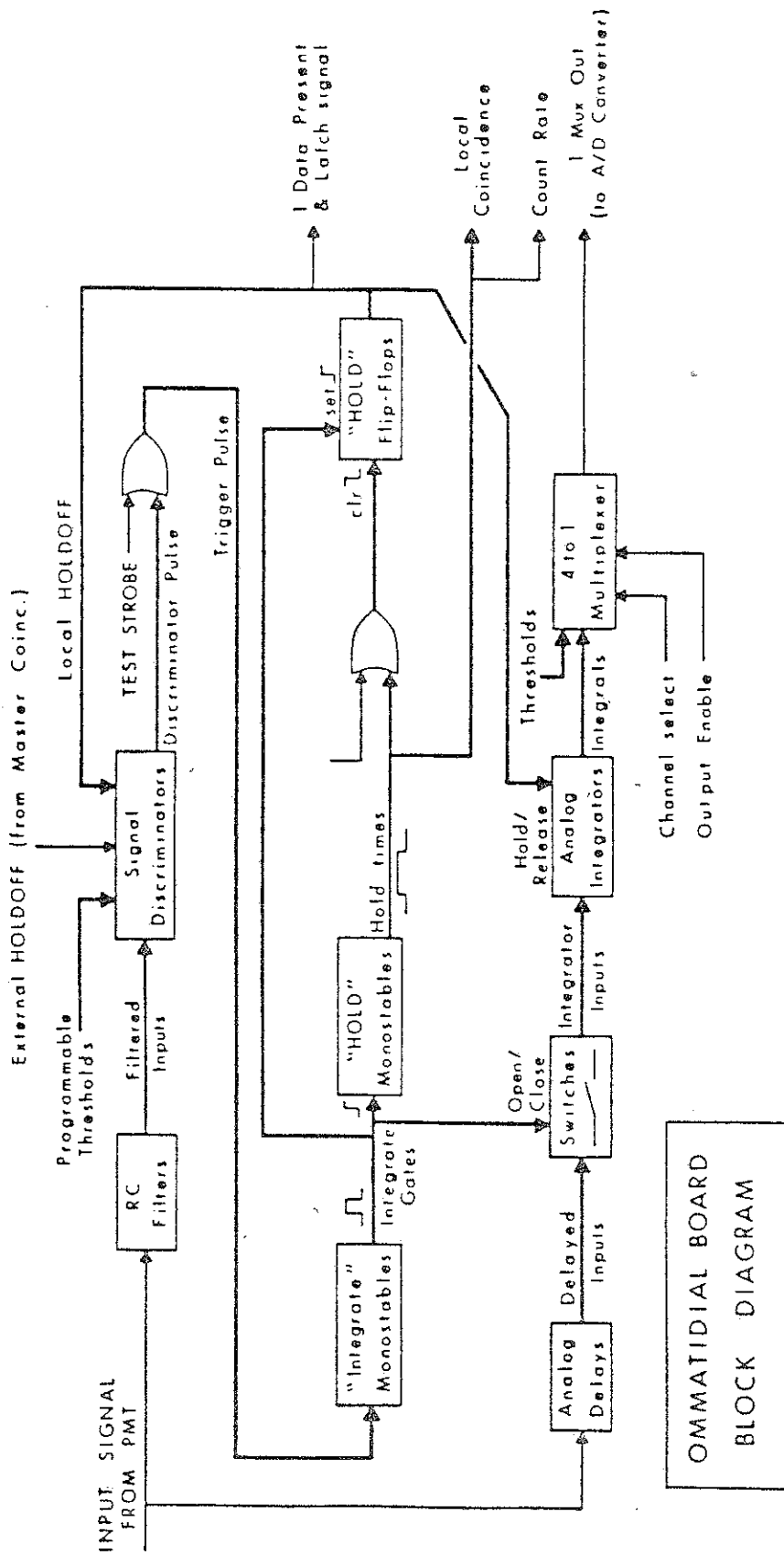
Figure 4.5—Ommatidial board layout.

4.2.1 Event Triggering

Event triggering is divided into three levels: (1) single, (2) local, and (3) master triggers. All levels have three different triggering channels (channels 2-4) that act independently of each other and are optimized for different pulse widths and thus different shower distances. This allows for a large dynamic range of pulse widths corresponding to a large range of impact parameters. All three triggers exist in hardware.

There is a fourth triggering channel (channel 1) that is used for Cherenkov 'blast' triggers from PeV EAS, but it plays no part in EeV shower detection.

4.2.1.1 Single Triggering

Each PMT's signal is split into the three different channels and sent through low-pass filters. For FE2 and for most of the time for FE1, the filters have been RC filters. π-section filters replaced the RC filters at FE1 in late 1987. The singles triggering section is physically located on the ommaditial board (OMB).

The filtered pulse from each channel is routed to a discriminator with a threshold voltage set to a value determined by the count rate section of the electronics (typically 100-300 mV). The thresholds are adjusted to give a constant singles triggering count rate (typically 40 Hz, but this number has varied during the course of FE operation).

When a filtered pulse exceeds the threshold, a signal is sent to the integrate section of the OMB closing an electronic switch through which the delayed signal passes and is integrated. The integral is held for a period of time that depends on the channel. Simultaneously, a pulse is sent to the local coincidence board. If the OMB does not receive a return signal from the local coincidence board signifying that another tube in the mirror has triggered, the electronics is reset, and the OMB is again ready for another trigger. The coincidence gate times for the triggering channels are listed in Table 4.2.

4.2.1.2 Local Triggering

Local coincidences are generated at the mirror level. If two or more PMTs in a given mirror have filtered signals exceeding their individual threshold within the local coincidence gate time, then a local coincidence pulse is sent to the Master coincidence and to the triggered OMBs. Upon receiving a signal from the local triggers, the OMBs will to continue to hold the integrated signal and firing time until the local coincidence line is cleared or the hold is extended by the master trigger.

4.2.1.3 Master Triggering

Master coincidences are generated when any two local coincidences from two different mirrors in the system are generated within the Master coincidence gate time. Again, each channel is on a seperate trigger line. Once a master

Table 4.2. 'Hold' times for the three coincidence levels and three channels. Channel 1 is used only for 'blast' operation and is not part of the 'track' mode triggering.

| | Trigger Channel | | | |
	1	2	3	4
Single gate(μsec)	–	4.	10.	25.
Local gate(μsec)	.2	8.	20.	50.
Master gate(μsec)	.2	8.	20.	50.

coincidence is generated for any of the three channels, the computer is interrupted and data acquisition occurs.

4.3. Fly's Eye Parameters

4.3.1. Introduction

There are three fundamental parameters necessary from each channel (phototube-OMB system) for accurate EAS reconstruction. These are (1) the tube center pointing directions, (2) the EAS light arrival time, and (3) the amount of light in the tube apertures. From these and some relatively minor model assumptions of items like mirror optics, etc., the geometry and profile of the EAS are reconstructed.

Event reconstruction is specifically addressed in Chapter 5. Here the reliability of the measured fundamental parameters is explored. This is determined by (1) the mirror pointing directions, (2) the relative channel firing time accuracy, and (3) the energy calibration. The uncertainty in these ultimately determines how well air

showers can be reconstructed. These are the parameters that must be continually checked.

4.3.2. Mirror Alignment

4.3.2.1. Nominal and Residual Directions

Due to the difficulty in aligning mirror directions exactly where one would like them, each mirror is set to within ± 2° of its "nominal" or the desired direction for each mirror for full sky coverage. The residual difference between the nominal direction and the actual direction is then measured. The FE mirror's pointing directions are determined by two independent surveying methods: (1) the transit survey, and (2) the photographic survey. Both methods measure the mirror center pointing direction.

4.3.2.2. Transit Survey

The transit survey finds the mirror directions by sighting the image of the tube cluster center with a standard survey transit and then measuring the angles (zenith and azimuth) between the cluster center image and distant landmarks visible from an elevated platform upon which the transit sits. The cluster center image gives the direction where the mirror center is pointing, so the mirror center vector is found by the angles to the two known landmark vectors.

For an internal consistency check, two different points on the mirror are sampled twice, and each point is measured relative to two landmarks. The check is made by calculating

the angle between the two landmarks from the sum of the angles of the landmark and the cluster center. This is compared to the actual angular difference of the landmarks.

The limiting factors in the transit survey are the mirror spot size and the number of measurements. To reduce coma effects, the transit is aligned as close to the cluster edge as possible. The estimated errors in the transit survey is $< 1/3°$.[103] This is based on the consistency between measurements of the actual landmark angular difference and that estimated from the survey.

4.3.2.3. Photographic Survey

The photographic survey finds the mirror directions by taking pictures of the night sky viewed by the mirrors. This is done by placing a large camera containing four sheets of 8×10 inch TRI-X black and white film on the cluster plane. The mirror is turned up as it is during the normal data run, and the camera shutter is opened, so the film is exposed to the night sky. If the time is properly recorded, the mirror direction is then found by comparing the star images on the film (hence the cluster plane) with star positions calculated from their well known Right Ascensions and Declinations.

To estimate the star positions from the film, a chi-square fit of sorts is done. Because the star images on the photographs can be fairly large (but < 2.5 cm), the exact position of the star on the cluster plane is sometimes

difficult to determine. The human film scanner determines the approximate center of the star image and estimates an approximate spot size for each image. A Monte Carlo 'fit' is done by varying the exact image position to within the estimated spot size. At each variation, the mirror directions are varied until the chi-square is minimized. Except when the iteration fails, the best direction fit is the average mirror direction for all chi-square minima.

Typical statistical errors for the photo survey are 1/3°. The systematic error is estimated by multiple exposures of a single mirror and is also about 1/3°.

As with the transit survey, the photo survey is limited by spot size, but there are possible sources of systematic error. For example, the time may be recorded incorrectly, and the distance from the cluster center to the camera center may be mismeasured. The possibility of these happening is small. The optimal solution for better pointing accuracy is to get better mirrors, but a more accurate star image position estimation is not out of the question. A densitometer reading of the exposed film would help isolate the image center better, but it is doubtful that a large improvement would be made.

Figure 4.6(a),(b) show the differences in the calculated residuals from the average value of the transit and photographic method, while 4.6(c) histograms the angular difference in the two mirror center vectors. The average mirror directions are good to approximately 0.25°. Because

Photo vs. Transit
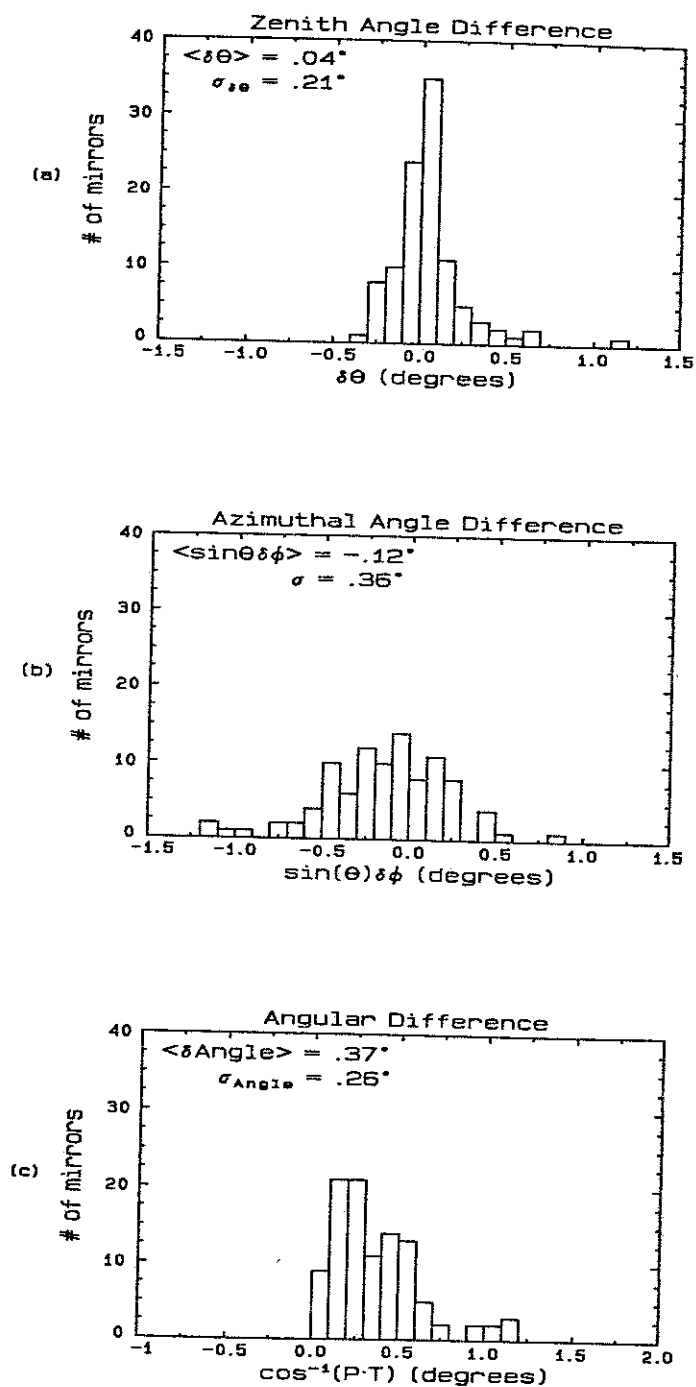
Figure 4.6—The difference in mirror residuals calculated by the photographic survey and the transit survey methods: (a) photo zenith − transit zenith, (b) (photo azimuth − transit azimuth)·sin(zenith), (c) the angular difference between the two mirror center vectors.

agreement is so good, no attempt has been made to determine the alignment more accurately for mirrors that disagree.

4.3.3.4 Monitoring Mirror Alignment

The mirror alignment can drift due to slipping motor breaks and other reasons, so it is important to continually look for changes in the mirror directions. For this reason, a level is placed on the outside of the can holding the mirror. When the actual mirror position is determined from the survey, the level is set. During the data run, each operator manually inspects the mirror directions by monitoring these levels. If the can is off by more than $1/4°$, then the operator adjusts the can's position back to its proper place.

4.3.3. Relative Timing Accuracy

The relative timing is fundamentally limited by the clock speed (20 Mhz) to 50 nsec. If the pulses entering the OMB are large enough, then this is the relative timing accuracy of each channel. However, for real events, the resolution can be significantly worse if the signal is small. This degradation of timing resolution is seen by doing a simple experiment.

4.3.3.1. Measuring the Timing Resolution

To observe firing time fluctuations, a series of short laser pulses is made at the same geometry but with different beam intensity. This way many important variables such as

attenuation, actual tube aperture crossing points, etc. are held constant. The only varying parameter is the amount of light hitting the tube, and hence, the pulse height of the incoming signal to the OMB. The geometry and, to first order, the pulse width are the same. (This test can also be done with the xenon flashers since the light output naturally varies by about 10%, but the dynamic range is not as great as the nitrogen laser used.)

If the clock resolution limits the large pulse signals, then a histogram of the relative firing time of one tube with a large measured integral relative to another tube that also has a large integral should show a narrow time distribution. Such a distribution is shown in Figure 4.7(a), which consists of relative timing plots for such a configuration. The plot is a scatterplot of a channel 2 integral vs. relative firing time, so the constancy with respect to pulse height can be seen. (Remember, the pulse width is constant for the different laser shots in the same tube since the geometry is the same, so the pulse height is proportional to the total integral.) Each point in Figure 4.7(a) represents one laser shot, so most of the time, the relative time in which the two tubes trigger is within 50 nsec. The standard deviation is, in fact, 47 nsec. Assuming the firing time for tubes 8-8 and 8-14 varies by the same amount, then the standard deviation for each tube is extracted from addition in quadrature to be 33 nsec.
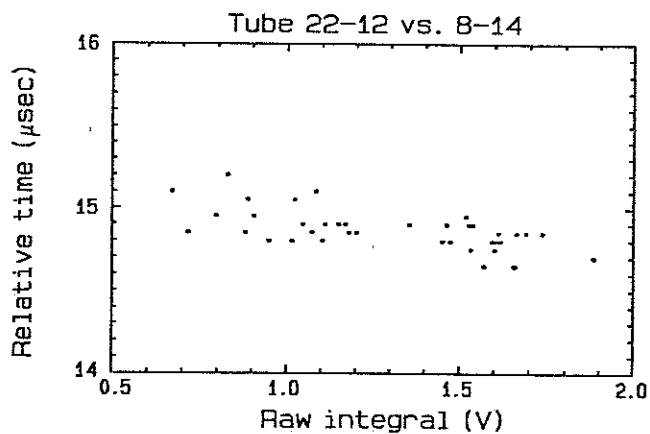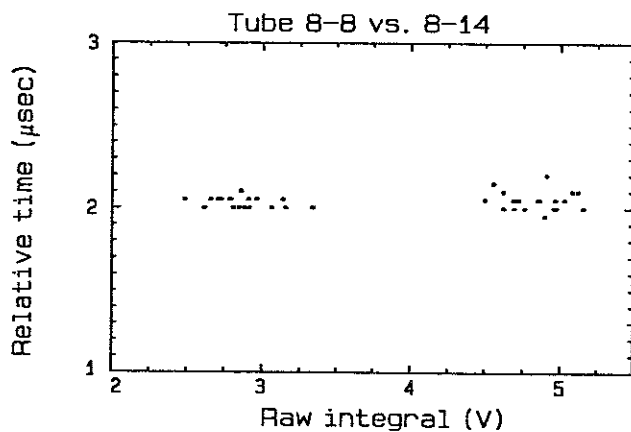
Figure 4.7—Measurement of timing resolution and demonstration of time slewing. In (a), there is no time slewing, since the pulses are large. The firing time is the same to within 50 nsec for repeated firings of the laser. In (b), a distinct delay in firing time occurs when the pulse height is reduced. (The tube relative firing times are measured with respect to the same reference tube, 8-14.)

In most instances where the signal is large, the 25 nsec resolution is reached as shown in Table 4.3 that gives the average time variance for a subset of tubes in this particular set of laser shots with R_p=4.2 km and ψ=34.8°.

4.3.3.2. Observation of Pulse Slewing

Figure 4.7(b) shows a graph for a different tube in the same set of laser shots. The times are measured relative to the same reference tube (8-14). In this case, however, one sees that the firing times are not constant, but they have a correlation with the channel 2 integral. The pulse slewing is readily seen. The firing time occurs later with decreasing amplitude. In general, the slewing effect will be a function of the pulse shape, and so will also depend on the signal width (and, therefore, the geometry of the track) as well as the firing channel integral. The Appendix details time slewing corrections.

The graphs are qualitatively consistent with the model used for the actual signal pulses, i.e., the trapezoid. For signals with large pulse height (relative to the triggering threshold), the slewing effects are small and can almost be ignored. An integral that is only slightly smaller will only have a lower pulse height plateau. The rise time of the signal remains constant. For smaller heights relative to the triggering threshold, this is no longer the case. Signal fluctuations become significant for these smaller pulses as does the contribution to the slewing from the

Table 4.3. Average tube data for a set of laser shots from a distance of 4.2 km.

Mirror-tube	$<time-t_0>$ (nsec)	$<Integral>$ (Channel 2) (mV)
48-12	-1103 ± 180	599 ± 235
48-11	-602 ± 352	454 ± 280
8-14	0 ± 0	4755 ± 1255
8-13	753 ± 57	3285 ± 849
8-10	1315 ± 248	164 ± 208
8-9	1427 ± 42	3292 ± 867
8-8	2041 ± 47	3883 ± 995
22-14	11209 ± 62	1343 ± 332
22-13	12845 ± 77	1993 ± 537
22-12	14865 ± 119	1295 ± 328
22-8	16629 ± 202	566 ± 191
21-14	18208 ± 282	652 ± 333

electronic triggering filter. In this case, the timing resolution is not the 25 nsec that is quoted, but it can be significantly worse (4 or 5 clock tics in some cases). So, quoting 25-50 nsec is somewhat misleading. It represents the optimal resolution. The resolution is a function of the geometry and signal strength as well.

4.3.4 The Energy Calibration

The photoelectron yield of a given FE channel must be converted into the number of incident photons to determine (with the reconstructed geometry) the number of fluorescent photons from the EAS. This is done by comparing every channel's detection efficiency and gain to an absolute measurement of a standard channel. In this way, the absolute calibration of each channel can be monitored over time by a relative calibration made during the Fly's Eye

STEP 1

Standard mirror
and cones are
installed in the
standard 'can.'
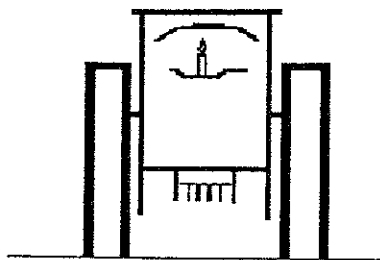
STEP 2

Standard candle
'flashed.' Tube
voltages adjusted
to give uniform
response.
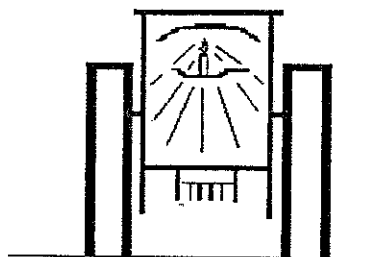
STEP 3

Standard tube placed
in cluster. Voltage
adjusted to give same
signal as other tubes.

Standard
gain read
from
graph.

G

V
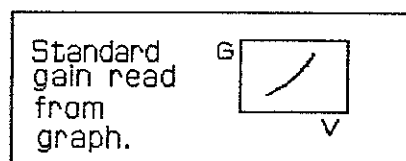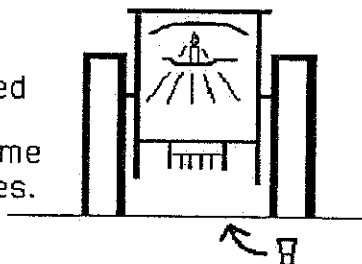
Figure 4.8—Calibration procedure diagram.

STEP 4
Roving candle response
calibrated to
standard candle.
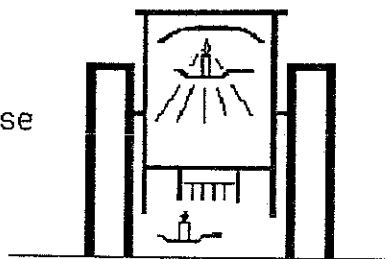
STEP 5
Local candle response
calibrated to
roving candle.
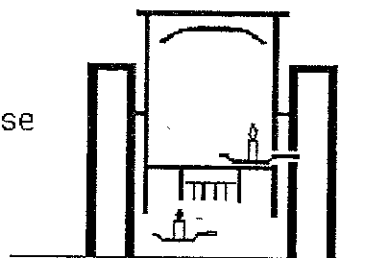
STEP 6
Local candle
monitors response
during run.
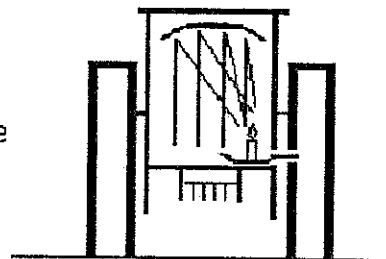
Figure 4.8. (Continued).

to voltage output conversion factors. The PMT gain is known to ± 10 % while all the other factors are known to 1 %. The absolute gain is given by the equation

$$G = V/N_{pe} = e \; G_{PMT} \; G_{OMB} \; Z_0 \qquad (4.1)$$

where Z_0 is the effective trans-impedence, G_{OMB} the ommatidial board conversion factor from input voltage-time integral to output voltage, G_{PMT} is the tube and preamp gain, and e is the electron charge. Table 4.4 lists the values for absolute gains. The PMT gain has changed over the years due to other detector changes. The UV-pass filters allowed a fourfold gain increase, while the installation of anodized mirrors forced a reduction in gain. The different values used to date are given in the table.

From the gains and efficiencies, the absolute number of photons collected by the mirror is calculated. The total number detected in a given triggered signal is

$$N_{\gamma i} = V_i / (\epsilon \; G \; \eta_{opi}) \qquad (4.2)$$

where V is the voltage from the charge integrator and η_{opi} is the gain·efficiency for the channel relative to the absolute $\epsilon \cdot G$:

$$\eta_{opi} = \epsilon_i \cdot G_i / \epsilon \cdot G \; . \qquad (4.3)$$

Hence, if the channel had the exact same values for the gains and efficiencies as the standard channel, $\eta_{opi} = 1.00$.

Table 4.4. Phototube gains for FE1 and FE2 measured during calibration.

Parameter	Value
G_{OMB}	$(2.725 \pm .027) \ 10^6 \ sec^{-1}$
Z_0	$(43.4 \pm .4 \ k\Omega)$
Gain (FE1)	
11,81	$(4.0 \pm 10\%) \ 10^4$
10,83	$(3.5 \pm \quad) \ 10^4$
5,84	$(3.38 \pm \quad) \ 10^4$
11,85	$(16.6 \pm \quad) \ 10^4$
7,87	$(14.2 \pm \quad) \ 10^4$
1,88	$(14.2 \pm \quad) \ 10^4$
7,88	$(14.2 \pm \quad) \ 10^4$
4,89	$(14.2 \pm \quad) \ 10^4$
Gain (FE2)	
9,86	$(16.6 \pm 10\%) \ 10^4$
8,87	$(14.2 \pm \quad) \ 10^4$
1,88	$(\quad " \quad) \ 10^4$
7,88	$(\quad " \quad) \ 10^4$
4,89	$(14.0 \pm \quad) \ 10^4$

Of course, the standard tube must be calibrated. How the PMT gain is determined is addressed after the relative normalization is explained.

4.3.4.2. Relative Channel Normalization

The relative efficiencies, η_{opi}, are determined by a standard candle of sorts which is moved to each mirror during the calibration procedure. The standard candle used initially was a set of NaI crystals coupled with Cs^{137} samples. These could be mounted directly above the PMTs in their cluster arrangement. This setup gave a 660 KeV γ-ray induced optical flash from the NaI, which were then detected by the PMT directly. The PMTs high voltages were then

adjusted until the pulse height distributions from each PMT were within 1% of each other giving an equalized PMT response for the cluster. The mirror and Winston cone efficiencies were not included.

After the installation of the UV-pass filters (Section 4.4), the $NaI-Cs^{137}$ method could no longer be used, since the filters were placed above the Winston cones blocking the place where the crystals were positioned. Because of the obstruction, another method was employed. The new method uses one of the Argon flash bulbs which is used in monitoring changes in the calibration (next section). It is placed near the mirror center instead of directly on top of the PMT cluster. The bulb is then pulsed giving a near uniform beam incident on the cluster plane (now covered with UV-pass filters). Tube voltages are adjusted as in the old method until their distributions are within the 1% tolerance. Note that this method includes the UV-pass filters and the Winston cones whose efficiency could conceivably drift with time. However, because the filters were installed, the cones have not degraded as fast, so this is not a big problem. No significant wear on the filters has been observed either.

The standard candle brings all PMTs to the same response at calibration. At calibration time, a standard mirror and standard Winston cones are installed at one of the mirror units at each eye. After the PMT adjusting, all tubes in that mirror now are standard channels. At this

point, the only thing not known is what their absolute PMT gain is. The absolute gain is found by replacing tubes in the cluster with the standard tube. The standard candle is flashed, and the standard tube's voltage is adjusted until its response is the same as response of the tube it replaced was when it was in the cluster. Now the gains of all the tubes in the cluster are known, and they are all the same as the standard tube's gain to within 5%. The procedure of switching the standard tube with a tube in the cluster is done with a few tubes in the cluster to ensure the stability of the measurement. The absolute gain of the standard tubes has been measured in the laboratory.

4.3.4.3. Monitoring Changes in Calibration

Two problems remain. There is the problem of normalizing all other mirrors to the standard channel, and there is the problem of monitoring the system response over time. Only the standard mirror has been completely normalized so far. The other mirrors have only had the relative response of the tubes equalized. The efficiency of the mirrors and cones for the remaining units is still unknown. Plus, it is essential to monitor the calibration drift. (Changes in calibration occur because of tube gain drift, mirror degradation, and, to a lesser extent, Winston cone degradation and filter degradation.) These problems are resolved with the aid of a roving optical pulser and a pulser installed locally inside each mirror unit.

Recall that the relative efficiency of a channel at any time t is given by

$$\eta_{opi} = \epsilon_i \, G_i / (\epsilon \, G). \tag{4.4}$$

It is impossible to monitor the absolute sensitivity of each mirror and tube at all times, the efficiency is monitored by noting changes in the relative calibration via local optical pulsers situated in each mirror system. Each local pulser is calibrated relative to a roving pulser that is taken from the standard mirror to all the other mirrors at the time of calibration.

Because only relative measurements are done, the relative efficiency at any time t of mirror i is given by

$$\eta_i(t) = \frac{RP_i(t)}{RP_{st}(0)} \tag{4.5}$$

where $RP_i(t)$ is the response of a roving pulser at time t. Now, the trick is to calibrate each mirror's optical pulser (local standard candle) against the roving pulser at t=0. This way, the tube's response relative to the roving pulser can be monitored if a local calibration is done, because:

$$\frac{OP_i(t)}{RP_i(t)} = \frac{OP_i(0)}{RP_i(0)} \tag{4.6}$$

where $OP_i(t)$ is the optical pulser response in mirror i at some time t after calibration. (All the formula says is that both the optical pulser and the roving pulser give a

photon intensity which do not change with time.) Now, multiplying equation 4.5 by 1, we get

$$\eta_i(t) = \frac{OP_i(t) \cdot RP_i(t)}{OP_i(t) \cdot RP_{st}(0)} \ . \tag{4.7}$$

This can be rewritten as

$$\eta_i(t) = \frac{OP_i(t)}{OP_i(0) \cdot RP_{st}(0)/RP_i(0)} \tag{4.8}$$

by using equation 4.6. If the changes in η_i can be monitored over time (which they are by nightly optical pulser calibrations done by the operator), and, if at calibration the ratio of tube response from the optical pulser and the roving pulser is measured as well as the roving pulser of the mirror with the standard mirror, then the absolute calibration of each channel is done.

Figure 4.9 shows $\langle\eta_i(t)\rangle$ for FE1 and FE2. There are some rather distinct features in the plots. The most dramatic change occurs at 7,87 for FE1 and 8,87 for FE2. These are the dates the new anodized mirrors were installed at the two sites.

Another interesting feature is the rise in efficiency during the winter months. This is a real effect! It is because the phototube quantum efficiency has a temperature dependence. Other discontinuities in the graphs typically correspond to times when mirrors were changed or washed, and/or when a calibration was done.
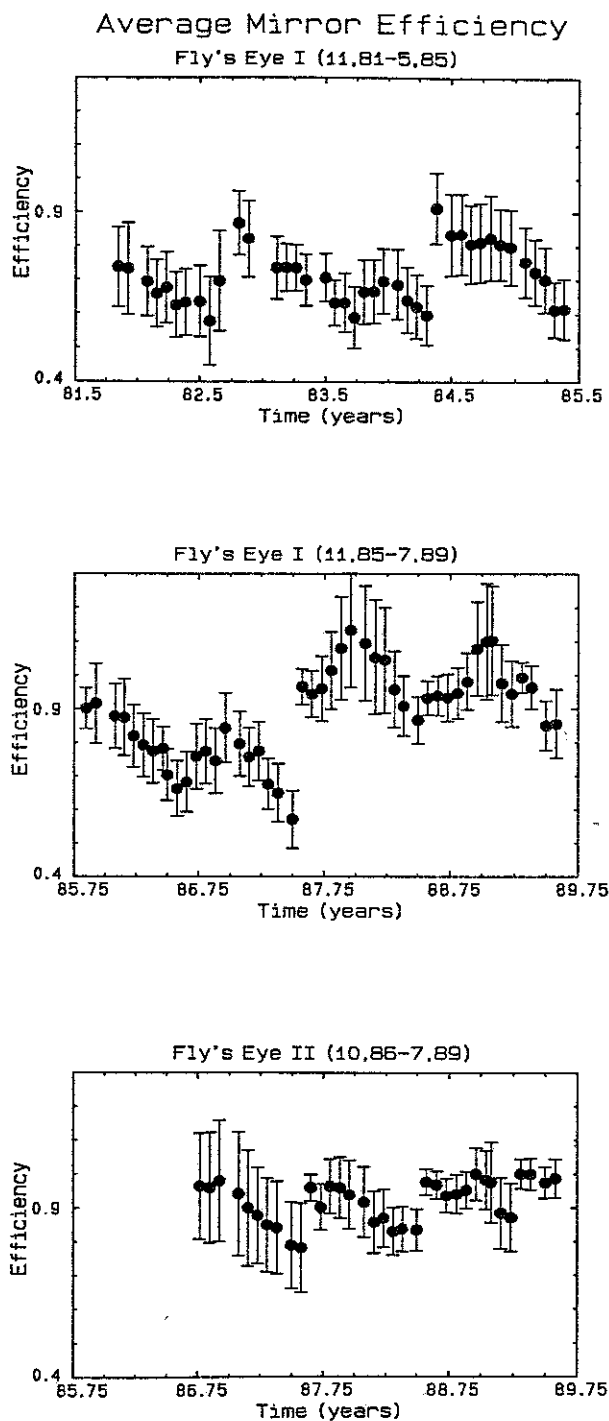
Figure 4.9. Average mirror efficiencies for FE1 and FE2. The discontinuities show mirror changes and/or recalibration. Note the relative stability since anodized mirrors were installed in July (FE1) and August (FE2), 1987. The error bars represent the spread in the efficiency values for each detector and not the statistical error.

4.3.4.4. Laser Calibration

Three different nitrogen lasers (337.1 nm) have been used spanning a wide range of impact parameters (1-20 km). The lowest energy laser is used for close-by shots, while the most powerful laser is used for the more distant shots. Table 4.5 details some parameters of the three different lasers used for calibration.

During some nights of normal detector operation, the laser is pulsed many times at many different angles and impact parameters. These pulses of light simulate fairly well (though not exactly) EAS propagation through the atmosphere. Light from the beam is scattered in the directions of both FE1 and FE2. The Fly's Eyes record the light pulses as they do EAS through normal data acquisition. The light yield, measured by the two detectors and adjusted for attenuation and solid angle corections, is then used to calculate the number of photons in the laser beam. This correction relies on knowledge of Rayleigh and Mie scattering models.

The actual amount of light in the beam is determined by splitting the beam sending a small portion (8%) into a radiometer that records the amount of light in each laser shot. The actual number determined by the radiometer is then compared with the number determined with the Fly's Eyes. Figure 4.10 shows the ratio of the expected amount to the observed amount of light in the beam. One sees an offset of only 6% between the Fly's Eye observation and the

Table 4.5. Lasers used to calibrate the Fly's Eyes.

Laser #	Approx. Energy	$<R_p>$ (km)	Equivalent N_e (Approx.)
1	.05 mJ	1.5	10^8
2	.2 mJ	7.	$4 \cdot 10^8$
3	3. mJ	15.	$6 \cdot 10^9$

measured pulse. The actual systematic error estimated from measurements taken on site are ±15%. Note that the offset is constant over the emission angle range shown (Figure 4.10(b)). This leads us to the conclusion that the offset is due to a systematic offset between the laser calibration and the absolute gain calibration.

That the agreement between observed and predicted is so good is quite encouraging. Among other things, it implies that the Rayleigh and Mie scattering corrections are done properly.

The laser can be used to calculate and test not only the Rayleigh and Mie scattering corrections, but also the geometric reconstruction algorithms, because the wavefront is traveling at the speed of light just as the particles in the air shower are.

4.3.4.5 Flasher Monitoring

The long-term drift of the calibration can be checked with xenon flasher units strategically placed around FE1 and which give a short flash of light hourly (Figure 4.11).
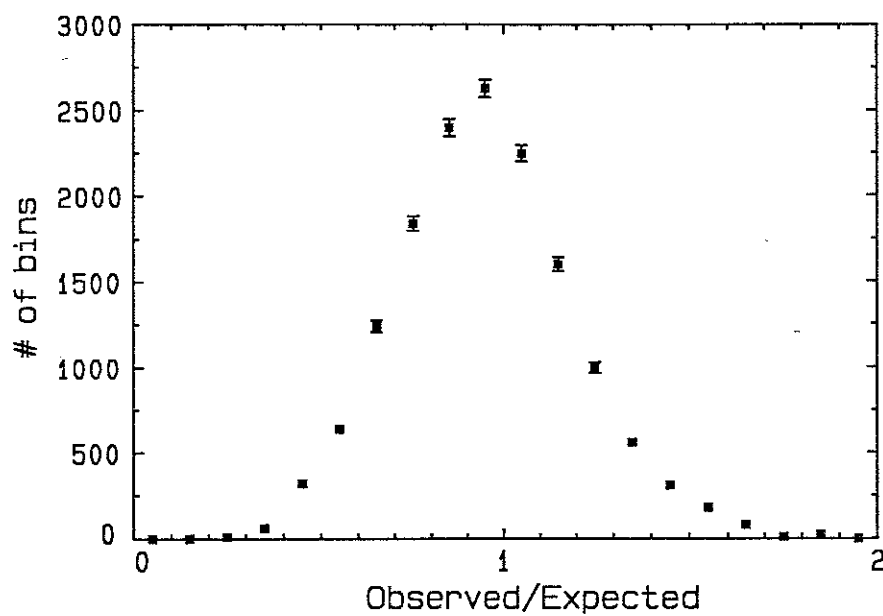
(a)

Figure 4.10—Ratio of observed to expected light from the nitrogen laser. (a) A histogram of all shots and emission angles. (b) The ratio as a function of emission angle.
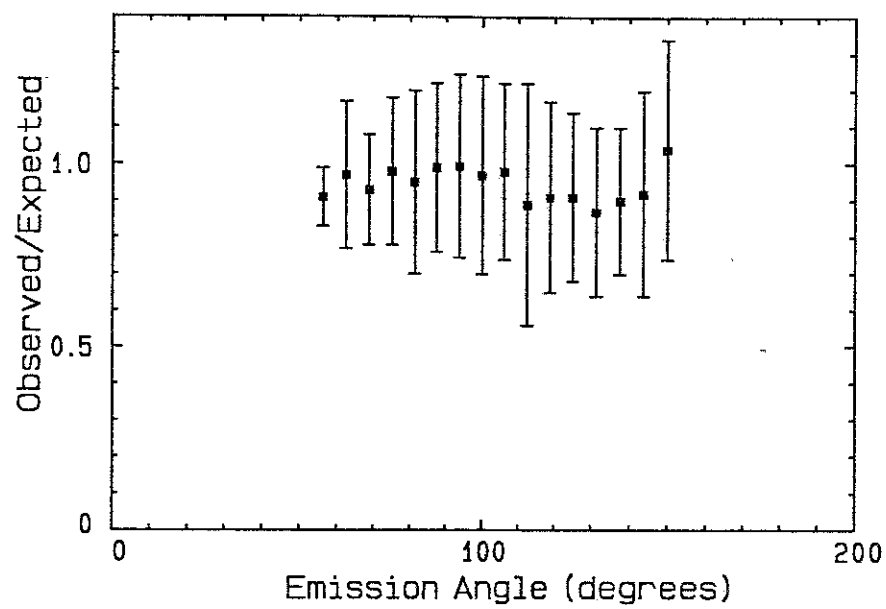
(b)

Figure 4.10—(Continued).

(They are also detectable by FE2.) The light source is known to be constant to within 20% on a shot by shot basis. However, larger differences are seen due to external effects such as frost accumulation on the flasher windows, ground haze, scattering of light from nearby clouds, etc. Figure 4.11 show the monthly average of the total amount of light detected by all the tubes in 2 specific mirrors at FE1 and FE2 since the xenon flashers were installed. There are definite long term trends present in the data. The most noticable deviation occurs during the period from 9,86 to 7,87 at FE1 and to 8,87 at FE2 where a decrease in light is seen relative to the later data. It is no coincidence that the light intensity increased dramatically when new mirrors were installed. This slight drift in calibration was because the local light pulsers failed to adequately track the mirror degradation during that period. The principal reason for this tracking problem is that the optical pulsers installed after the UV-pass filters did not sample the entire mirror, and as the mirrors degraded, the calibration slipped. A similar slipped occurred when Channel 2 at FE1 was removed.

Since the flashers have been monitoring the true degradation, a full correction is possible to rectify the slight drift. For the analysis here, only average values for a specific data set (Epoch) and Eye are used. Table 4.6 gives the renormalization constants determined from a large sample of flasher data for both Eyes and different time

FE1 <P.E. in Mirror 41>   Flasher 16

(a)
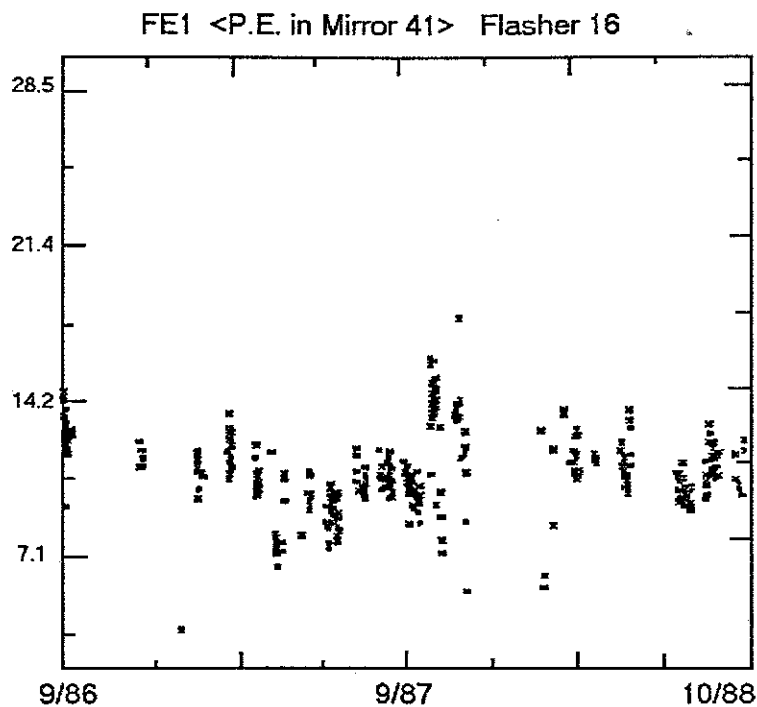
Figure 4.11—The total amount of detected light (photo-electrons·10^3) from a constant light source (xenon flasher) detected by tubes in (a) mirror 40 at FE1 versus time and (b) mirror 21 at FE2 versus time. If the calibration has been properly done, then no variation with time should be seen. Winter months have been disgarded due to frost accumulation on the flasher windows.

FE2   <P.E. in M21>   Flasher 05
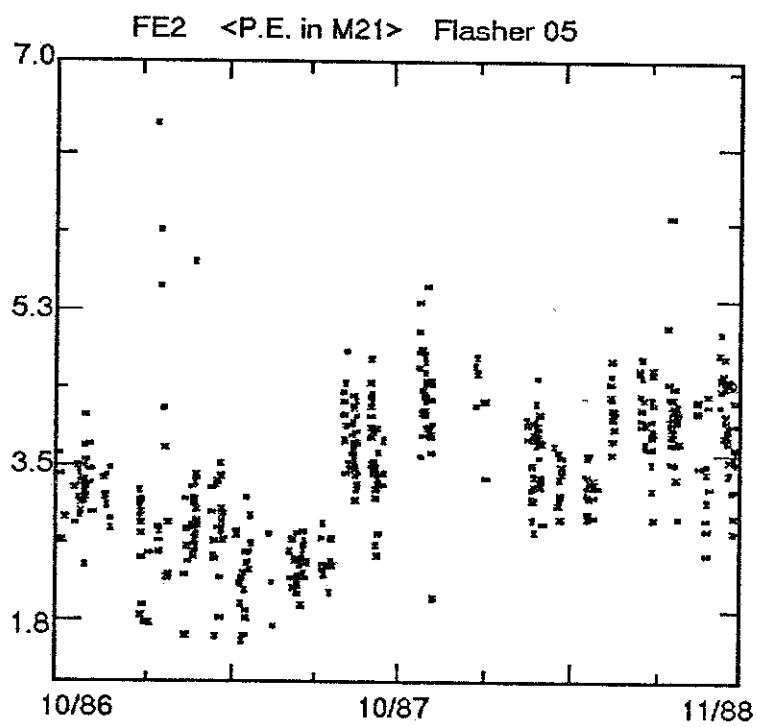
(b)

Figure 4.11—(Continued)

Table 4.6. Renormalization constants for different running periods and for both Eyes as determined by xenon flashers.

Period	FE1	FE2
11,85 − 6,87	1.25	1.25
7,87	1.0	1.25
8,87	1.0	1.0
8,88-present	1.15	1.0

periods. Data taken during the respective period have been adjusted to correct for this calibration drift.

For data preceding the flasher installation and the UV-pass filter installation, the drifts cannot be as severe for two reasons: (1) the mirrors were resurfaced with their aluminum coating more frequently, and (2) the optical pulser installed at that time sampled more of the mirror than did the postfilter pulser.

4.3.4.6 FE1-FE2 Cross Calibration

The final comparison is made by comparing FE1 and FE2 data from actual EAS. Tracks are selected with $R_p > 1.5$ km to ensure good reconstruction and reduced Cherenkov contamination. The actual tracks of EASs are broken up into equal angle bins (as seen by FE1). The total amount of light seen by FE1 and FE2 in the bins with emission angle > 40° are compared—again to reduce the amount of Cherenkov contamination. The log of the ratio of FE2 to FE1 is plotted in Figure 4.12. The different figures are to ensure no large systematic offsets are seen during the different running conditions. One sees in the last period
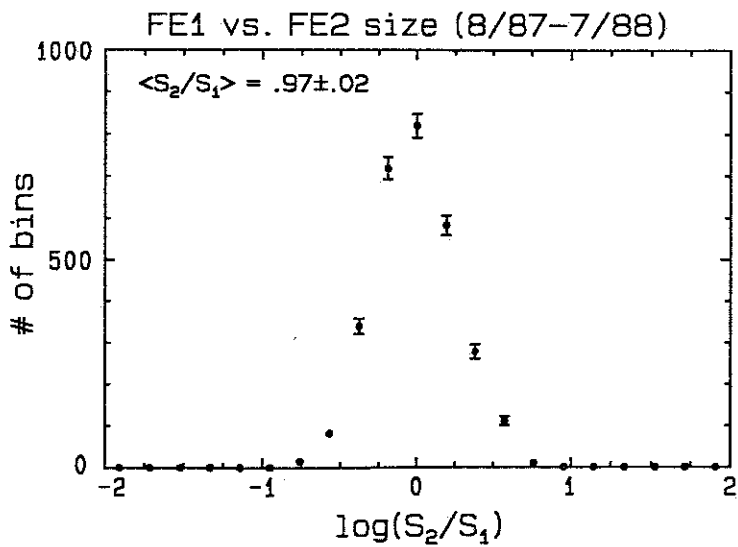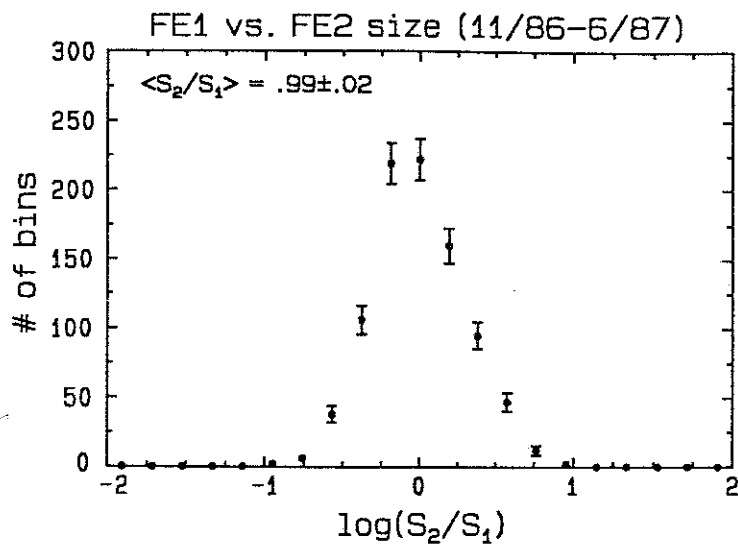
Figure 4.12—FE1 vs. FE2 EAS output for different periods.

FE1 vs. FE2 size (8/88-6/89)

$\langle S_2/S_1 \rangle = 1.11 \pm .02$

# of bins

$\log(S_2/S_1)$
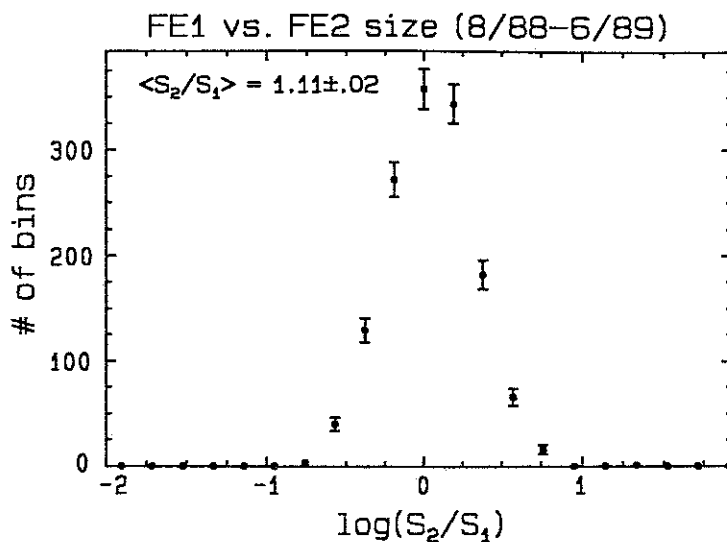
Figure 4.12—(Continued).

that there is an 11% difference between FE1 and FE2. This
is consistent with the flasher data (above) if FE1 has
drifted by 15%. This relative gain difference is corrected
in the analysis, but was not corrected for the FE1-FE2
cross-calibration check that is plotted in the figure.

From the four different methods of checking the energy
calibration, it is safely said that the systematics of the
photometric calibration is understood at the 10% level. The
remaining item for adequate energy determination of EASs is
the geometric reconstruction to be discussed in Chapter 5.

4.4. Outline History of the Fly's Eye

The Fly's Eye has had many changes during its lifetime. This section lists some of the more significant ones. These important changes are listed in Table 4.6, and are described in detail below. Most changes have improved the detectors or have helped unlock the mysteries of the Fly's Eye.

4.4.1 FE1 Data Taking for Analysis Begins

Data used for analysis starts in November, 1981, when FE1 construction of 67 mirrors was finished. Prior to November, 1981, only 48 (or less) mirrors were operating. The 67 mirrors gave 2π steradian coverage.

4.4.2 Individual Tube Threshold Adjustment

One troublesome aspect of looking at the entire night sky is the fact that some small spots in the sky are much brighter than others (i.e., stars exist). A large DC light component will raise triggering thresholds, because thresholds are adjusted to maintain a constant trigger rate. The lights from the stars and planets typically fall only into one tube. A bright object in one tube's aperture could artificially raise thresholds in the other tubes in the mirror. For this reason, the threshold adjusting was changed to the individual phototube level instead of the mirror level.

4.4.3 FE2 Prototype

The Fly's Eye 2 prototype took data from June, 1983 to January, 1985. It consisted of 8 mirrors and 112 tubes.

Table 4.6 Changes made to the Fly's Eyes over the years.

Date	Change	Purpose/Effect
11,81	FE1 construction complete.	2π steradian coverage.
2,83	Individual tube threshold adjustment	Detector more sensitive.
6,83	FE2 prototype (8 mirrors) online.	Test of stereo method.
11,85	UV-pass filter installation	Signal/noise improvement.
9,86	FE2 Expansion (36 mirrors)	Increase stereo aperture.
7,87	Mirror Anodization (FE1)	Signal/noise improvement (FE1).
8,87	Mirror Anodization (FE2)	Signal/noise improvement (FE2).
9,87	PeV 'blast' capabilities at FE2	PeV γ-ray Astronomy.
4,88	Ground Arrays operating near FE2 (Utah, MIchigan)	PeV γ-ray Astronomy.
12,87	New trigger filters at FE1	Increase detector sensitivity
8,88	Removal Channel 2 trigger at FE1	Increase detector sensitivity
3,90	CASA on-line with 500 units.	PeV γ-ray Astronomy.

The prototype was a success for it showed the tremendous advantage of using the stereo method to detect EAS.[1]

The prototype was run using FE1 as a trigger. If FE1 triggered, a strobe was sent to FE2, which was seen by a special red-sensitive tube. When the tube triggered, an interrupt would occur, and data from all FE2 tubes that had recently triggered were stored.

The prototype was also useful in verifying some EAS phenomonology. The angular distribution of Cherenkov light was directly measured.[106]

4.4.4 UV-pass Filter Installation

UV-pass filters (Hoya U-360) were installed at FE1 in September, 1985. The effect was to improve the signal to noise by about a factor of 2 (the actual improvement depends on event geometry and atmospheric transmission and is quite complicated). Figure 3.4 shows the nitrogen fluorescence spectrum with the UV-pass filter (along with the FE2 quantum efficiency response).

Data rates increased measurably, especially at the lower energies. In Chapter 6, details of the changes in the data distributions are discussed.

4.4.5 FE2 Expansion

Because stereo viewing was demonstrated to be a powerful technique, Fly's Eye 2 was expanded to 36 mirrors and 464 tubes. It began operation in August, 1986, at which point it had sufficient aperture to trigger independently of

FE1 (which it has done since). The stereo data have also been quite useful in EeV composition studies as described in Chapter 2.

4.4.6 Mirror Anodization and Changes

One major setback of uncoated mirrors is that their reflectivity decreases rapidly in the desert due to continual wear by the elements. Mirrors had to be resurfaced with the aluminum coating approximately once per year. In the summer of 1987, the mirrors of both eyes were replaced with newly aluminized mirrors. These new mirrors also had an anodized surface to protect them from weathering as quickly. They also made it possible to wash the mirrors in situ. The effect of the new mirrors is best seen in Figure 4.8, which shows the system average calibration efficiency vs. time. The time when the mirrors were installed is evident—particularly at FE1.

4.4.7 Ground Array(s) Installed at FE2

The Fly's Eye group has recently been joined by two groups from the University of Chicago[107] and the University of Michigan.[103] They have installed ground arrays around FE2 and are optimized for PeV (10^{15} eV) studies.

The surface arrays have relatively small apertures, so little EeV type physics will be done with them. However, the Michigan Muon array has a large effective aperture, since the muon lateral distribution extends over 1-2 km.

When used in conjunction with the the Fly's Eyes, the array is useful for calibration studies.

4.4.8 Cherenkov Blast Detection Capabilities at FE2

To aid in PeV studies in conjunction with the ground arrays, FE2 was retrofitted for Cherenkov Blast detection in most of its near vertical mirrors.

4.4.9 New OMB Trigger Filters at FE1

In December, 1988, the triggering filters on all three channels of the OMBs were changed from RC filters to π-section filters. This was done in an attempt to reduce the noise coincidences. The new filter has a sharper frequency cut-off, and it was hoped that this sharper cutoff would have caused a reduction of triggering threshold by further filtering of the high frequency pulses from the Cherenkov flashers from low energy (PeV range) cosmic rays. No overwhelming improvement occurred.

4.4.10 Channel 2 Removed from FE1

Another attempt was made in August, 1988, to increase FE1's sensitivity. This was the removal of the "fastest" triggering channel. A significant reduction in threshold was observed after channel 2 was removed. The reason is that the closeby Cherenkov flashes and fast ambient light were heavily filtered, so they would no longer produce single tube triggers. In fact, the threshold "bottomed out"

into the electronic noise. To remedy the situation, the
channel amplifiers were increased in gain.

The data rate changed significantly as a result of the
triggering change. The most dramatic change was the
reduction in raw data rates. Most of the close-by events no
longer triggered the system. These were mainly within the
1.5 km inner radius, so the change resulted in no
significant data loss in the spectral studies.

CHAPTER 5

EAS RECONSTRUCTION

5.1. Introduction

EAS reconstruction is a long and arduous task. It is divided into a series of steps that naturally fall into two major divisions: (1) geometric reconstruction, and (2) shower profile reconstruction. Both of these however can be further divided and are in this chapter. To add to the complexity, there are two types of reconstruction analysis: (1) single eye or monocular reconstruction, and (2) two eye or stereo reconstruction. Both are done differently and both will be discussed. Stereo reconstruction is useful for verifying monocular data, because, as we will see, stereo imaging has better resolution and is generally more robust. Unfortunately, the stereo aperture is only about 1/4 as large as the monocular aperture, and its aperture is even smaller at the highest energies, so stereo's usefulness with the present Fly's Eyes to the cutoff issue is limited.

Briefly, the geometric reconstruction begins with determining the shower plane characterized by a normal vector with zenith and azimuth angle θ_n, ϕ_n respectively. Then the distance to the shower, R_p, and the shower angle within the plane, ψ, are found (Figures 5.1, 5.2). The

SHOWER GEOMETRY
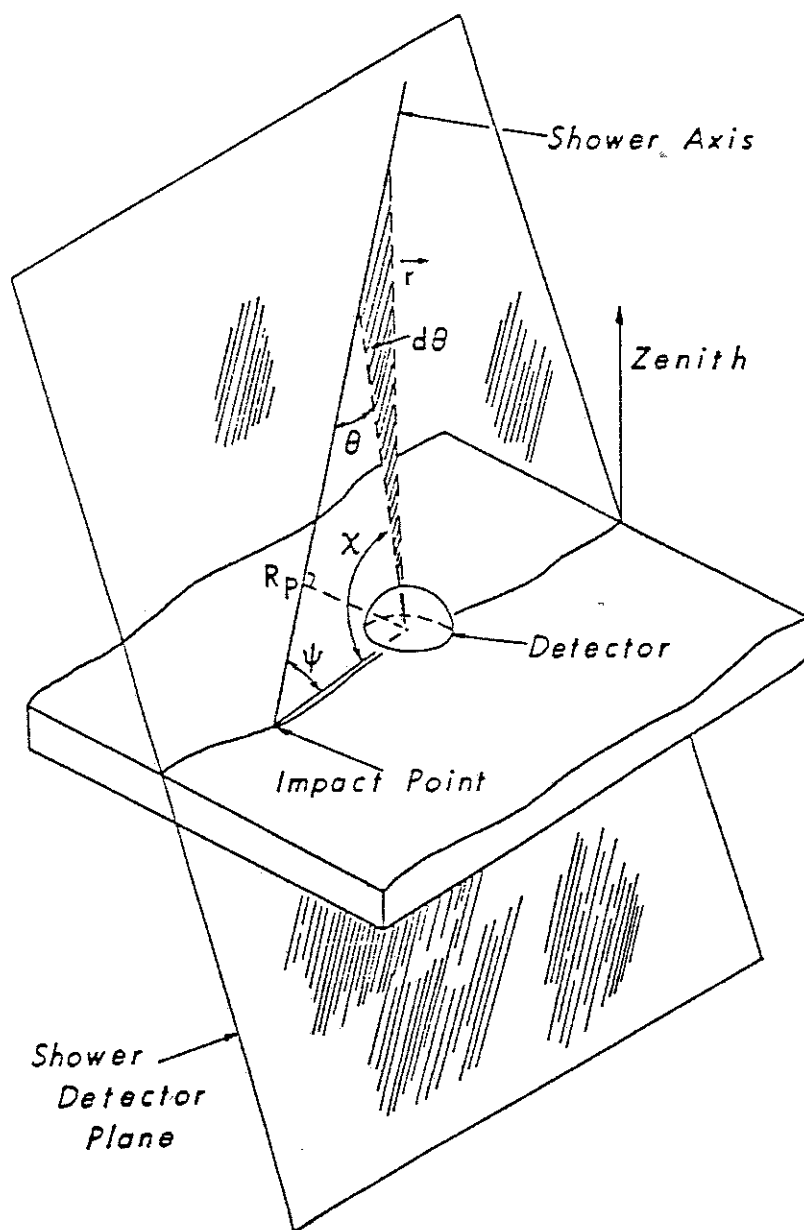
Figure 5.1—EAS geometry.
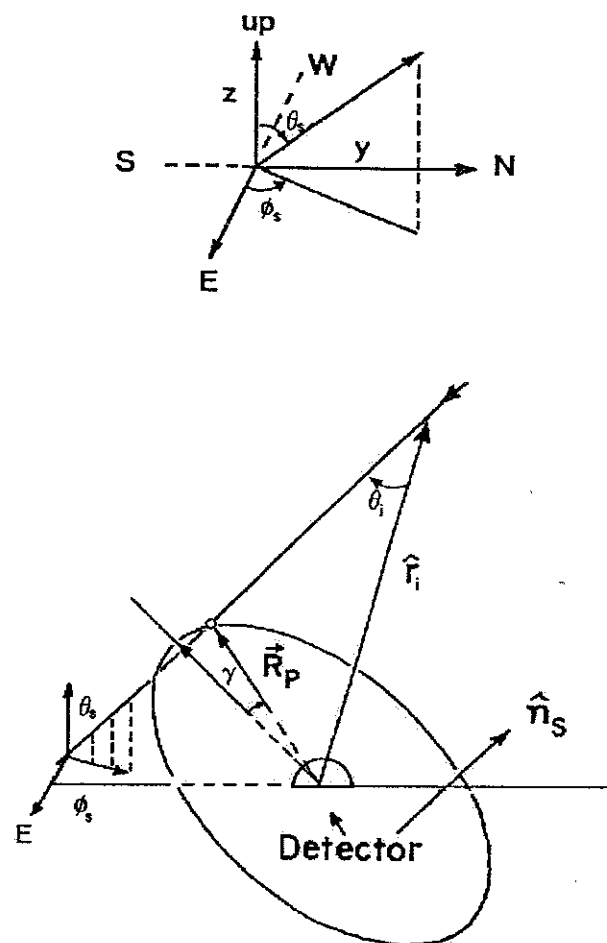
Figure 5.2—EAS geometry parameters shown graphically that are used by the Fly's Eye.

determination of R_p, ψ is different for stereo and mono reconstruction.

Once the geometry is known, the source intensity throughout the shower development can be estimated. The source intensity from the different points is then used to fit a longitudinal shower profile. Finally, the energy of the primary cosmic ray is estimated from the integral of the longitudinal profile plus small corrections that are included for the undetected components of the air shower.

5.2. The Shower Plane

For large impact parameters, an extensive air shower can be characterized as a point source of electrons (the shower core) propagating through the atmosphere tracing out a line in space. This line and the detector center (assumed not to be on the line), uniquely define a plane in space (Figure 5.1). The coordinate system used for each FE has the origin at the detector center, the x-axis pointing East, the y-axis pointing North, and the z-axis pointing up. (Stereo analysis takes the FEI center as the origin.)

Two assumptions are made: (1) the two eyes are "point" detectors, and (2) the showers are infinitely narrow showers. For assumption (1) to hold, the average (or, for that matter, the extreme) distance a mirror is from the origin is much less than the distance to the air shower. FE1 is contained in a 50 meter radius and FE2 has a smaller containment radius, so assumption (1) is reasonable for

showers at distances > 1km. Assumption (2) requires that the lateral spread of shower particles is much less than the distance to the air shower. Both of these are reasonable assumptions for showers with R_p > 2 km.

5.2.1. Determining the Shower Plane[108]

The best fit plane is found by standard chi-square minimization. Each PMT of a Fly's Eye views a small angular aperture of the night sky hemisphere. If a tube signals a detection of part of the air shower, then one knows that the shower plane passes through that tube's aperture. For the fit, one takes the tube center as lying on the shower plane which is approximately true. This way the plane normal vector is perpendicular to each tube detecting the shower. So, characterizing the plane by its normal vector, the best fit plane is found by minimizing the weighted sum of the dot product of each tube center direction vector and the plane normal vector using the constraint that the normal vector is orthonormal:

$$\text{minimize} \quad \chi^2 = \sum_{i=1}^{N_{tbs}} \frac{(0. - \mathbf{X}_i \cdot \mathbf{X}_n)^2}{\sigma_i^2} \tag{5.1}$$

subject to the constraint:

$$\varphi = 1 - \mathbf{X}_n \cdot \mathbf{X}_n = 0 \tag{5.2}$$

where $\mathbf{X_n}$ is the plane normal vector, and the $\mathbf{X_i}$s are the normalized tube direction vectors. The subscript "i" refers to the ith tube and "n" refers to the normal vector. The components of $\mathbf{X_n}$ and $\mathbf{X_i}$ are explicitly written as

$$\mathbf{X_n} = (\sin\theta_n\cos\phi_n, \ \sin\theta_n\sin\phi_n, \ \cos\theta_n) \qquad (5.3)$$
$$\equiv (A, \ B, \ C)$$

$$\mathbf{X_i} = (\sin\theta_i\cos\phi_i, \ \sin\theta_i\sin\phi_i, \ \cos\theta_i) \qquad (5.4)$$
$$\equiv (\alpha_i, \ \beta_i, \ \gamma_i).$$

where θ, ϕ are the zenith and azimuthal angles respectively of the vector. The values α_i, β_i, γ_i are the direction cosines of the ith tube.

A standard technique used for solving the constrained minimization problem is the method of Lagrange multipliers. This method is used, for it gives a simplified expression that works well computationally. We now derive what is used. Writing the Lagrange equation for each component of the normal vector explicitly for clarity, we have

$$\frac{\partial\chi^2}{\partial A} + \lambda\frac{\partial\varphi}{\partial A} = 0. \qquad (5.5a)$$

$$\frac{\partial\chi^2}{\partial B} + \lambda\frac{\partial\varphi}{\partial B} = 0. \qquad (5.5b)$$

$$\frac{\partial\chi^2}{\partial C} + \lambda\frac{\partial\varphi}{\partial C} = 0. \qquad (5.5c)$$

If the χ^2 equation is written in the form

$$\chi^2 = \sum_{i=1}^{N_{tbs}} \frac{(\ 1.0 - |\mathbf{X_n} \times \mathbf{X_i}|^2\ )}{\sigma_i^2} \tag{5.6}$$

then (after some algebra) the Lagrange equations become

$$\sum_i \{(1/\sigma_i^2)\ [\gamma_i(C\alpha_i - A\gamma_i) - \beta_i(A\beta_i - B\alpha_i)]\} - \lambda A = 0.$$

$$\sum_i \{(1/\sigma_i^2)\ [\alpha_i(A\beta_i - B\alpha_i) - \gamma_i(B\gamma_i - C\beta_i)]\} - \lambda B = 0.$$

$$\sum_i \{(1/\sigma_i^2)\ [\beta_i(B\gamma_i - C\beta_i) - \alpha_i(C\alpha_i - A\gamma_i)]\} - \lambda C = 0.$$

$$\tag{5.7a-c}$$

where the sum over i is through the number of tubes viewing the shower. With some judicious rearranging, an eigenvalue problem is found where λ is the eigenvalue and $\mathbf{X_n}$ is the eigenvector:

$$\begin{bmatrix} \sum_i \{(-\gamma_i^2-\beta_i^2)/\sigma_i^2\} & \sum_i \{\beta_i\alpha_i/\sigma_i^2\} & \sum_i \{\gamma_i\alpha_i/\sigma_i^2\} \\ \sum_i \{\alpha_i\beta_i/\sigma_i^2\} & \sum_i \{(-\alpha_i^2-\gamma_i^2)/\sigma_i^2\} & \sum_i \{\gamma_i\beta_i/\sigma_i^2\} \\ \sum_i \{\alpha_i\gamma_i/\sigma_i^2\} & \sum_i \{\beta_i\gamma_i/\sigma_i^2\} & \sum_i \{(-\beta_i^2-\alpha_i^2)/\sigma_i^2\} \end{bmatrix} \begin{bmatrix} A \\ B \\ C \end{bmatrix} - \lambda I = 0$$

$$\tag{5.8}$$

It is now argued that the eigenvector corresponding to the largest eigenvalue is the plane normal vector. (The

other two vectors lie in the EAS plane.) The easiest way to show this is to make a coordinate transformation so the normal vector is parallel to the vertical direction. In this way, all $\mathbf{X}_i$'s have γ_i's which are 0, since all tubes viewing the track have a zenith angle of 90° in this coordinate system. When this is done, the above matrix equation reduces to:

$$
\begin{bmatrix}
\sum_i \{-\beta_i^2/\sigma_i^2\} & \sum_i \{\beta_i\alpha_i/\sigma_i^2\} & 0. \\
\sum_i \{\alpha_i\beta_i/\sigma_i^2\} & \sum_i \{-\alpha_i^2/\sigma_i^2\} & 0. \\
0. & 0. & \sum_i \{-1/\sigma_i^2\}
\end{bmatrix}
\begin{bmatrix}
A \\
B \\
C
\end{bmatrix}
- \lambda I = 0.
$$

(5.9)

The eigenvalue that equals $-\sum_i \{(1/\sigma_i^2)\}$ corresponds to the eigenvector, which is the plane normal vector. Using the facts that the eigenvalues must be real, and that the sine and cosine are bounded by 1.0, it can be shown that the absolute magnitude of the remaining two eigenvalues are $< \sum_i \{(1/\sigma_i^2)\}$ by solving the remaining quadratic equation left from the characteristic equation. The algebra is left to the inspired reader.

Finding the plane normal vector now becomes a problem of finding the largest eigenvalue of equation (5.8) and its corresponding eigenvector. This is done numerically using the Power Method.[109]

5.2.1.1. Weighting

It is assumed that the shower passes directly through the tube center. In any given event, this is not exactly true. The shower will usually pass through one side of the aperture instead of directly through the tube's center. The amount of light detected by the phototube is approximately proportional to the angular distance the EAS plane is from the tube center. Thus, each direction is assigned a weight proportional to the amount of light detected. The following weight empirically gives good results:

$$Wt_i = \max \left[\frac{I_i - I_{min}}{I_{max} - I_{min}} \quad , \quad 0.1 \right] \qquad (5.10)$$

where I is the integrated signal from the PMT.

5.2.2. Plane Reconstruction Resolution

The error is estimated by using the χ^2 contour curve. $\delta\theta_p$ is the difference between the estimated plane zenith angle and the adjusted plane that corresponds to the χ^2+1 point.

The reconstruction resolution is measured directly by strobing a laser or a xenon flasher at a known geometry. The pulsed beam of photons is Rayleigh and aerosol scattered with some of the light going toward the FE simulating a real EAS.

The resolution is found by comparing the beam geometry known from survey techniques to the reconstructed geometry

obtained from the same analysis programs used for reconstructing real air showers. This is possible, because both types of light sources (air showers and a pulsed beam of photons) are approximately line sources propagating at the speed of light. Figure 5.3 shows the fitted plane resolution from laser shots.

As mentioned above, the actual resolution has a slight track length dependence. This can be seen in Figure 5.4 where a scatterplot of error vs. track length is plotted.

5.2.3 Stereo Reconstruction

For a significant fraction of the Fly's Eye EAS data set, the entire shower geometry can be determined using the fact that the intersection of two nonparallel planes is a line (which corresponds to the EAS longitudinal axis). This gives a useful redundancy in EAS reconstruction. With the planer stereo reconstruction, no timing information is needed (except perhaps to distinguish between upward and downward events). Reconstruction becomes difficult however if the opening angle between the planes is too small (of the order of 1-2 tube apertures)—i.e., when the planes are nearly parallel (Figure 5.5). This happens when a shower falls in a narrow region along the line of site between the two detectors and for very large impact parameters. A track 15 km from both eyes has an opening angle $\simeq 13°$ which is quite small. (The best opening angle for stereo reconstruction is 90°.)
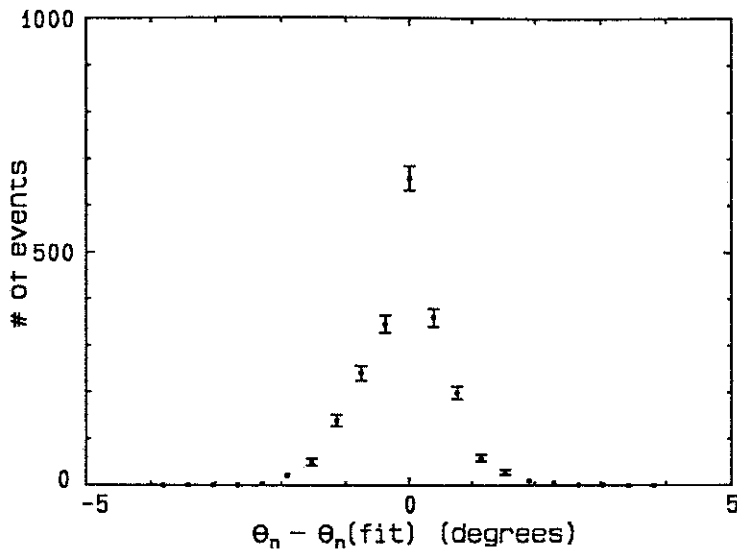
(a)
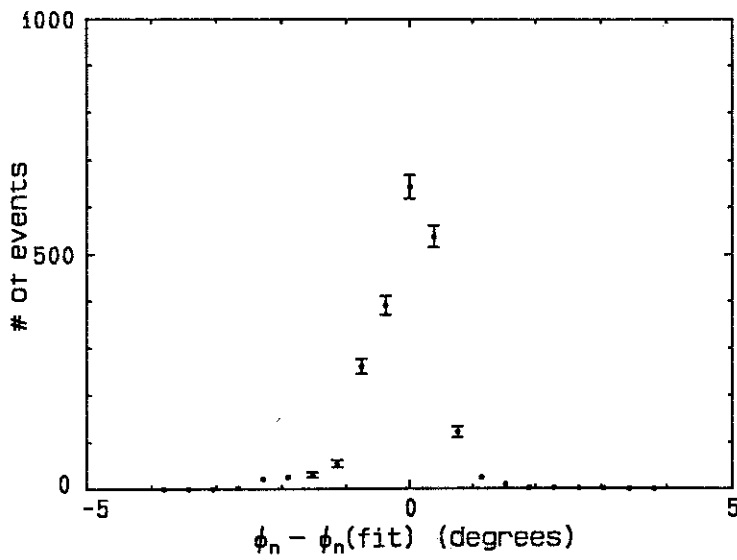
(b)

Figure 5.3—Plane parameters resolution (a) θ_n, (b) ϕ_n.
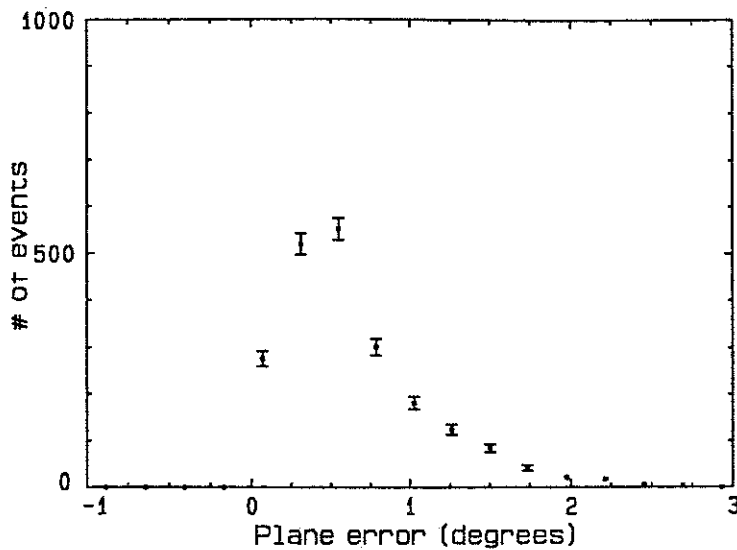
(a)
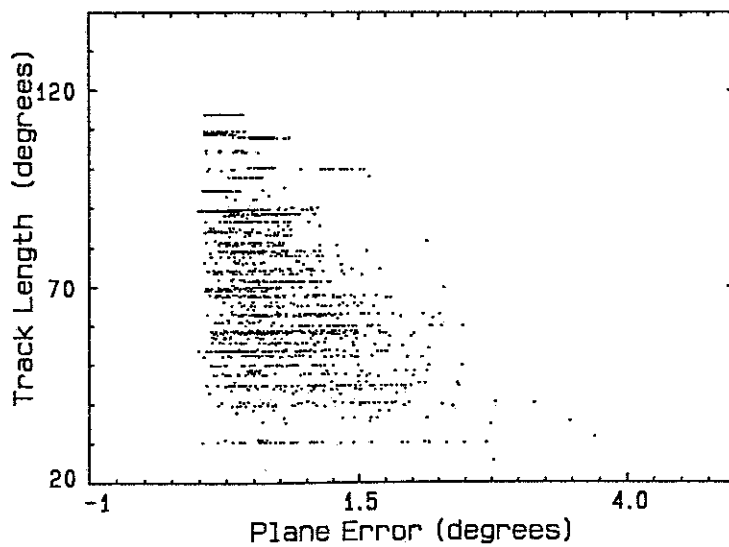
(b)

Figure 5.4—Plane angular error (a) Histogram of the angular difference $\cos^{-1}(\mathbf{X}_n(\text{true}) \cdot \mathbf{X}_n(\text{fit}))$. (b) The angular differencs vs. event track length.
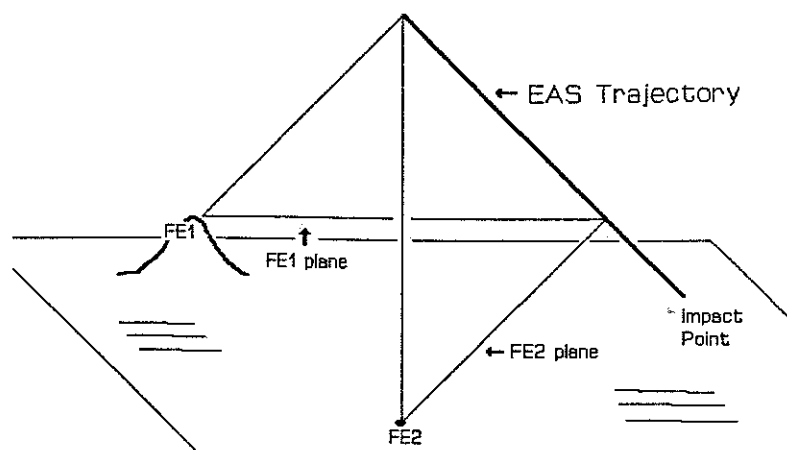
Figure 5.5—EAS geometry from stereo analysis. The EAS longitudinal axis corresponds to the intersection of the two planes determined separately in each Fly's Eye from its own tube direction vectors.

5.2.3.1. Stereo Resolution

The stereo plane fit is nearly equivalent to the mono plane fit, so no plots of plane errors are given. δR_p, $\delta \psi$ distributions from xenon flasher reconstruction are shown in Figure 5.6. The principal contributers to the uncertainty are the track length segments from each Eye and the angle between the two event planes. Cuts of track lengths > 35°, R_p > 1km, and opening angle > 30° are made.

5.3 Timing Reconstruction

5.3.1 The Timing Parameters

Given a plane in which the EAS lies, the remaining geometric parameters R_p, ψ can be found for a single Eye with EAS front arrival times from each cell. The geometric

STEREO R_p Resolution

$\langle\delta R_p/R_p\rangle = -.0004$

$\sigma_{Rp}=.02$

# of events

$(R_p-R_p(fit))/R_p$

STEREO ψ Resolution

$\langle\delta\psi\rangle = .02°$

$\sigma=.83°$

# of events

$\psi-\psi(fit)$ (Deg)
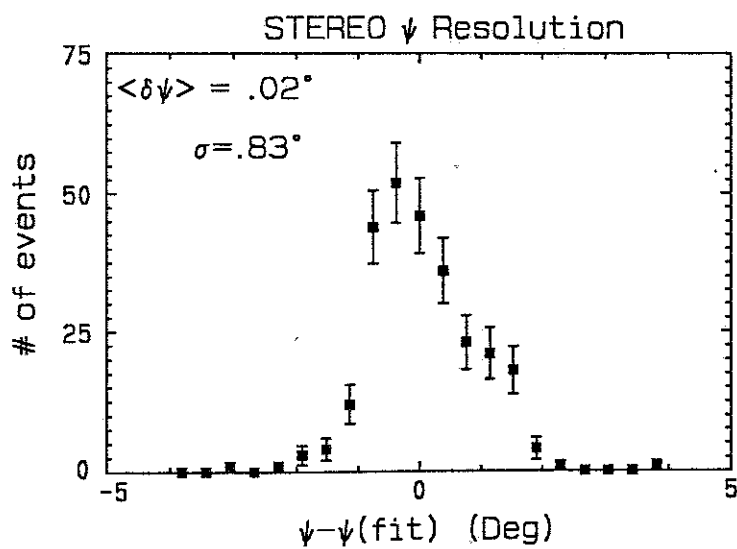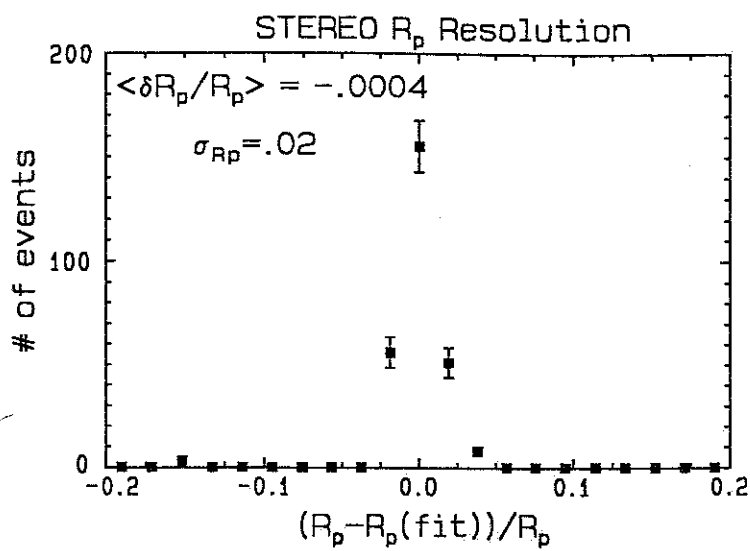
Figure 5.6—Stereo resolution from flasher reconstruction.

parameters are shown in Figures 5.1 and 5.7. The reader is encouraged to stare at them for many hours.

Projecting the tube center direction vector onto the shower plane, each tube has a unique viewing angle, χ_i, within the shower-detector plane. Light from the EAS will reach the detector at angle χ_i in time t_i where χ_i and t_i are related by the formula

$$\chi_i(t_i) = \chi_0 - 2 \tan^{-1}[c(t_i - t_0)/R_p] \tag{5.12}$$

where $\chi_0 = \pi - \psi$, c is the speed of light, and t_0 is the time the shower front plane passes through the detector origin. A derivation is given in Reference [1], and Figure 5.7 shows the geometry.

As with the plane fits, a χ^2 minimization is done, except in this case, the three fitted parameters, R_p, χ_0, ct_0, are not separable in the nonlinear equation, so the Levenberg-Marquardt method has been adopted.[110] The time χ^2 equation is

$$\chi^2 = \sum_{i=1}^{N_{tbs}} \frac{(\chi_i - \chi(R_p, \chi_0, t_0; t_i))^2}{\sigma_i^2} \tag{5.13}$$

The Levenberg-Marquardt method requires an initial guess to start the gradient search for the χ^2 minimum. To insure a good first guess, three tubes are judiciously selected and estimates of the parameters are obtained from

Figure 5.7—The Event geometry in the Shower Plane.

the model. The Simplex algorithm[111] is then used to refine the first guess. This combined algorithm of Simplex plus Marquardt minimization has proven to be very robust.

5.3.1.1 t_0 Constraint

Included directly in the minimization is the constraint that $t_0 \leq 0$. All this means physically is that the light from the shower reaches the detector after the front passes. The case that $t_0 = 0$ is the special case where the shower lands directly on top of the Fly's Eye in which case the Fly's Eye cannot reconstruct it from differential timing techniques anyway.

The way this constraint is included is straight-forward. Equation 5.12 above becomes

$$\chi_i(t_i) = \chi_0 - 2 \tan^{-1}((ct_i + a_3^2)/R_p)$$ (5.14)

where

$$a_3 = \sqrt{ - ct_0}.$$ (5.15)

The three fitted parameters are now R_p, χ_0, a_3. With this constraint, $-\infty < a_3 < +\infty$, but $ct_0 \leq 0$. The motivation for making this constraint is to ensure the parameter vector does not wander into a local minimum in an unphysical section of parameter space.

5.3.1.2 Time Slewing

The time the actual filtered signal crosses the triggering threshold on the Ommatidial board is not the time the light reaches the detector. The time difference between the light arrival time and the triggering time is called the slewing time, and it is difficult to calculate.

The corrections to the timing model consist of two parts. There is a plane adjustment to χ_i and a time adjustment to t_i. The Appendix details how this is done. Briefly, χ_{shift} is a function of the angle between the plane and tube center (elevation angle) and t_{slew} depends on the elevation angle, the geometry of the shower, the signal intensity, and the electronic signal filtering (which is different for each triggering channel). The phrase "time

slewing" in this discussion refers to both corrections and not just the time delay due to pulse slewing. With the elevation angle and timing corrections, the model equation becomes

$$\chi_i(t_i) = \chi_0 + \chi_{shift} - 2 \tan^{-1}((ct_i - t_{slew} + a_3^2)/R_p).$$

$$(5.16)$$

For the FE1 data presented in Chapter 6, a slewing correction has been done, and this represents an important change to the FE1 data analysis which was not previously incorporated. The stereo data are not affected, because no timing information is used in the stereo plane analysis data set (except determining if the shower is coming up or going down).

5.3.2 Timing Reconstruction Resolution

There are two different ways used to measure the resolution of the geometric parameters obtained from differential timing: (1) from xenon flashers, and (2) by comparison with stereo reconstruction. The comparison with stereo data is fruitful in case there is any hidden systematic with using flashers for timing reconstruction. One potential systematic is that flashers extend over the high range of $(\chi_0 - \chi_i)$ where there is significant "curvature" in the tangent function (Figure 5.8). Thus, the relative
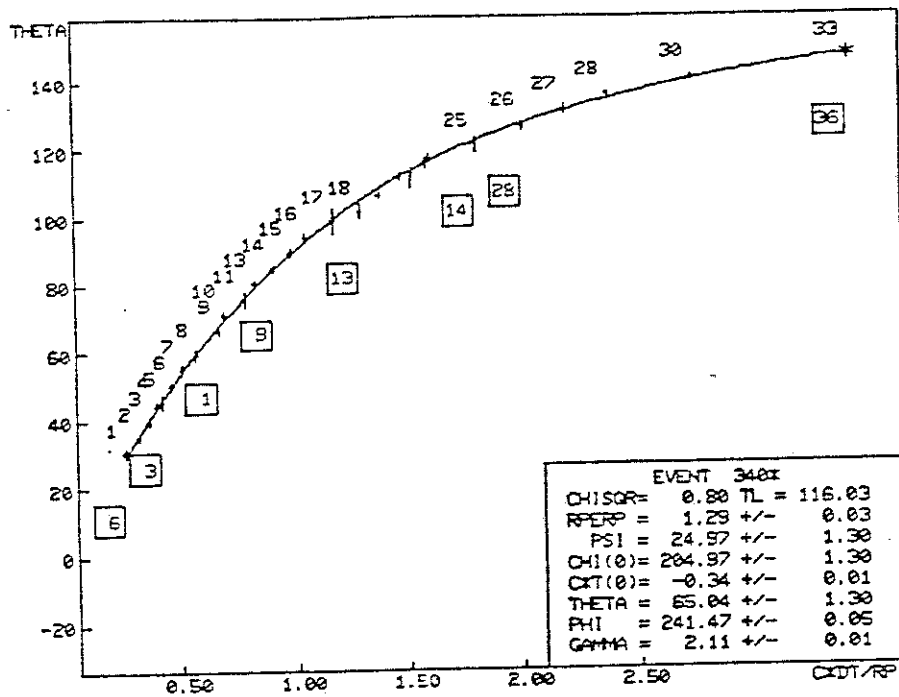
Figure 5.8—Time plot of flasher event. In the plot, $\theta = (\chi_0 - \chi_i)$ is the y-axis, and $c(t_i - t_0)/R_p$ is the x-axis.

time between adjacent tubes receiving light is large compared to the time resolution.

5.3.2.1. Flasher Reconstruction

Figure 5.9 shows the R_p, ψ resolution from vertical flashers from November, 1989. The effective track length cut is 40°.

5.3.2.2. Comparison with Stereo

The true test of single eye reconstruction comes from comparing with stereo reconstruction, since as mentioned, flashers typically sample the tail end of the arctangent curve where the time between samples is relatively large. Figure 5.10 compares R_p, ψ estimated from stereo and mono data. The offset is slightly larger than the laser shots would indicate. This larger deviation seen in Figure 5.10 versus Figure 5.9 is due to differences in the relative timing fit for flashers and real events and the difference in the track length distributions.

5.4 Shower Size[112]

To calculate the EAS size at different points along the longitudinal profile ($N_e(X_i)$) from atmospheric techniques, a series of corrections must be made to the raw photoelectric signal. Geometric corrections to the scintillation light and corrections for the directly beamed Cherenkov light are the largest ones for most EASs, but atmospheric attenuation
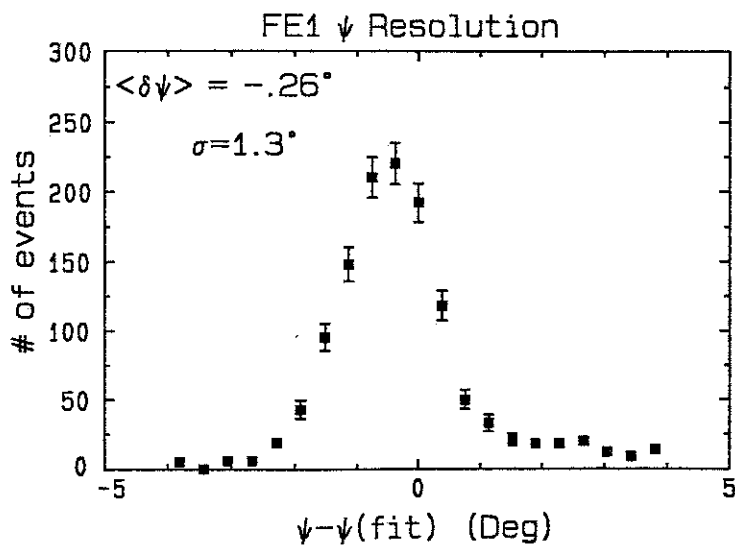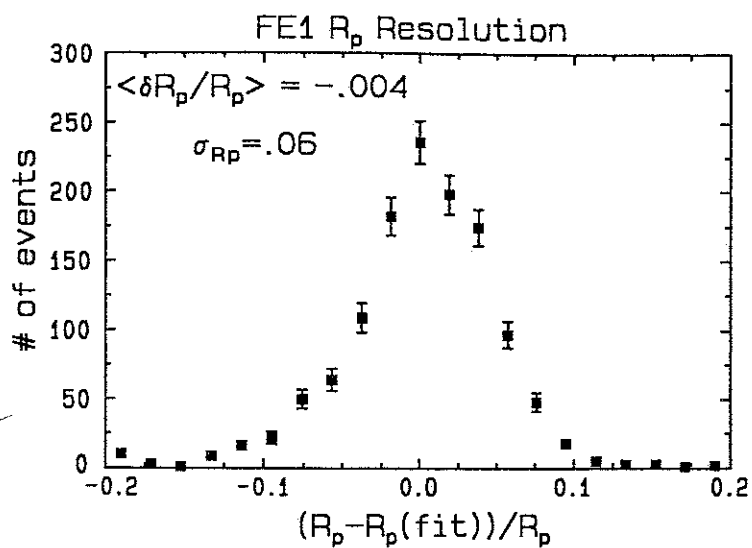
Figure 5.9—FE1 resolution (a) R_p and (b) ψ from flashers.

Stereo v. FE1

$\langle \delta R_p \rangle = .03$

$\sigma_{R_p} = .09$

# of events

300

200

100

0

-0.5   0.0   0.5

$(R_p(STE) - R_p(FE1))/R_p(STE)$

Stereo v. FE1

$\langle \delta \psi \rangle = 2.6°$

$\sigma_\psi = 8.3°$

# of events

200

100

0

-25   0   25

$\psi(STE) - \psi(FE1)$ (Deg)
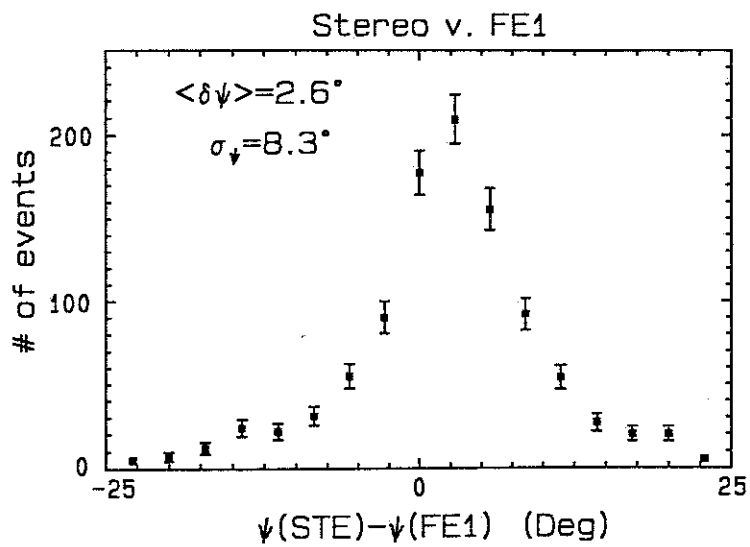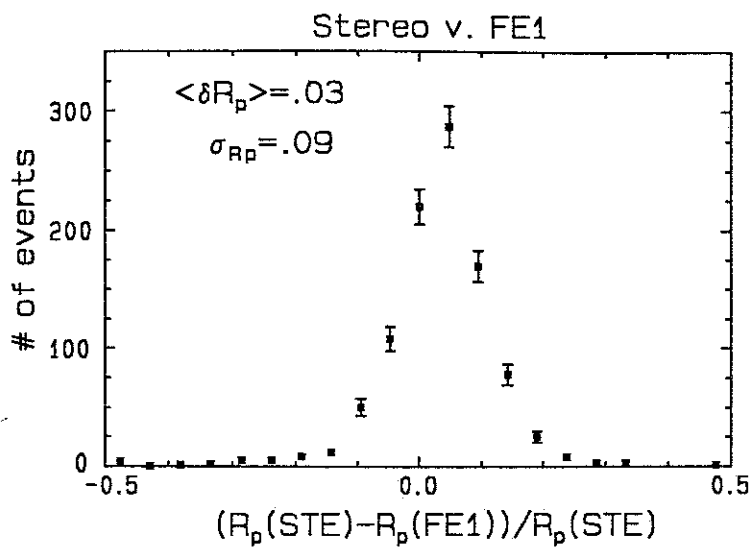
Figure 5.10—Stereo vs FE1 R_p and ψ. Note the offsets.

is also a factor. Further, substractions for the Cherenkov light that is scattered from the beam into the detector by Rayleigh and Mie mechanisms are necessary. The corrections are somewhat involved, for they all have a wavelength dependence demanding that the wavelength properties of the UV-pass filter and the tube photocathode efficiency be included in the calculation.

The situation is further complicated by the fact that the amount of Cherenkov light that is detected through the direct and scattered paths depends on knowing how much Cherenkov light there is in the beam. As outlined in Chapter 3, this depends on the number of electrons in the shower from the earlier parts of the development as well as the current number of electrons in the longitudinal point, so some estimation of the shower size is needed to calculate the size.

To adequately model these complexities, the size analysis must be done iteratively. The calculated number of electrons will depend in part on the number detected earlier in the shower. What follows is a description of how this is done. The discussion begins with how the data are combined into angular bins and how the atmosphere is modeled.

5.4.1 Combining Data into Angular Bins

Mirror spot size and true lateral spread of the shower cause the actual signal to have a transverse width to it. Although it is true that the spread due to the lateral

distribution is small for showers used in the analysis, the spot size is something we must live with in every shower. This can cause difficulties when the signal traverses near the edge of the Winston cone-tube aperture. The reflected light is then split into two or more tubes and some is lost through the cracks.

To circumvent this lateral spread problem, a sum over the lateral spread is done. The observed track is segmented into 6° angular (longitudinal) bins. The signal from any given tube is then divided proportionately into the bins it straddles. A correction is made for the lateral displacement the shower plane is from the tube-cone center, because the collecting efficiency degrades as a function of displacement from the tube center. The correction was empirically determined with the fractional amount of light detected given by

$$ f = 1.0 - 12.02 \cdot \left| \sin(X_n \cdot X_i) \right|. \tag{5.17} $$

where the range of accuracy extends out to 2.4° from the tube center.

Stereo data are handled similarly. In the stereo case, the FE1 profile is segmented into 6° bins the same as in monocular reconstruction. FE2 data are then split into variable angular bins which correspond to the FE1 6° bin. Their values can range typically from 3°-8°, though some are slightly smaller or larger.

5.4.2 The Atmosphere

For the Fly's Eye analysis, the U.S. Standard Atmosphere is used.[113] This model is adequate for the present Fly's Eye. Seldom are showers viewed at distances exceeding one atmospheric attenuation length (approximately 20 km), so subtle changes are not a major issue. The validity of the standard atmosphere has been verified by comparing it to actual radio sonde data taken from the Salt Lake City Municipal Airport. Deviations between the model and the real data are < 30 gm·cm^{-2} for heights up to 20 km. The Isothermal Atmosphere is thus a good model, though the measured deviations contribute to the systematic error of the X_{max} distribution measurement discussed in Chapter 2, but it is insignificant for the energy measurement.

5.4.2.1 Atmospheric Depth

For ease, the analysis uses slant depths to determine what the attenuation corrections are. Slant depths are relatively straightforward to calculate. Except for steeply inclined showers, the slant depth at a particular point along the shower is given by

$$X_i = X_0 \, e^{-h/H_0} \, \sec\theta_i \qquad (5.18)$$

where X_0 is the vertical depth above the detector horizontal plane (852 gm·cm^{-2} at FE1), h is the height the point is above the detector plane, H_0 is the atmospheric scale height ($H_0 \simeq 7.3$ km). The angle θ_i is the angle the slant "path"

makes with the zenith. For Cherenkov light propagating along the EAS trajectory, $\theta_i = \theta_s$, the shower zenith angle. For scattered and the isotropically emitted fluorescence light propagating from a point on the trajectory to a phototube or bin, θ_i is the tube or bin angle from the zenith (Figure 5.11).

For large zenith angles, the parameterization in Equation 5.18 fails. The way around this is to integrate over the local density as one increases in height from the observer to the source. This procedure will give the differential difference in depth for zenith angles up to $\approx 80°$ for events near the detector, but the absolute depth may be incorrect to due the Earth's curvature.

5.4.2.2 Atmospheric Attenuation

Atmospheric attenuation is generally divided into three types: Rayleigh, Mie (or Aerosol) and Ozone attenuation. For distant showers or for showers observed at large depths, the first two corrections become important. The total transmission factor can be expressed as

$$T_{ATM} = T_R \cdot T_M \cdot T_0 \tag{5.19}$$

where T_R is the Rayleigh transmission, T_M is the Mie transmission, and T_0 is the Ozone transmission factor. Ozone does not affect fluorescence appreciably.

The fraction of light in a beam which is not scattered by Rayleigh scattering is

EAS Trajectory
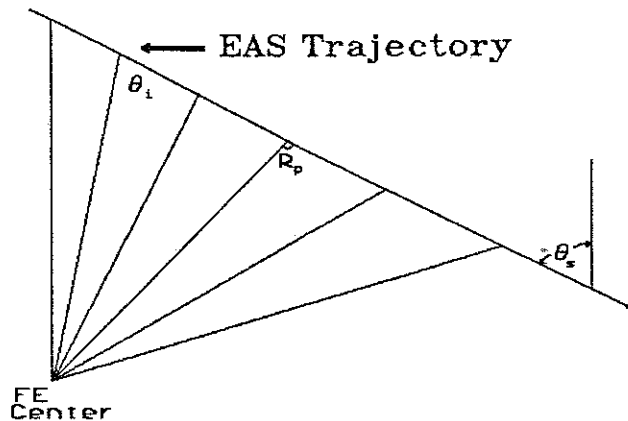
Figure 5.11—The longitudinal profile is segmented into 6°
bins.

$$T_R = \exp \left[- \left(\left| X_1 - X_2 \right| / X_R \right) \cdot \left(400 \text{ nm} / \lambda \right)^4 \right] \tag{5.20}$$

where X_1 and X_2 are the respective source and receiver slant

depths, X_R is the Rayleigh mean free path ($X_R = 2974$ g·cm^{-2})

for light with $\lambda = 400$ nm.

For Mie scattering, the transmission factor is

primarily a function of the height above the ground, because

the aerosol tends to gravitate there. For light emitted at

height h_1 and detected at height h_2, the Mie transmission

factor used is

$$T_M = \exp \left[\left(\exp(-h_1/H_M) - \exp(h_2/H_M) \right) \cdot \left(H_M \sec\theta / L_M \right) \right].$$

$$\tag{5.21}$$

where H_M is the Mie scale height ($\simeq 1.2$ km) and L_M is the mean free path ($L_M = 14$ km at 360 nm). The Mie correction is almost always small for data used in the analysis. It only affects at all the tail end of a shower seen low on near the horizon and from a large distance.

It is crucial to remember that the atmospheric transmission factor is a function of the wavelength of light. How this is incorporated is explained below.

5.4.3 Determining the Number of Electrons

To determine the number of electrons, the number of scintillation photons must be calculated, but this requires extraction of the other components from the photo-electron yield. The procedure is iterative. For any given tube (or bin), the amount of photoelectrons (P) has the four already mentioned components written symbolically as

$$P = S + C + R + A \qquad (5.22)$$

where S stands for scintillation, C stands for direct Cherenkov light, R stands for Rayleigh scattered Cherenkov light, and A stands for Aerosol (Mie) scattered Cherenkov light.

For the first bin viewing the shower, the assumption is made that the scattered Cherenkov contributions are negligible. The physical reason is that the Cherenkov beam has not had time to develop fully, so there are not many to

scatter. In this case, the number of photoelectrons detected is

$$P_1 = S_1 + C_1. \tag{5.23}$$

S_1 and C_1 are both proportional to the number of electrons in the shower:

$$S_1 = \alpha \cdot N_{e1} \tag{5.24}$$

$$C_1 = \beta \cdot N_{e1}. \tag{5.25}$$

For the first bin only, the Cherenkov component does not have the "past history" in it, because, as already mentioned, the Cherenkov beam is still too small. So, if α and β can be calculated (see below), then the number of ionizing particles in the first bin is determined:

$$N_{e1} = P_1/(\alpha + \beta). \tag{5.26}$$

The number of particles in the second and subsequent bins are not so easy, but, because the first bin is known, we can use this information to calculate the corrections necessary in these later bins. The number of Cherenkov photons in the beam in the first bin (B_1) is now calculable, since N_{e1} is known. For the second bin, some of these photons will propapate through. In addition, more Cherenkov

photons will be generated. If f_{c1} Cherenkov photons from the first bin reach the second bin, then the number of Cherenkov photons in the beam can be approximated as

$$B_2 = f_{c1} \cdot B_1 + \varepsilon \cdot (N_{e1} + N_{e2})/2. \qquad (5.27)$$

where we assume that the number of electrons is the average number of the first and second bin and that these electron have a Cherenkov *production* efficiency ε. ε is to be contrasted to β which is the Cherenkov *detection* efficiency.

Given the combined probability of scattering and detecting these Rayleigh (γ) and Mie (ζ) beamed photons, the number of detected photoelectrons in the second bin is now calculable:

$$P_2 = (\alpha + \beta) N_{e2} + (\gamma + \zeta) \cdot B_2. \qquad (5.28)$$

This now lets us solve for N_{e2} which is used for calculating the correction to N_{e3} and so on. The only problem is that we have not explicitly detailed what α, β, γ, ζ, ε, f_c are. The first four parameters are the topics of the next subsections. ε and f_c will follow from the discussion. One important point is worth reiterating here—these parameters have are functions of the photon wavelength. Thus, a sum over wavelength is necessary.

Generalizing the formulae, the number of photoelectrons in each bin is

$$P_i = (\alpha_i + \beta_i) \cdot N_{ei} + (\gamma_i + \zeta_i) \cdot B_i \qquad (5.29)$$

$$N_i = \frac{P_i - \sum_{j=1}^{Nwave} \{ (\gamma_{ij}+\zeta_{ij}) \cdot (f_{ci-1} \cdot B_{i-1} + \varepsilon_{ij} \cdot N_{ei-1}/2) \}}{\sum_{j=1}^{Nwave} \{ \alpha_{ij} + \beta_{ij} + (\gamma_{ij} + \zeta_{ij}) \cdot \varepsilon_{ij}/2 \}} \qquad (5.30)$$

The summations are over the different wavelength intervals. The sums begin centered on 280 nm and increment through in 9 nm intervals. For the filtered data, there are only 16 intervals. The filter attenuates the rest. 40 intervals are needed for data preceding filter installation.

To simplify the notation, the index i will stand for the angular bin number and j will be the wavelength interval number. Generally, it is assumed angular bin i is being discussed, so, the index i will be dropped unless the discussion warrants its inclusion.

5.4.3.1 The Scintillation Efficiency (α)

Chapter 3 details the fluorescence efficiency calculation. Here we show how to convert the number produced to the number actually detected.

The angular distribution of fluorescence light is

$$\frac{d^2N_S}{d\ell d\Omega} = \frac{N_\gamma(T,h) \cdot N_e}{4\pi} \qquad (5.31)$$

where $d\ell$ is the pathlength subtended by the bin, and $d\Omega$ is the mirror collecting area (Figure 5.12). The number of photoelectrons produced by these scintillation photons directed towards the viewing bin depends on the viewing solid angle, the track pathlength the EAS takes through the bin, and the detection efficiency and is expressed as

$$N_{pe}(S) = \epsilon_{det} \frac{d^2N_S}{d\ell d\Omega} \Delta\ell\Delta\Omega \qquad (5.32)$$

The parameter ϵ_{det} is useful to define. It includes factors unrelated to the photon source—only to the factors relating to the detection of the produced photons. The value will change with wavelength bin and is expressed as

$$\epsilon_{det} = \epsilon_{MC} \cdot T_F(j) \cdot \epsilon_{PMT}(j) \cdot T_{ATM}(j) \qquad (5.33)$$

and includes the mirror-cone reflectivity ϵ_{MC}, the photocathode efficiency ϵ_{PMT}, the filter transmission $T_F(j)$, and the atmospheric transmission T_{ATM} (defined above). Explicitly including the wavelength dependence of N_γ and the components of ϵ_{det}, the number of scintillation induced photoelectrons as a function of the number of ionizing particles in the shower is

$$N_{pe}(S) = \frac{\epsilon_{MC} \cdot \Delta\ell \cdot \Delta\Omega \cdot N_e}{4\pi} \sum_{j=1}^{Nwave} (N_\gamma(j) \cdot T_F(j) \cdot \epsilon_{PMT}(j) \cdot T_{ATM}(j))$$

$$(5.34)$$
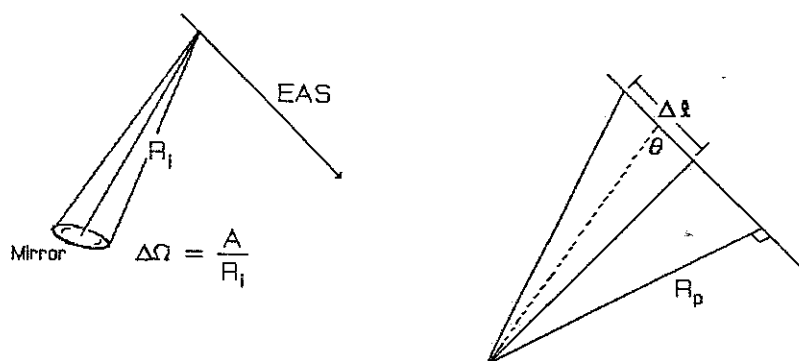
Figure 5.12—$\Delta\ell$ and $\Delta\Omega$ shown pictorially.

From geometry, the approximate path length $\Delta\ell$ and the collecting solid angle $\Delta\Omega$ are

$$\Delta\ell \simeq R_i \cdot \phi_{bin}/\sin\theta_i \tag{5.35}$$

$$\Delta\Omega = A/R_i^2 \tag{5.36}$$

$$\Delta\ell \cdot \Delta\Omega = A \cdot \phi_{bin}/(R_i \cdot \sin\theta_i) = A \cdot \phi_{bin}/R_p \tag{5.37}$$

where A is the mirror collecting area, ϕ_{bin} is the bin angle (6°), and R_p is the impact parameter. Recall that N_γ has temperature and height dependences as described in Chapter 3. Its value is

$$N_\gamma = N_{\gamma 0} \cdot [300/(T-a \cdot h)]^{-1/2} \qquad (5.38)$$

One must also include the wavelength dependences. With
this, the scintillation efficiency parameter is

$$\alpha = \frac{\epsilon_{MC} \cdot A \cdot \phi_{bin}}{4\pi R_p} \sum_{j=1}^{Nwave} \left(N_\gamma(j) \cdot \epsilon_{PMT}(j) \cdot T_F(j) \cdot T_{Atm}(j) \right)$$

$$(5.39)$$

5.4.3.2 The Direct Cherenkov Light Efficiency (β)

The Cherenkov light efficiency depends on the angular
distribution of electrons, the Cherenkov threshold energy,
and the energy distribution of the electrons in the shower.
These are quantities that depend on the viewing geometry,
the atmosphere, and the longitudinal development of the
shower.

The angular distribution of Cherenkov light follows the
form

$$\frac{dN_\gamma}{d\Omega} = \frac{\exp(-\theta/\theta_0)}{2\pi\theta_0 \, \sin\theta} \qquad (5.40)$$

where the term θ_0 depends on the threshold energy for
Cherenkov production and is parameterized by the formulae

$$\theta_0 = 0.83 \cdot E_t^{-.67} \qquad (5.41)$$

where

$$E_t = mc^2/(2\delta)^{1/2} \qquad (5.42)$$

The formulation was determined through extensive Monte Carlo techniques. Deviations from this parameterization for the Fly's Eye's energy range were found via Monte Carlos to be $\simeq$ 10%.[114] The Fly's Eye has also measured θ_0 directly,[106] and the results are in agreement with the Monte Carlo studies. Typically, $\theta_0 \simeq 5°$.

The number of Cherenkov photons produced per unit path length is calculated in Chapter 3. Recall Equations 3.26 and 3.27:

$$\delta = \delta_0 \cdot \exp(-h/H_0) \qquad (3.26)$$

$$\frac{dN_c}{d\ell} = 2\pi\alpha N_e \int_{E_t}^{\infty} d(1/\lambda) \int f(E')(2\delta - m^2c^4/E^2) \, dE' \qquad (3.27)$$

The integral over the wavelength is limited to the wavelength bins. For convience, equation 3.27 will be expressed in the form

$$\frac{dN_c}{d\ell} = 2\pi\alpha \ N_e \ G(E_t) \ \Delta\nu/c \qquad (5.43)$$

Recall that f(E) is just the fractional number of particles in the shower above energy E:

$$f(E_t) = 1/N_e \int_{E_t}^{\infty} dN/dE \ dE \qquad (5.44)$$

where E_t is in MeV. Greisen has parameterized the particle energy distribution function in the form

$$f(E_t) = 2.96 \cdot (\ln E_t)^{-1/2} - 1.136 \qquad (5.45)$$

Substituting this into equation 3.27 above, and dividing up the integration into two parts gives a form for G(E) which numerically is more convenient to calculate, namely

$$G(E_t) = \frac{2.96}{2} \left(\left[\int_{E_t}^{4E_t} \frac{2\delta - m^2 c^4 / E^2}{E \ (\ln E)^{1.5}} \ dE \right] + 2\delta \cdot f(4E_t) \right) \qquad (5.46)$$

Now, the number of direct Cherenkov photons directed at the Fly's Eye is

$$\frac{d^2 N_C}{d\ell d\Omega} = \frac{dN_C}{d\ell} \ \frac{\exp(-\theta/\theta_0)}{2\pi\theta_0 \ \sin\theta} \qquad (5.47)$$

The integration over pathlength and solid angle must be done a bit more carefully for the Cherenkov light due to the rapidly changing angular distribution. Thus,

$$N_{pe}(C) = \iint \epsilon_{det} \frac{d^2N_C}{d\ell d\Omega} \, d\ell d\Omega . \qquad (5.48)$$

The important angular integration part is just

$$I(\theta) = \int_{\theta_{min}}^{\theta_{max}} \frac{\exp(-\theta/\theta_0)}{\sin\theta} \, d\theta \qquad (5.49)$$

The angles θ_{min}, θ_{max} are defined by the boundary of the angular bin. With $G(E)$ and $I(\theta)$ defined, the number of photoelectrons produced from the direct Cherenkov light is written as

$$N_{pe} = \frac{\alpha \cdot \epsilon_{MC} \cdot I(\theta) \cdot A \cdot N_e}{R_p \; c} \sum_{j=1}^{Nwave} (T_F(j) \cdot \epsilon_{PMT}(j) \cdot T_{Atm}(j) \cdot \Delta\nu(j))$$

$$(5.50)$$

where α in this case is the fine structure constant $(^1/_{137})$ and not the scintillation efficiency. Thus the Cherenkov efficiency is expressed as

$$\beta = \frac{\alpha \cdot \epsilon_{MC} \cdot A \cdot G(E_t) \cdot I(\theta)}{R_p \cdot c} \sum_{j=1}^{Nwave} (T_F(j) \cdot \epsilon_{PMT}(j) \cdot T_{Atm}(j) \cdot \Delta\nu(j))$$

$$(5.51)$$

5.4.3.3 The Rayleigh Efficiency (γ)

γ is a calculation of how many Cherenkov photons propagating down the "beam" (i.e., the along the shower

trajectory) that are scattered into a bin's field of view and subsequently detected by the PMT. The Rayleigh transmission factor is calculated using equation 5.19. Here the scattering itself is considered whose cross section has an angular dependence to it.

The distribution of Cherenkov photons that are Rayleigh scattered out of the EAS beam is given by

$$\frac{d^2N}{d\ell d\Omega} = \frac{dN}{d\ell} \frac{3}{16\pi} (1 + \cos^2\theta) \tag{5.52}$$

where the number scattered per unit length depends linearly on the local air density and rather strongly on the photon wavelength.

$$\frac{dN_R}{d\ell} = \frac{\rho(h)\ N}{X_R} (400/\lambda)^4 \tag{5.53}$$

For the isothermal atmosphere,

$$\frac{dN_R}{d\ell} = \frac{\rho_0\ \exp(-h/H_0)\ N}{X_R} (400/\lambda)^4 \tag{5.54}$$

which can be rewritten in the form

$$\frac{1}{N} \frac{dN_R}{d\ell} \Delta\ell = \frac{\rho\ \Delta\ell}{L_R} = \Delta X/L_R \tag{5.55}$$

where the Rayleigh scattering length is

$$L_R = X_R(\lambda/400)^4 \tag{5.56}$$

$$= 1.16 \cdot 10^{-11} \lambda^4 \ (gm \cdot cm^{-2}) \tag{5.57}$$

for λ given nm. The slant depth for the bin is

$$\Delta X = \rho(h) \ \Delta\ell \tag{5.58}$$

It follows from Equation 5.54 that the probability a Cherenkov photon is scattered is given by

$$P_{Rayl}(j) = 1 - \exp \ (-\Delta X/L_R(j)) \tag{5.59}$$

Thus, the Rayleigh efficiency for the bin is

$$\gamma_i = \frac{3 \ \epsilon_{MC} \ A \ (1+\cos^2\theta)}{16 \ \pi \ R_i^2} \sum_{j=1}^{Nwave} (\ \epsilon_{PMT}(j) \cdot T_{Atm}(j) \cdot P_{Rayl}(j) \cdot T_F(j) \ ) \tag{5.60}$$

5.4.3.4 The Aerosol Efficiency (ζ)

The angular distribution of aerosol scattered Cherenkov light is typically divided into two parts in the same form as the Rayleigh scattered light.

$$\frac{d^2N_A}{d\ell d\Omega} = \frac{dN_A}{d\ell} \ \frac{d\sigma(\theta,\phi)}{d\Omega} \tag{5.61}$$

As with the Rayleigh scattered light the probability
the Cherenkov photon is Aerosol scattered can be expressed
in the form

$$P_{Aer}(j) = 1 - \exp(-\Delta X/L_A(j)) \qquad (5.62)$$

$$= 1 - \exp(-\beta(\lambda,h) \cdot \Delta X) \qquad (5.63)$$

This is the general form used by people studying aerosol
scattering.[115] $\beta(\lambda,h)$ is called the turbidity parameter and
as indicated, it depends on wavelength and the height above
the ground. For Rayleigh scattering, the particle size is
small compared to the wavelength. For aerosol scattering,
this mathematical luxury is not necessarily available. In
reality, the amount of photons and the angles at which they
are scattered depends on particle size and shape.

Empirically, $\beta(\lambda,h)$ has a scale height dependence,

$$\beta(\lambda,h) = \beta(\lambda,0) \exp(-h/H_M) \qquad (5.64)$$

with $H_M = 1.2$ km typically. The average value of $\beta(\lambda,0)$ has
been studied extensively throughout the U.S., and a value
for Dugway, Utah is $\beta(\lambda,0) = 0.05$. In fact, the Dugway area
ranks as one of the best places in the U.S. in terms of low
turbidity.

The angular dependence has also been studied, and its
form varies slowly with emission angle over the region where
the aerosol can have a measurable effect on the data (> 5°

viewing angle. For angles less than this, the direct Cherenkov light dominates). We use a form determined by Elterman.[116] The normalized distribution is tabulated in Table 5.1 as a function of viewing angle.

The efficiency for aerosol scattered Cherenkov photons is thus expressable

$$\zeta = \frac{\epsilon_{MC} \ A \ \ d\sigma/d\Omega}{4\pi \ R_i^2} \sum_{j=1}^{Nwave} (\ \epsilon_{PMT}(j) \cdot T_{Atm}(j) \cdot P_{Aer}(j) \cdot T_F(j) \ )$$

(5.65)

All the corrections discussed above strongly dependent on the shower geometry. Figure5.13 shows the relative contributions of the four components for two showers of differing geometries. The direct Cherenkov component is small for showers with $R_p > 1.5$ km.

5.4.4 Size Reconstruction Resolution

With stereo viewing, it is possible to check the shower size reliability. In Figure 4.11, the size "balance" is plotted for bin viewing angles > 40°. This is the difference of the number of electrons detected by FE2 and FE1.

5.5 Shower Longitudinal Profile

The longitudinal profiles detected by the Fly's Eye are fit by both a Gaisser-Hillas equation (3.6) and a gaussian profile of form
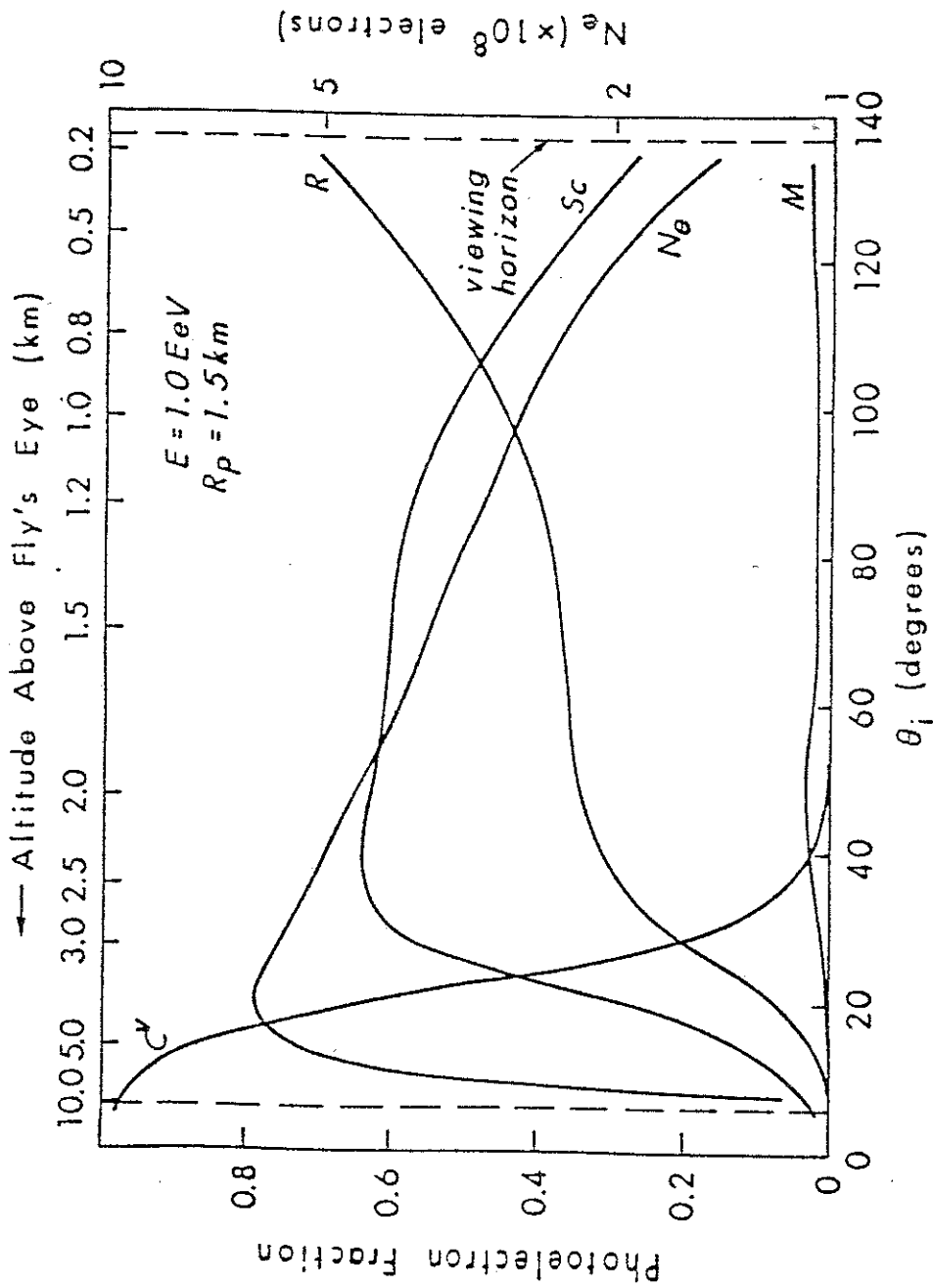
Figure 5.13—The relative photometric contributions of an EAS at (a) 1.5 km, (b) 4.0 km.
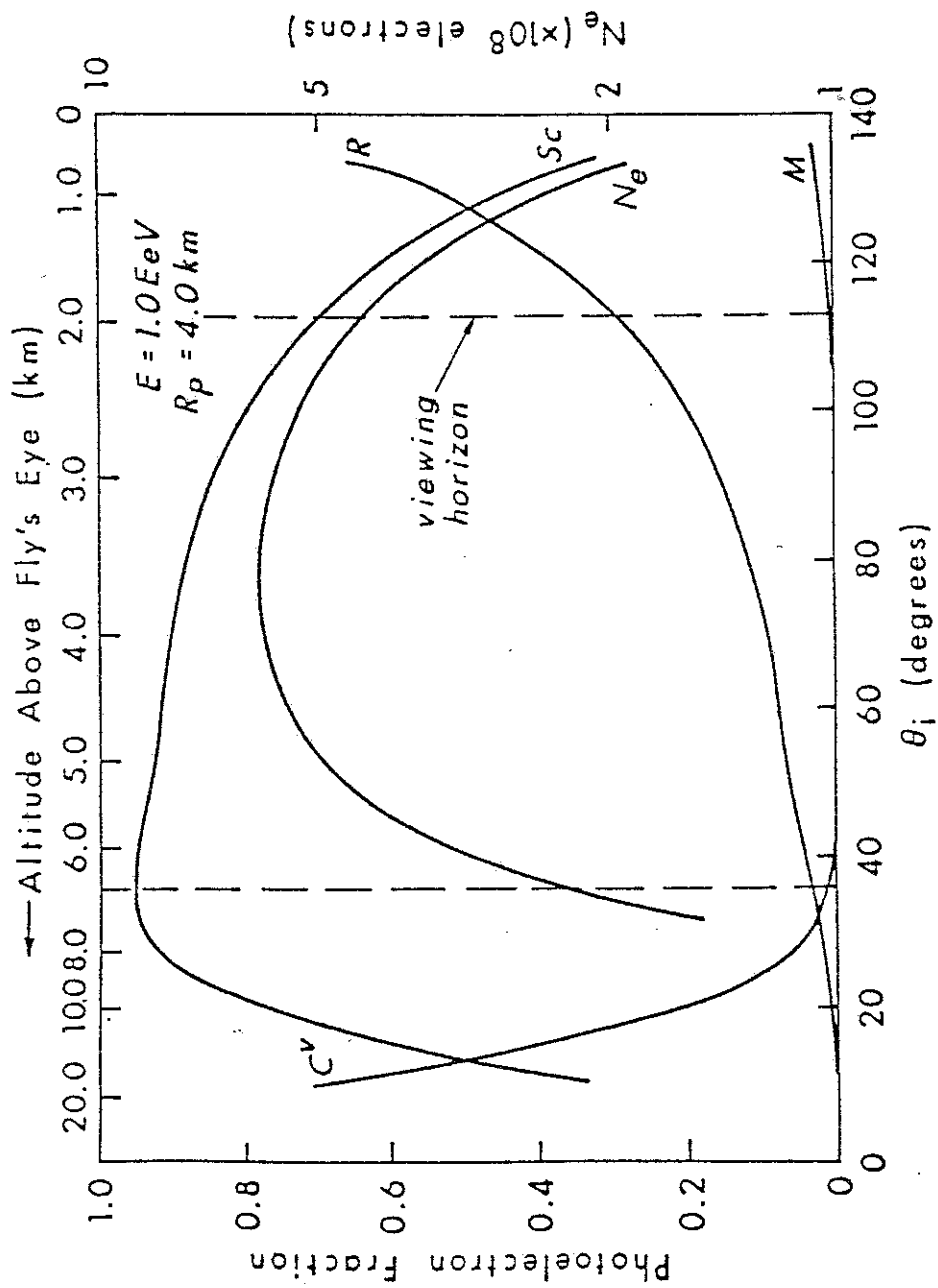
Figure 5.13—(continued)

Table 5.1—Normalized angular distribution aerosol factors.

Emission angle	$d\sigma/d\Omega$	Emission angle	$d\sigma/d\Omega$
5	1.145	95	.0175
10	.836	100	.0151
15	.625	105	.0132
20	.479	110	.0123
25	.370	115	.0112
30	.293	120	.0110
35	.233	125	.0110
40	.184	130	.0110
45	.148	135	.0121
50	.115	140	.0132
55	.090	145	.0151
60	.071	150	.0183
65	.058	155	.0214
70	.047	160	.0258
75	.036	165	.031
80	.030	170	.038
85	.024	175	.045
90	.021	180	.052

$$N_e(X) \; = \; N_{max} \cdot \exp\{ \; -(X-X_{max})^2/(2X_{width}^2) \; \} \tag{5.66}$$

Data from an actual profile is shown in Figure 3.3. Both fits give results which are close to each other differing only slightly. Generally, the gaussian profile has a better reconstruction efficiency, because more of the detected showers will fit to the gaussian profile.

5.6. Shower Energy

The electromagnetic component of the shower energy is found by integrating over the measured longitudinal profile:

$$E_{em} \; = \; \frac{\varepsilon_0}{X_0} \; \int N_e(X) \; dX \tag{5.67}$$

The integral of the gaussian is expressible as

$$E_{em}(Gauss) = \frac{\varepsilon_0}{X_0} (2\pi)^{1/2} N_{max} X_{width} . \tag{5.68}$$

For the Gaisser-Hillas (GH) function,

$$E_{em}(G-H) = \frac{\varepsilon_0}{X_0} \lambda N_{max} \alpha^{-\alpha} e^{\alpha} \Gamma(\alpha+1) \tag{5.69}$$

where $\lambda = 70$ g$\cdot$cm^{-2}, $\alpha = 0.51 \ln(E/\varepsilon_0) - 1$.

Again, differences between the GH and gaussian can be found, though they are reasonably close. Figure 5.14 shows the total energy calculated from GH vs gaussian. The data are well-measured stereo showers. Showers from monocular reconstruction give similar results.

To get the total energy, the Electromagnetic shower energy must be corrected for undetected components. Linsley[117] showed that the undetected energy can be estimated by requiring data from electron arrays and muon arrays be consistent. The Fly's Eye data are consistent with Linsley's supposition.[118] The parameterization can be expressed in the form

$$E_{em} = E_{tot}\cdot(0.99 - .0782\cdot E_{tot}^{-0.175}) \quad (E \text{ in EeV}). \tag{5.70}$$

Table 5.2. E/N$_{max}$ vs. E$_{tot}$ from theory and experiment.

Method	0.01	0.1	1.0	10.0 EeV
EM Cascade	1.12	1.18	1.25	1.31
Gaisser–Hillas	1.13	1.20	1.28	1.34
Linsley	1.06	1.12	1.17	1.22
Measured (1985)	1.11±.09	1.17±.10	1.19±.10	1.20±.10

E$_{missed}$/E$_{tot}$	.01	0.1	1.0	10.0
Linsley	.19	.13	.09	.06
G–H	.31	.27	.22	.18

E$_{tot}$/N$_{max}$	.01	0.1	1.0	10.0
Linsley	1.37	1.34	1.31	1.28
G–H	1.16	1.60	1.53	1.46
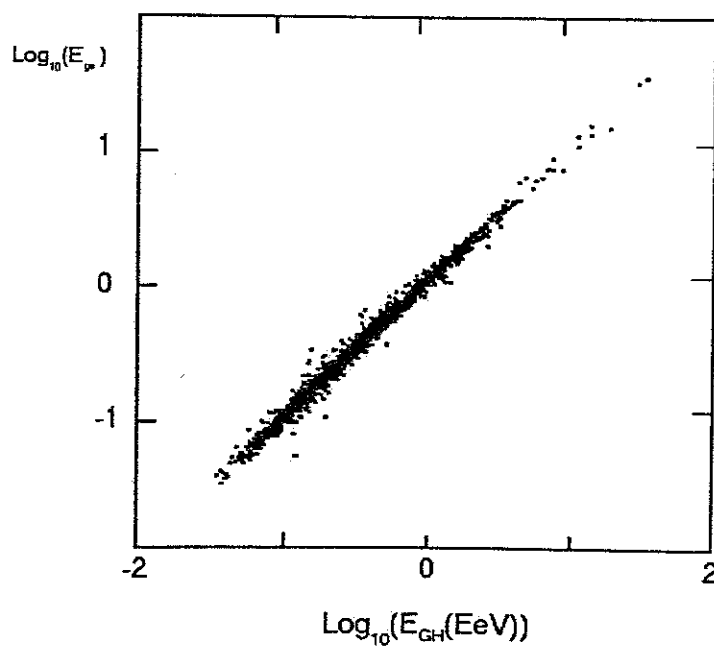
Figure 5.14—A scatterplot of the total shower energy from the integral of the Gaisser-Hillas and Gaussian profiles.

The values of this expression and different theories are tabulated in Table 5.2 along with the empirical data.

With the Fly's Eye detecting showers in coincident with the Michigan Muon array (Chapter 4), it is possible to calibrate the Fly's Eye with ground array parameterizations. Preliminary analysis suggests that the Fly's Eye method is in agreement with the Yakutsk experiment at the 6% level.[119]

5.6.1 Energy Resolution

The energy resolution is estimated from Monte Carlo simulations and checked by comparing the energy from stereo and mono reconstruction. The resolution can be found by comparing input to output energy. The Monte Carlo energy estimation for mono and stereo are plotted in Figures 5.15 along with the estimated error.

In Figure 5.16, the difference between the mono and stereo energy estimation is plotted for coincident showers with $E(STE) > 0.3$ EeV. Further cuts include Track Length $> 40°$, $\delta E/E$(estimated) < 1.0, $\delta X_{max}/X_{max} < 1.0$, $R_p > 1.5$ km, stereo opening angle $> 20°$. These will be the default "tight cuts" used in the spectrum. "Loose cuts" will also be made with only the R_p and Track Length cuts. There is a definite shift between FE1 and stereo data. The difference is due to the geometric shifts that result in an underestimation of both N_{max} and X_{width}. Because this shift is geometrically
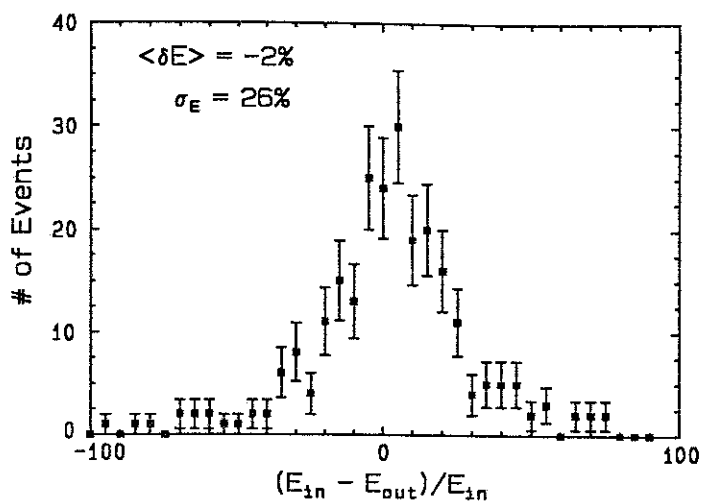
(a)
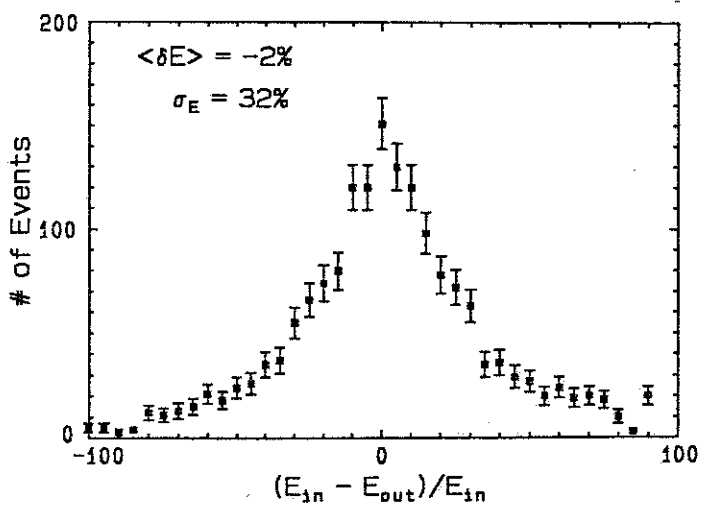
(b)

Figure 5.15—Monte Carlo energy resolution for (a) stereo and (b) mono data. Note that FE1 Monte Carlo data have no geometric induced shift that does exist in the real data.
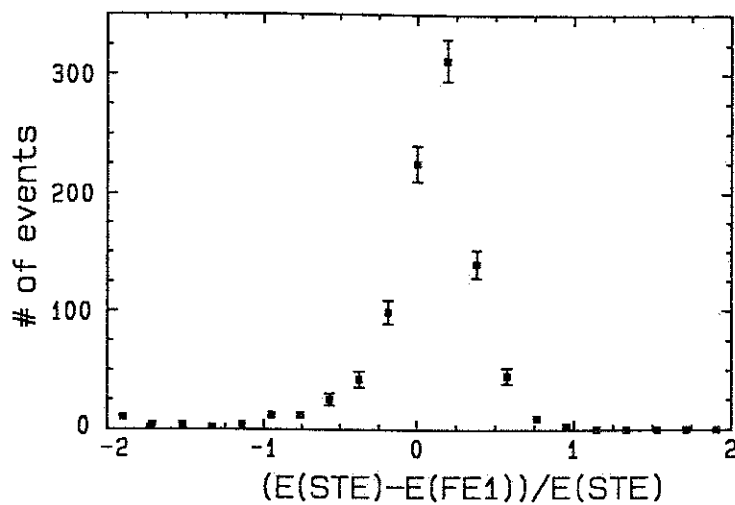
Figure 5.16—Stereo versus FE1 energy for coincident events with E(STE) > 0.3 EeV. The 20% shift is due to geometric differences between timing and stereo reconstruction.
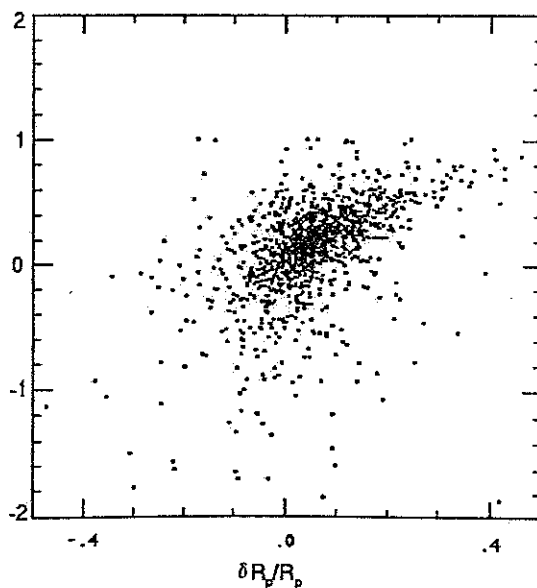
Figure 5.17—$(R_{pSTE}-R_{pFE1})/R_{pSTE}$ vs. $(E_{STE}-E_{FE1})/E_{STE}$ for coincident events with E(STE) > 0.3 EeV.

induced, the FE1 data are rescaled by 20% to agree with the stereo values on average. That this shift comes from a geometric reconstruction error is shown in Figure 5.17 where the Stereo v. FE1 differences in energy and R_p are plotted. There is a clear correlation between the R_p difference and the energy difference.

For completeness, a summary of the energy resolution is presented. The statistical error for showers with E > 0.3 EeV is $\simeq$25% for planer stereo data and $\simeq$30-35% for the FE1 mono dataset. This comes from Monte Carlo simulations, but is consistent with a comparison of FE1 mono and the Planer stereo data. There is a systematic error in the FE1 mono data that artificially reduces the shower energy by 20% relative to the stereo value, but this can be corrected and is corrected on average for the spectrum presented in Chapter 6.

There is a systematic uncertainty associated with the Fly's Eye calibration as discussed in Chapter 4, and it is believed to be $\simeq$ 20% from uncertainties in gains and efficiencies in the system. The other systematics involve unknowns in the EAS, and all experiments to date are sensitive to them. These other uncertainties are the ratio of critical energy to the radiation length ($\simeq$3%), and the undetected component (5-15%) such as muons, neutrinos etc. This latter systematic is corrected for on average, so its net contribution is necessarily smaller. The overall systematic uncertainty is quoted as 25%.

CHAPTER 6

THE ENERGY SPECTRUM

Finally, the energy spectrum is calculated. There are two different data sets from which the spectrum can be determined. They are FE1 monocular data and stereo data. Both groups will be discussed in this chapter. It is possible to construct a FE2 spectrum from its monocularly reconstructed data set, but it is similar to FE1, and the FE2 exposure is smaller, so it will not be discussed.

The spectrum is given by the formula

$$j(E) = \frac{1.}{[\ A\Omega(E)\cdot t]} \cdot \frac{dN}{dE} \tag{6.1}$$

where $A\Omega(E)$ is the energy dependent detector aperture, t is the detector live time, and dN/dE is the differential rate of EASs detected by the Fly's Eye.

The different changes to the Fly's Eye over the years makes the analysis more involved, because the system response is different during different time periods.

The sequence of changes have increased the detector aperture, and, hence, the event detection rate. Figure 6.1 shows the total stereo event rate of air showers above 0.1

Stereo Rate E>0.1 EeV
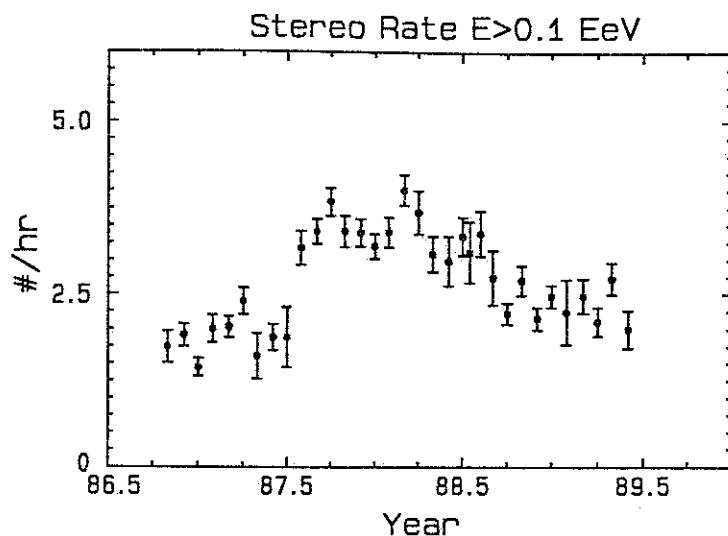
Figure 6.1—The stereo data rates of detected events with energy > 0.1 EeV and with 1.0 EeV. The rates are plotted on a monthly basis to show the near constancy for a given set of running conditions and the difference in observed rate between different running conditions. Events with energy known to within 25% are included.

EeV. From the graph, three distinct sets are present. Noticeable breaks are in August, 1987 and August, 1988.

The changes in the stereo data rate correspond to two of the changes mentioned in Chapter 4: (1) anodized mirror installation, (2) Channel 2 trigger removal at FE1. Other changes made since November, 1986, have had little effect on the apertures. For this reason, only three different apertures are estimated from the Monte Carlos for the stereo data. FE1 data can be broken up into four different

datasets—the three already mentioned, and the set
containing the data taken previous to the UV-pass filter
installation. Table 6.1 gives the dates for these four
datasets, which will be termed Epochs 1-4.

6.1 The Detector live time(s)

FE1 and FE2 running times are based on Enable/Disable
times stored at the beginning and end of nightly data runs.
The stereo running time is found from the overlap of FE1 on
time and FE2 on time with a small ($\approx 5\%$) correction made for
times when the clocks at the two stations were not
synchronized. This is how stereo data are matched in the
reconstruction analysis. The total live times are given in
Table 6.2 with the live times of the FE1 data. We will
further impose to the "tight cuts" described in Chapter 5 a
weather cut to the data. If there were any clouds above the
horizon more than 15°, then the operator marked the data
accordingly. This cut is stringent, because it means the
operator believed there was no significant obscuration in
any direction during the run.

Despite the apparent crudeness of the weather cut,
empirically there is no noticeable difference in event rates
at the 20% level, and the "bad weather" contributes <25% of
the entire dataset. It should also be stressed that the
Fly's Eye was not purposely operated during bad weather, and
thus there was never any period with complete obscuration.

Table 6.1—Dates demarcating the different data sets.

Epoch	Date	Major Change
1	11,81 - 5,85	Pre UV filter
2	11,85 - 6,87	Post UV filter
3	7,87 - 8,88	Anodized mirror
4	8,88 - 5,90	FE1 trigger change

Table 6.2—Detector live times (hours). Different analyses used slightly different data sets. The stereo data set includes data only to 5,89.

Epoch	FE1 (all)	FE1 (good weather)	FE1 (Data)	Stereo (all)
1	1431.4	962.0	2157	—
2	1188.3	608.4	1200	447
3	901.6	626.0	989	825
4	1453.3	874.4	—	610

6.2 Data Determined Aperture Spectrum (FE1)

One difficulty with the Fly's Eye spectrum which ground arrays need not encounter is the determination of the detector aperture. For ground arrays, a well defined fiducial area can be determined from the event core and solid angle distributions. The total area and solid angle coverage are determined by the data for which the incident flux is constant. At a given solid angle bin centered on angle θ, and for a circular radius r_0 over which the core distribution is constant, the detector differential aperture is

$$A \; \delta\Omega \; = \; \pi \; r_0^2 \; \cos\theta \; 2\pi \; d(\cos\theta) \tag{6.2}$$

The $\cos\theta$ term enters in from the array projection along the shower direction.

In contrast, the Fly's Eye's aperture is highly energy dependent, and is distributed asymmetrically towards the Fly's Eye, because showers at the same r_0 and energy may or may not trigger depending on the angle ψ and will have different detected track lengths if they both do. Showers with $\psi < 90°$ will be favored because of track length and attenuation effects. To utilize the full Fly's Eye data set, a detailed Monte Carlo must be used to determine the aperture as a function of energy. This has been done, but as an important check, a spectrum similar to the enclosed ground array method is first presented. It mimics a constant flux analysis a ground array experiment would used if it could determine the shower energy directly.

To determine the aperture for each differential energy bin, data are histogrammed as a function of area and solid angle and intervals in which the flux is constant are thereby determined. As with most data sets, cuts are applied. The "tight cuts" described in Chapter 5 will be used, but a weather cut will not be. Further cuts are $r_0 < 1.5$ km, $\psi < 90°$. This latter cut removes all events landing "in front" of the Fly's Eye. It is equivalent to keeping events with $90° < \gamma < 180°$ where γ is shown in Figure 5.2.

In Figure 6.2, the number of detected EAS per area are plotted as a function of r_0 for the energy bin $0.316 < E$
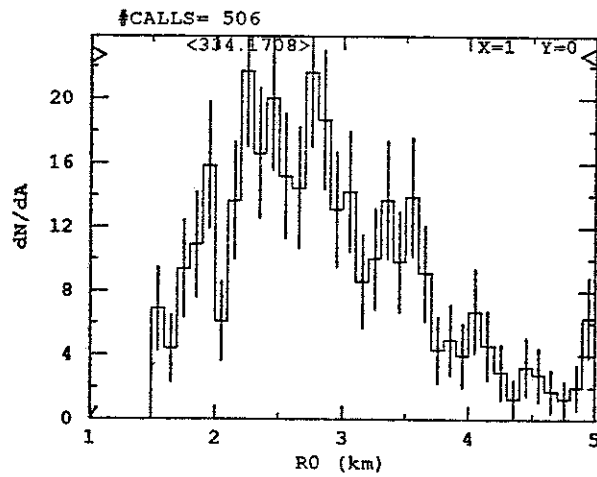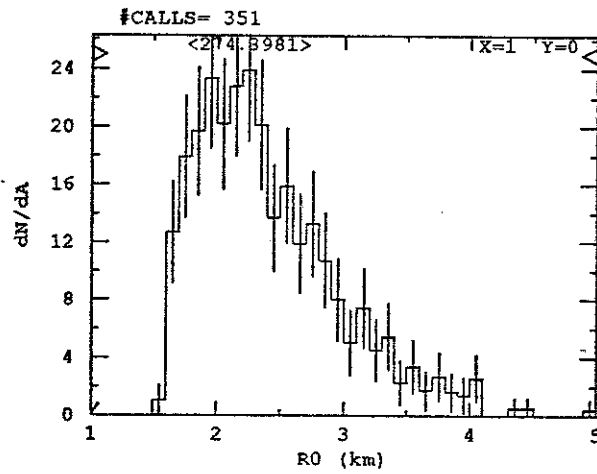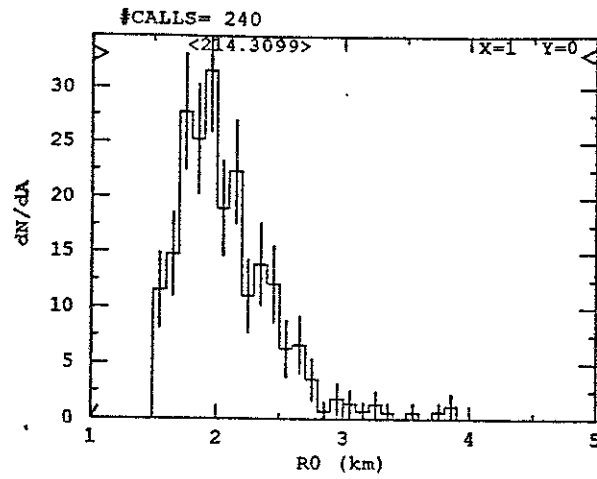
Figure 6.2—Distribution of R_0 in bin .316 <E(EeV) < .422 for (a) Epoch 1, (b) Epoch 2, (c) Epoch 3.

(EeV) < .422 from Epochs 1-3. There is a zenith angle cut of $\cos\theta > 0.75$ as well as the "tight cuts." Figure 6.3 show similar distributions for the energy bin $1.33 < E < 1.78$. The data are weighted by the factor $1/(r_0 \cdot dr_0 \cdot \cos\theta)$. The distribution should be flat for a constant flux and for the lower energy bins that have adequate statistics, one can see there are regions that are constant within statistical fluctuations. The aperture "rise" for small values of r_0 is a result of the $r_p < 1.5$ km cut.

Tables 6.3-6.5 give the data used in determining the data determined spectra for Epochs 1-3 for which multiple cuts could be made. A consistency check is made within each Epoch dataset to test the flux constancy.. Smaller apertures are determined for the lower energy bins by introducing tighter r_0 and θ cuts. The flux values obtained for these energy bins are indeed internally consistent as shown in the table.

At the higher energies, the aperture is kept fixed. The limited statistics preclude obtaining reliable $r_0(max)$ values. However, higher energy showers will provide more light at fixed r_0, so it is a safe assumption independent of any Monte Carlo that the aperture remains constant. The Monte Carlo verifies that the aperture is still increasing at these energies. The data determined aperture spectrum is shown in Figure 6.4. Limited statistics allow no conclusive interpretation above 10 EeV, but this spectrum gives a reliable basis for comparison from the Monte Carlo aperture
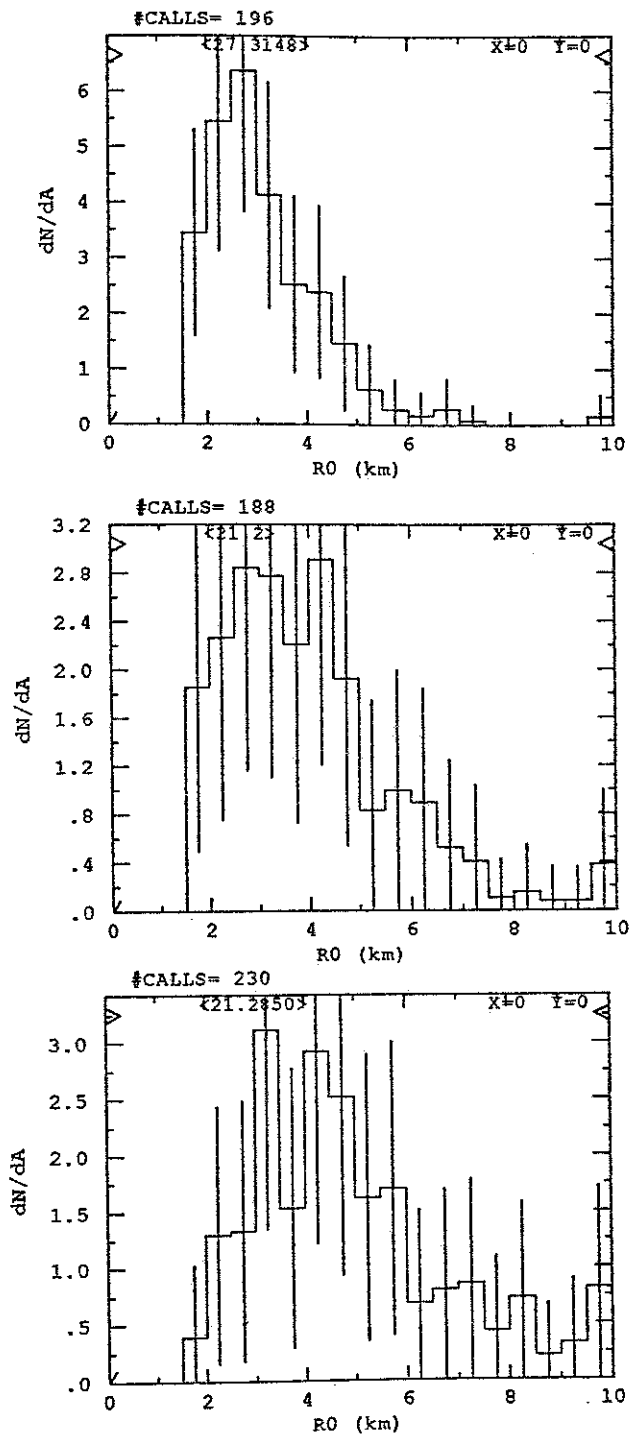
Figure 6.3—Distribution of R_0 in bin $1.33 < E(EeV) < 1.78$ for (a) Epoch 1, (b) Epoch 2, (c) Epoch 3.

Table 6.3—Differential spectral quantities for Epoch 1.

dE (EeV)	r_0 (km)	$\cos\theta$	Aper (km^{2}sr)	N	$J(10^{-30})$ (m^{-2}sr^{-1}sec^{-1}eV^{-1})	$\text{Log}_{10}(E^3J)$
.316-.422	1.6	0.90	.183	7	57.1± 22.	24.46
"	1.8	0.85	1.10	46	54.6± 8.0	24.47
"	2.0	0.85	2.14	89	54.3± 5.8	24.44
.422-.562	1.8	0.90	.812	18	21.7± 5.1	24.41
"	1.8	0.85	1.10	28	24.9± 4.7	24.47
"	2.2	0.85	3.29	76	22.6± 2.6	24.43
.562-.750	2.0	0.80	2.66	30	8.28 ± 1.5	24.32
"	2.5	0.80	6.65	89	9.83 ± 1.0	24.44
"	2.5	0.70	9.06	114	9.24 ± 0.9	24.42
.750-1.00	2.0	0.80	2.66	15	3.11 ± .80	24.43
"	2.5	0.80	6.65	55	4.56 ± .61	24.48
"	2.5	0.70	9.06	70	4.25 ± .50	24.45
1.00-1.33	2.0	0.70	3.40	14	1.70 ± .45	24.31
"	3.0	0.70	16.0	79	2.04 ± .22	24.51
"	3.0	0.60	19.5	86	1.82 ± .20	24.46
1.33-1.78	2.0	0.70	3.40	3	0.54 ± .31	24.51
"	3.0	0.70	16.0	39	0.76 ± .12	24.45
"	3.0	0.60	19.5	48	0.76 ± .11	24.46
1.78-2.37	2.5	0.70	9.05	6	0.36 ± .15	24.09
"	3.5	0.70	24.2	44	0.42 ± .06	24.57
"	3.5	0.60	29.8	52	0.41 ± .06	24.56
2.37-3.16	2.5	0.70	9.05	5	0.058±.026	24.09
"	3.5	0.70	24.2	12	0.086±.024	24.26
"	3.5	0.60	29.8	15	0.088±.022	24.27

Table 6.4—Differential spectral quantities for Epoch 2.

dE (EeV)	r_0 (km)	$\cos\theta$	Aper (km^{2}sr)	N	$J(10^{-30})$ (m^{-2}sr^{-1}sec^{-1}eV^{-1})	$\text{Log}_{10}(E^3 J)$
.178–.237	1.6	0.85	.227	17	292.± 71.	24.42
"	1.8	0.90	.812	61	293.± 38.	24.42
.237–.316	1.8	0.85	1.10	43	114.± 17.	24.38
"	2.2	0.85	3.29	149	132.± 11.	24.45
"	2.2	0.75	4.89	216	129.± 9.	24.43
.316–.422	2.0	0.85	2.14	53	54.3± 7.5	24.43
"	2.2	0.85	3.29	87	58.0± 6.2	24.46
"	2.2	0.75	4.89	117	52.5± 4.9	24.42
.422–.562	2.2	0.85	3.29	38	19.0± 3.1	24.35
"	2.5	0.85	5.22	70	22.1± 2.6	24.42
"	2.5	0.75	7.93	118	24.5± 2.3	24.46
.562–.750	2.5	0.80	6.65	56	10.4 ± 1.4	24.47
"	2.75	0.80	8.99	72	9.88 ± 1.2	24.45
"	2.75	0.70	12.4	99	9.87 ± 1.0	24.44
.750–1.00	2.5	0.80	6.65	30	4.17 ± .76	24.45
"	3.0	0.80	11.5	59	4.73 ± .55	24.50
"	3.0	0.70	16.0	82	4.75 ± .52	24.50
1.00–1.33	3.0	0.70	16.0	34	1.48 ± .25	24.37
"	4.0	0.70	35.6	71	1.38 ± .16	24.34
"	4.0	0.60	41.6	81	1.35 ± .15	24.33
1.33–1.78	3.0	0.70	16.0	20	0.65 ± .14	24.39
"	4.5	0.70	44.3	59	0.69 ± .09	24.42
"	4.5	0.60	55.1	70	0.66 ± .08	24.40
1.78–2.37	3.5	0.70	24.2	11	0.18 ± .05	24.20
"	5.0	0.70	56.2	35	0.24 ± .04	24.34
"	5.0	0.60	70.1	42	0.23 ± .04	24.32
2.37–3.16	3.5	0.70	24.2	7	0.085±.032	24.25
"	5.0	0.70	56.2	20	0.104±.023	24.34
"	5.0	0.60	70.1	26	0.109±.021	24.36

Table 6.5—Differential spectral quantities for Epoch 3.

dE (EeV)	r_0 (km)	$\cos\theta$	Aper (km^{2}sr)	N	$J(10^{-30})$ (m^{-2}sr^{-1}sec^{-1}eV^{-1})	$\mathrm{Log}_{10}(E^3J)$
.133-.178	1.8	0.95	.445	43	713.±109.	24.43
"	1.8	0.90	.812	74	672.± 78.	24.40
.178-.237	2.0	0.90	1.53	85	307.± 33.	24.44
"	2.0	0.85	2.14	124	321.± 29.	24.45
"	2.5	0.85	5.22	276	292.± 18.	24.42
.237-.316	2.2	0.85	3.29	102	129.± 13.	24.44
"	2.75	0.85	7.02	214	126.± 9.	24.43
"	2.75	0.75	10.8	316	122.± 7.	24.41
.316-.422	2.2	0.85	3.29	49	46.3± 6.6	24.37
"	3.0	0.85	8.99	160	55.4± 4.4	24.44
"	3.0	0.75	13.9	237	53.2± 3.5	24.43
.422-.562	2.5	0.85	5.22	45	20.0± 3.0	24.38
"	3.2	0.85	10.7	110	24.0± 2.3	24.46
"	3.2	0.75	16.6	172	24.3± 1.9	24.46
.562-.750	2.75	0.80	9.0	41	8.0 ± 1.2	24.35
"	4.0	0.80	24.0	127	9.3 ± 0.8	24.42
"	4.0	0.70	33.6	174	9.1 ± 0.7	24.41
.750-1.00	3.0	0.80	11.5	26	2.96 ± .58	24.30
"	4.5	0.80	31.5	76	3.16 ± .36	24.33
"	4.5	0.70	44.3	107	3.17 ± .31	24.33
"	4.5	0.60	55.1	128	3.05 ± .27	24.31
1.00-1.33	4.0	0.70	35.6	44	1.22 ± .18	24.29
"	4.5	0.70	44.3	63	1.40 ± .18	24.35
"	4.5	0.60	55.1	77	1.38 ± .16	24.34
1.33-1.78	4.5	0.70	44.3	31	0.52 ± .09	24.29
"	5.0	0.70	56.2	38	0.50 ± .08	24.27
"	5.0	0.60	70.1	52	0.55 ± .08	24.31
1.78-2.37	5.0	0.70	56.2	25	0.25 ± .05	24.34
"	6.0	0.70	83.9	36	0.24 ± .04	24.33
"	6.0	0.60	105.	47	0.25 ± .04	24.35
2.37-3.16	5.0	0.70	56.2	7	0.052±.019	24.04
"	6.0	0.70	83.9	11	0.054±.016	24.06
"	6.0	0.60	105.	20	0.079±.018	24.22

spectrum determined by both the stereo and the FE1 mono datasets.

The spectrum from the combined data sets is given by

$$j = \frac{\sum dN/dE}{\sum [A\Omega(E) \cdot t]} \tag{6.3}$$

where the sums are over the different Epochs. This equation follows directly from 6.1. Table 6.6 tabulates the spectral values from data in Epoch 1-3. The apertures were calculated numerically cut to the $R_p > 1.5$ km cut.

6.3 Monte Carlo Aperture Simulation

The aperture calculation involves simulations by an elaborate Monte Carlo program which models the Fly's Eye detector response. In the Monte Carlo, one-dimensional shower longitudinal profiles are generated according to the Gaisser-Hillas profile with a slight modification to use the observed X_{max} elongation rate instead of the one implicit in the Gaisser-Hillas formulation.

The Monte Carlo assumes an isotropic flux of cosmic rays incident on the top of the atmosphere. From the one-dimensional profile, the number of ionizing particles are determined and the amount of emitted fluorescence and Cherenkov light (both direct and scattered) are calculated and corrected appropriately for the atmospheric attenuation to both FE1 and FE2 as described in Chapters 3 and 5.
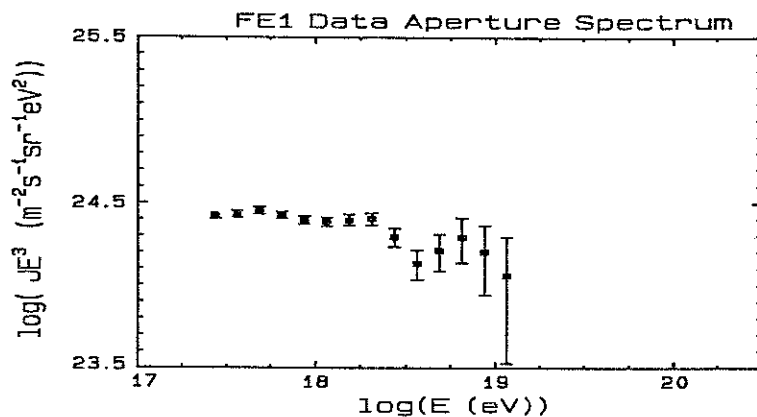
Figure 6.4—The spectrum from the data determined aperture.

Table 6.6—Differential spectrum using the data determined aperture from Epochs 1-3.

dE (EeV)	Exposure (km²sr yr)	N	J(10^{-30}) (m^{-2}sr^{-1}sec^{-1}eV^{-1})	Log$_{10}$(E^{3}J)	
.133-.178	0.078	74	673. ± 78.	24.40	
.178-.237	0.615	337	293. ± 16.	24.42	
.237-.316	1.71	532	124. ± 5.4	24.42	
.316-.422	2.505	443	53.2 ± 2.5	24.43	
.422-.562	3.478	366	23.7 ± 1.2	24.45	
.562-.750	7.030	387	9.31 ± .47	24.42	
.750-1.00	9.600	280	3.70 ± .22	24.39	
1.00-1.33	15.51	244	1.50 ± .10	24.38	
1.33-1.78	18.81	170	0.64 ± .05	24.39	
1.78-2.37	26.61	141	0.28 ± .02	24.40	
2.37-3.16	"	61	0.092±.012	24.29	
3.16-4.22	"	24	0.027±.006	24.13	
4.22-5.62	"	16	0.014±.004	24.21	
5.62-7.50	"	11	.0069±.002	24.29	
7.50-10.0	"	5	.0024±.001	24.20	
10.0-13.3	"	2	.0007±.0005	24.06	
13.3-17.8	"	0	<.00062	<24.37	(90%)
17.8-23.7	"	0	<.00046	<24.62	(90%)

With the known system response, a model pulse is produced and sent through the simulation electronics system. Many detector parameters are necessary for input. These include the gains and efficiencies of the detector along with parameters that specify the OMB signal filter. Most all of these are measured in the laboratory. There is one important "observed" number needed that was not discussed in Chapter 4, and that is the PMT trigger threshold voltage. This voltage is a function of the amount of the night sky background light as well as the gains and efficiencies, and this noise spectrum is difficult and time consuming to calculate. It is easier and probably better to use the actual measured number. For data taken after April, 1988, the tube thresholds were stored every 10 minutes during operation. For data taken before April, 1988, the thresholds were stored for all the tubes which triggered in an event.

As with virtually every Monte Carlo, the aperture Monte Carlo has some simplifications which may affect the aperture calculations. Some of these are the use of system average mirror reflectivity and uniform tube gain for all mirrors and tubes. All thresholds are set to the system average threshold over the Epoch runs. Thus, the Monte Carlo is "starless" and the night sky background is assumed to be constant in time, zenith and azimuth.

Sets of simulated events were produced by the Monte Carlo at 4 energies per decade. An output file was

generated for each set and these simulation sets were then run through the data analysis programs in like manner with the actual data. The reconstruction efficiency is then determined by using the formula

$$A\Omega(E) \; = \; A\Omega_{input} \cdot \frac{(\# \; of \; successes)}{(\# \; of \; trials)} \; . \qquad (6.4)$$

The Monte Carlo can be tested for consistency by comparing the input EAS parameters with the reconstructed parameters and how well it models the different data distributions like R_p, ψ, θ, ϕ, etc. by comparing with the actual data sets. This has been done extensively in the past.[1] The simulated distributions follow the actual distributions quite well. Another sensitive test which will be shown here with the stereo data is to see if the Monte Carlo models the changes in the different epochs.

The stereo and FE1 apertures are plotted in Figure 6.5. A test of the Monte Carlo's sensitivity to changes is possible if one compares the ratio of data rates with the ratio of the apertures. Assuming the incoming cosmic ray flux is constant, then it follows directly from Equation 6.1 that

$$j(E) \; = \; \frac{1.}{[A\Omega(E) \cdot t]} \; \frac{dN}{dE} \bigg|_i \; = \; \frac{1.}{[A\Omega(E) \cdot t]} \; \frac{dN}{dE} \bigg|_j \qquad (6.5)$$

or

$$\frac{dN_i}{t_i} \; \frac{t_j}{dN_j} \; = \; \frac{R(E)_i}{R(E)_j} \; = \; \frac{A\Omega(E)_i}{A\Omega(E)_j} \qquad (6.6)$$
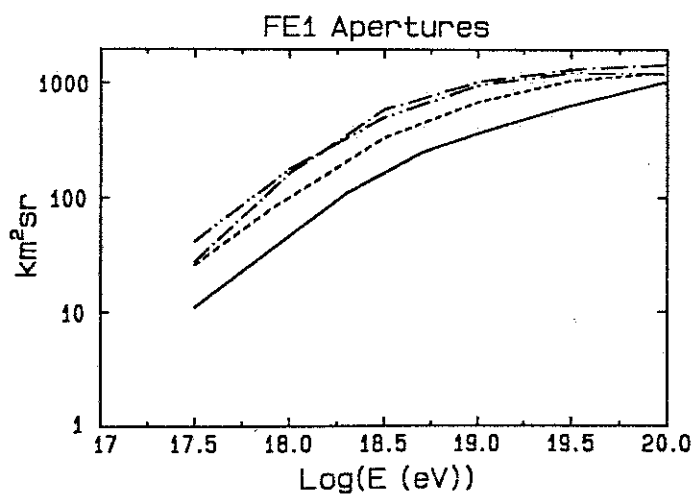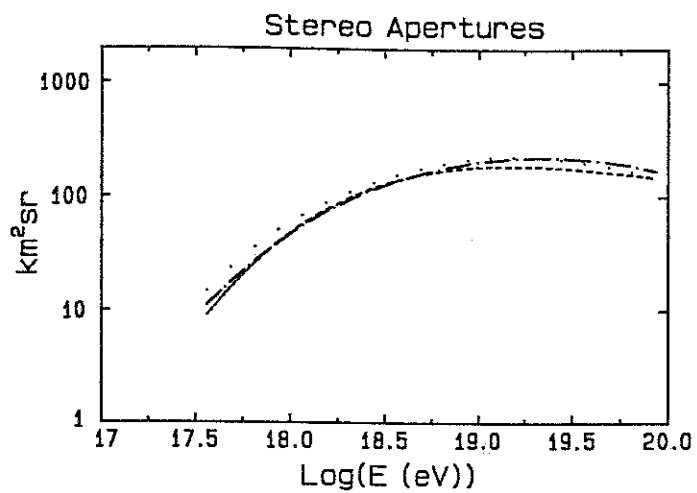
Figure 6.5—Stereo and FE1 Apertures. The dashed line is Epoch 2, the dash-dot-dot line is Epoch 3, and the dot-dash line is Epoch 4. The solid line is for Epoch 1.

where i and j denote any two different epochs. The stereo data rate ratios and aperture ratios are plotted in Figure 6.6 for all three combinations of stereo data used. The data and aperture ratios agree within the statistical uncertainties. In addition, the effect of the detector improvements are seen. The ratio of the stereo data rates between Epochs 2 and 3 increased by 60% at the lower energies, and according to the simulations, the data rate increased approximately 10% at the higher end of the spectrum.

The apparent turnover in Figure 6.5 of the stereo aperture at the highest energies is due to detector saturation. Recall that stereo cannot be used for large R_p because of the "opening angle" problem. The shower-detector planes become degenerate. Thus, there is a maximum distance for stereo fitting, and the showers from 10 EeV primaries will begin to be lost due to saturation. However, these events can be searched for, and no events consistent with E>10 EeV were lost to saturation in the stereo or, for that matter, FE1 dataset.

6.4 The Monte Carlo Aperture Spectrum

The stereo spectrum is shown in Figure 6.6. The numerical values for the number of events, detector exposure and spectrum points for each energy bin are given in Table 6.7. Due to the limited aperture, little significance can be given to the upper end, but the normalization and
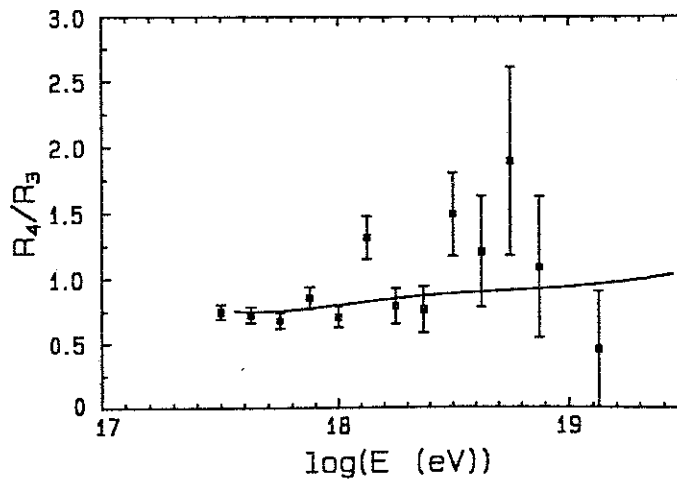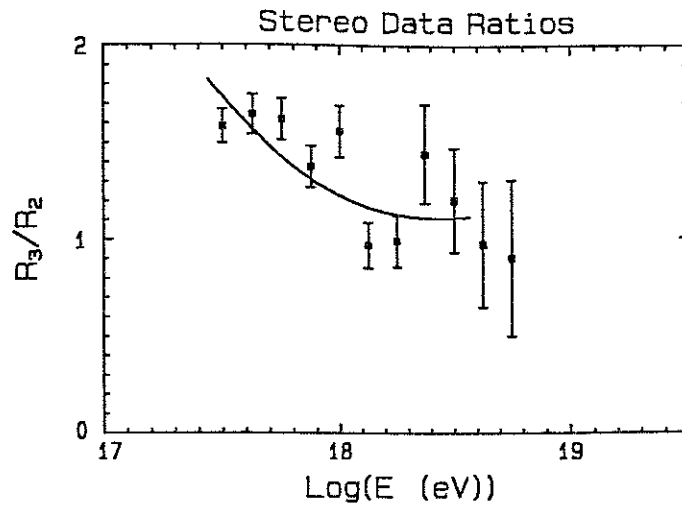
Figure 6.6—Data rate and aperture ratios as defined in Equation 6.6 for the different stereo periods.
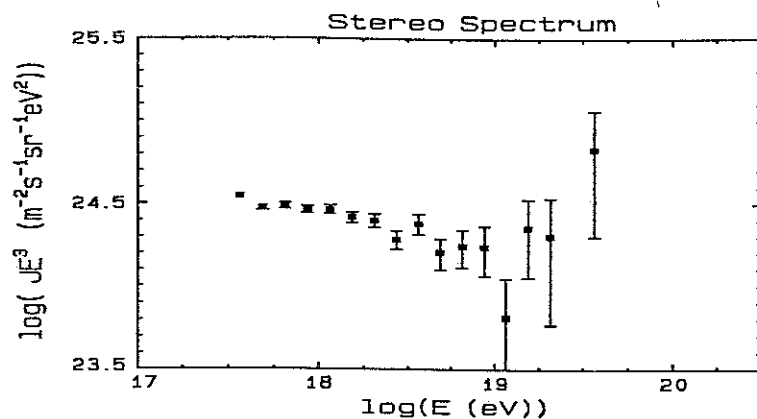
Figure 6.7—The cosmic ray spectrum from FE stereo data and Monte Carlo estimated apertures.

Table 6.7—Differential spectrum from stereo data and Monte Carlo aperture for Epochs 2-4. The quoted errors on the fluxes for bins with a nonzero count are just $\pm N^{0.5}$.

dE (EeV)	Exposure (km^{2}sr yr)	N	J(10^{-30}) (m^{-2}sr^{-1}sec^{-1}eV^{-1})	Log$_{10}$(E^{3}J)	
.316-.422	2.641	616	70.7 ± 2.8	24.539	
.422-.562	4.289	491	25.8 ± 1.2	24.476	
.562-.750	6.856	430	11.1 ± .54	24.483	
.750-1.00	9.562	334	4.45 ± .24	24.462	
1.00-1.33	13.15	249	1.80 ± .11	24.445	
1.33-1.78	17.31	171	0.71 ± .05	24.413	
1.78-2.37	21.90	118	0.30 ± .03	24.400	
2.37-3.16	26.68	61	0.092±.012	24.278	
3.16-4.22	31.53	51	0.049±.007	24.380	
4.22-5.62	35.90	22	0.014±.003	24.205	
5.62-7.50	39.79	15	.0064±.002	24.244	
7.50-10.0	43.04	9	.0027±.0009	24.239	
10.0-13.3	45.17	2	.0004±.0003	23.814	
13.3-17.8	46.21	4	.0006±.0003	24.356	
17.8-23.7	46.16	2	.0002±.0002	24.306	
23.7-31.6	45.88	0	<.0002	<24.61	(90%)
31.6-42.2	43.05	2	.0001±.0001	24.838	
42.2-56.2	31.61	0	<.00016	<25.28	(90%)

spectral slope between $10^{17.5}$–$10^{18.5}$ eV can be calculated with this better set of data. The FE1 spectrum is given in Figures 6.8, 6.9 for "tight" and "loose" cut data, and the values used in obtaining the points in two figures are listed in Tables 6.8 and 6.9.

With the accumulated running time, the stereo present data set now has over twice the number of events used in the original Spectrum analysis with 5382 total stereo events with energies above 0.1 EeV compared to 2408 used in the original Phys. Rev. Lett. paper. However, the spectral distribution is different. The stereo aperture is smaller than the mono aperture and does not grow as fast with Energy.

6.4.1 Spectral Slope

From all three datasets, it is evident that a power law spectrum will fit the data well between $10^{17.5}$–$10^{18.5}$ eV. Table 6.10 gives the least squares fit to the slope to the data.

6.4.2 Cutoff

There are no events above 100 EeV in the largest data set and only four above 56 EeV. The highest Energy events in stereo and FE1 data are 40 and 80 EeV respectively, and thus the data are in agreement with the Greisen-Zatsepin cutoff.

Since some groups have seen a continuation of the spectrum above the cutoff, it is worthwhile to calculate how

Table 6.8—Differential spectrum from FE1 mono data using Monte Carlo apertures for Epochs 1-4. The "tight cuts" were applied.

$Log_{10}E$ (EeV)	Exposure (km^2sr yr)	N	J ($m^{-2}sr^{-1}sec^{-1}eV^{-1}$)	$Log_{10}(E^3J)$
− 0.5	4.98	906	79.4 ± 2.6 (10^{-30})	24.400
− 0.4	7.56	893	41.0 ± 1.4	24.412
− 0.3	13.22	834	17.4 ± 0.60	24.340
− 0.2	18.66	737	$8.64 \pm .32$	24.337
− 0.1	30.23	756	$4.43 \pm .16$	24.338
0.0	39.16	683	$2.41 \pm .092$	24.381
0.1	50.64	528	$1.14 \pm .050$	24.358
0.2	65.24	449	$.599 \pm .028$	24.378
0.3	93.98	356	$.262 \pm .014$	24.318
0.4	116.6	276	$.130 \pm .008$	24.314
0.5	139.4	190	$595. \pm 43.$ (10^{-34})	24.274
0.6	163.9	148	$313. \pm 25.7$	24.296
0.7	191.5	111	$160. \pm 15.2$	24.303
0.8	219.9	81	80.6 ± 8.9	24.306
0.9	248.4	80	55.9 ± 6.2	24.448
1.0	277.2	41	20.4 ± 3.2	24.310
1.1	305.0	31	11.1 ± 2.0	24.347
1.2	331.5	29	7.62 ± 1.4	24.482
1.3	357.4	18	$3.48 \pm .82$	24.442
1.4	382.2	13	$1.87 \pm .52$	24.472
1.5	403.8	9	$.973 \pm .32$	24.488
1.6	423.0	3	$.246 \pm .14$	24.191
1.7	440.6	2	$.125 \pm .088$	24.197
1.8	456.5	0	$<.110$	<24.442 (90%)
1.9	469.5	1	$.0370 \pm .037$	24.268
2.0	479.1	0	$<.0663$	<24.821 (90%)
2.1	483.8	0	$<.0521$	<25.017 (90%)

Table 6.9—Differential spectrum from FE1 mono data using Monte Carlo apertures for Epochs 1-4. The "loose cuts" were applied.

$\mathrm{Log_{10}E}$ (EeV)	Exposure ($\mathrm{km^2 sr\ yr}$)	N	J ($\mathrm{m^{-2}sr^{-1}sec^{-1}eV^{-1}}$)	$\mathrm{Log_{10}(E^3J)}$
− 0.5	8.91	1591	$77.9 \pm 1.9 \ (10^{-30})$	24.392
− 0.4	13.52	1533	39.3 ± 1.0	24.394
− 0.3	19.84	1296	18.0 ± 0.50	24.355
− 0.2	26.80	1111	$9.07 \pm .27$	24.358
− 0.1	46.04	1269	$4.79 \pm .13$	24.380
0.0	59.39	1036	$2.41 \pm .08$	24.382
0.1	77.32	836	$1.19 \pm .04$	24.374
0.2	100.6	700	$.606 \pm .023$	24.382
0.3	147.2	578	$.272 \pm .013$	24.334
0.4	182.6	455	$.137 \pm .006$	24.336
0.5	218.5	307	$613. \pm 35. \ (10^{-34})$	24.288
0.6	255.6	246	$334. \pm 21.3$	24.323
0.7	296.0	189	$176. \pm 12.8$	24.345
0.8	338.2	129	83.4 ± 7.3	24.321
0.9	381.2	131	59.7 ± 5.2	24.476
1.0	424.0	65	21.2 ± 2.6	24.325
1.1	465.2	53	12.5 ± 1.7	24.397
1.2	503.9	39	6.74 ± 1.1	24.429
1.3	540.0	30	$3.84 \pm .70$	24.485
1.4	572.4	14	$1.34 \pm .36$	24.328
1.5	605.6	11	$.793 \pm .24$	24.403
1.6	628.0	7	$.386 \pm .15$	24.387
1.7	656.4	3	$.126 \pm .073$	24.200
1.8	680.2	3	$.0965 \pm .056$	24.384
1.9	697.5	1	$.0249 \pm .025$	24.096
2.0	711.1	0	$<.0294$	$<24.650 \ (90\%)$
2.1	716.4	0	$<.0232$	$<24.846 \ (90\%)$
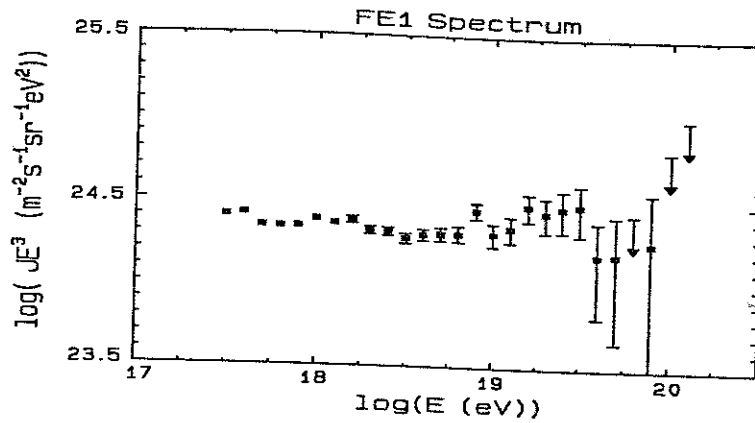
Figure 6.8—The FE1 mono spectrum from "tight cut" data. The inverted triangles represent 90% flux upper limits.
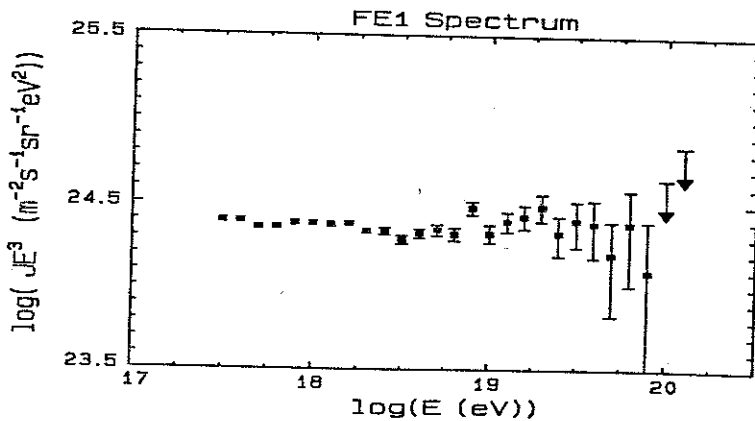
Figure 6.9—The FE1 mono spectrum using "loose" cuts. The inverted triangles represent 90% flux upper limits.

Table 6.10—Best fit slope values from stereo and mono data. The data are fit to a power law spectrum of form $j=aE^{-\beta}$ over the energy range 0.3 EeV − 10.0 EeV.

Data set	$0.3<E<10.0$
Stereo	3.28±.08
FE1 (loose)	3.02±.02
(Epoch 1)	2.93
(Epoch 2)	3.01
(Epoch 3)	3.01
(Epoch 4)	3.08
FE1 (tight)	3.03±.03

many events should have been seen at their flux. Given the Haverah Park Integral flux above 100 EeV of $(3\pm2)\cdot10^{-16}$ ($m^{-2}sr^{-1}s^{-1}$), and the Fly's Eye integrated exposure above 100 EeV, then 6.7 events should have been detected with energy above 100 EeV. The probability of observing no events when six were expected is $3.4\cdot10^{-6}$ or approximately $4^1/_2$ standard deviations.

In contrast to the other measurements, the Fly's Eye data suggest the predicted cutoff is still a possibility. The data are consistent with a cutoff, but a clear cutoff is not yet established. Unfortunately, the Cosmic Ray Composition is not known, so other competing production theories cannot be ruled out.

6.5 Prospects for the Future

The "End" of the spectrum has still not been conclusively demonstrated in over 25 years of experimental

work. The question is what will it take to resolve the issue? The answer is twofold. First, it will take experiments which have a factor of 10-100 larger fiducial area then the present arrays. The detected rate above 10 EeV needs to be > 200 yr^{-1} instead of the current rate of $\approx$20 yr^{-1}. This will require a yearly exposure on the order of 1000 km^2 sr yr! For a Fly's Eye type experiment, the duty cycle forces the design to > 10^4 km^2 sr.

Second, the detector systematics must be understood to better than 1 part in 10^4. It has not been demonstrated that a ground array experiment or a single Fly's Eye (no stereo viewing) can do this. The shower fluctuation problem must be overcome, and the resolution function must be understood to high accuracy.

The advantage of stereo reconstruction has been demonstrated and further work on improving stereo apertures appears to be a worthwhile next step. The stereo baseline needs to resolve showers which are near the necessary 30 km radius. Contrast this with the present 3.4 km baseline with a 10 km radius.

This large volume problem presents many formidable experimental difficulties. One that deserves mentioning is that the 10^4 km^2 sr aperture requirement means showers must be detected and reconstructed > 30 km from this future Fly's Eye. This involves "seeing" into $1^1/_2$ attenuation lengths into the atmosphere. Thus, the attentuation problem cannot

be as simply handled as it can be for the present aperture size. Nightly monitoring is a definite requirement.

For verification of the Greisen cutoff, more knowledge than just a cutoff and pile-up must be observed. The anisotropy must be known with higher accuracy than present to rule out a local galactic production of the highest energy cosmic rays. Further, the composition must be known if the acceleration process is to be understood. The successful Elongation and X_{max} distribution measurements described in Chapter 2 must be further extended to above 10 EeV with higher statistics, and a resolution of $\delta X_{max} < 20$ gm cm^{-2} is required to better isolate the heavy and light elements. A ground array alone will probably not be able to do this.

These are a few of the important issues that must be overcome in the continuing endeavor of searching for the "end" of the cosmic ray spectrum.

APPENDIX

FLY'S EYE DATA TIMING CORRECTIONS

A.1 Introduction

The electronic response of the Fly's Eye is modelled here. Problems arise in relative timing reconstruction of EAS because the time the clock is latched is not the time the EAS photons enter the PMT field of view. Here a model that determines this time correction is described.

The model is based on photographic images of actual mirror spot sizes, measurements taken in the laboratory of the tube-cone response, on-site laser shots whose actual detected pulses were recorded, Monte Carlo calculations of spherical aberation of the mirrors used in the Fly's Eye, and the known electronic properties of the triggering circuitry which reside on the ommatidial board.

A.2 Measurements of the Tube-Cone Response

From photographic measurements of star images on the cluster plane, one can summize that the spot size of a point source for most mirrors is ≤ 1 '. The spot size is defined as the circle in which 90% or more of the light from the source is contained. The remaining light is spread too thinly to be of great importance.

Concurrently, measurements of the tube-Winston cone response were done in the lab. A drawing of the lab arrangement is shown in Figure A.1. A uniform spot of 1.0" diameter was directed onto a phototube coupled to a Winston cone as it is at the Fly's Eye. The source was moved relative to the PMT and the output was recorded along with the coordinates of the beam relative to the tube center.

The relative response of DC light incident on the system is shown in Figure A.2. The sample tube used shows good uniformity, and the rising response of the cone can be seen. Another interesting feature is that the outline of the cone is noticeable.

Difficulty in obtaining good corrections for the slewing time can now be understood. The signal width will depend both on the cone response and the EAS geometry. Signals passing near the tube center will have longer pulses than those passing near the cone edge, plus events at larger distances will have longer pulse widths than those seen from a closer range. Further difficulties arise from the fact that the actual tube crossing center is not known with perfect accuracy, and the distance to the shower is not known perfectly either. When corrections are made to the latch time, it must be based on the current best guess of the geometry. However, if that geometry is not accurately known, the estimated slewing time will be incorrect. Empirically, the iterative process is convergent for most cases.
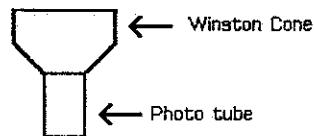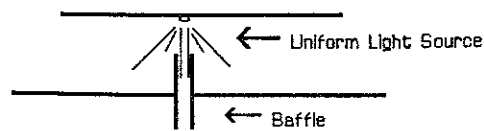
Figure A.1—The experimental setup for the relative response measurement of the PMT-Winston cone. Note that the mirror abberation is not included in this measurement, though the good approximation of a uniform spot is used.

A.3 Field Measurements of Laser Signals

During three different nights of laser calibrations, a storage oscilloscope (GOULD 4074 100 MHz) was used to record the actual signal shapes of laser shots. Many individual tube signals were recorded, and some of them are shown in Figures A.3-A.5. Notice the trapezoidal shape in the majority of the signals. This shape agrees with the tube-cone relative response measured in the lab.

A simple and effective model of the incoming signal can thus be constructed solely from the tube-cone response. It involves a linear rise, a constant width time and a linear fall (Figure A.6). If the signal is close to the detector when one observes an exponential rise and fall of 80 nsec due to the PMT preamp.

```
.0  .0  .0  .0  .0  .0  .0  .0  .0  .0  .01 .03 .03 .01 .0  .0  .0  .0  .0  .0  .0  .0  .0  .0

.0  .0  .0  .0  .0  .0  .0  .0  .01 .01 .3  .3  .3  .3  .01 .01 .0  .0  .0  .0  .0  .0  .0  .0

.0  .0  .0  .0  .0  .0  .0  .01 .3  .3  .5  .65 .65 .5  .3  .3  .01 .0  .0  .0  .0  .0  .0  .0

.0  .0  .0  .0  .0  .03 .2  .3  .4  .5  .7  .81 .81 .7  .5  .4  .3  .2  .03 .0  .0  .0  .0  .0

.0  .0  .0  .01 .2  .3  .5  .6  .7  .8  .89 .9  .9  .89 .8  .7  .6  .5  .3  .2  .01 .0  .0  .0

.0  .0  .2  .25 .3  .5  .8  .8  .9  .9  .99 .99 .99 .99 .9  .9  .8  .8  .5  .3  .25 .2  .0  .0

.0  .1  .25 .3  .6  .8  .8  .9  .99 .99 1.  1.  1.  1.  .99 .99 .9  .8  .8  .6  .3  .25 .1  .0

.0  .15 .3  .6  .8  .8  .9  .99 1.  1.  1.  1.  1.  1.  1.  .99 .9  .8  .8  .6  .3  .15 .0

.0  .15 .4  .7  .8  .9  .99 1.  1.  1.  1.  1.  1.  1.  1.  1.  .99 .9  .8  .7  .4  .15 .0

.0  .2  .5  .7  .8  .9  .99 1.  1.  1.  1.  1.  1.  1.  1.  1.  .99 .9  .8  .7  .5  .2  .0

.0  .2  .6  .8  .9  .99 1.  1.  1.  1.  1.  1.  1.  1.  1.  1.  1.  .99 .9  .8  .6  .2  .0

.0  .2  .65 .87 .94 .99 1.  1.  1.  1.  1.  1.  1.  1.  1.  1.  1.  .99 .94 .87 .65 .2  .0

.0  .2  .65 .87 .94 .99 1.  1.  1.  1.  1.  1.  1.  1.  1.  1.  1.  .99 .94 .87 .65 .2  .0

.0  .2  .6  .8  .9  .99 1.  1.  1.  1.  1.  1.  1.  1.  1.  1.  1.  .99 .9  .8  .6  .2  .0

.0  .2  .5  .7  .8  .9  .99 1.  1.  1.  1.  1.  1.  1.  1.  1.  .99 .9  .8  .7  .5  .2  .0

.0  .15 .4  .7  .8  .9  .99 1.  1.  1.  1.  1.  1.  1.  1.  1.  .99 .9  .8  .7  .4  .15 .0

.0  .15 .3  .6  .8  .8  .9  .99 1.  1.  1.  1.  1.  1.  1.  .99 .9  .8  .8  .6  .3  .15 .0

.0  .1  .25 .3  .6  .8  .8  .9  .99 .99 1.  1.  1.  1.  .99 .99 .9  .8  .8  .6  .3  .25 .1  .0

.0  .0  .2  .25 .3  .5  .8  .8  .9  .9  .99 .99 .99 .99 .9  .9  .8  .8  .5  .3  .25 .2  .0  .0

.0  .0  .0  .01 .2  .3  .5  .6  .7  .8  .89 .9  .9  .89 .8  .7  .6  .5  .3  .2  .01 .0  .0  .0

.0  .0  .0  .0  .0  .03 .2  .3  .4  .5  .7  .81 .81 .7  .5  .4  .3  .2  .03 .0  .0  .0  .0  .0

.0  .0  .0  .0  .0  .0  .0  .01 .3  .3  .5  .65 .65 .5  .3  .3  .01 .0  .0  .0  .0  .0  .0  .0

.0  .0  .0  .0  .0  .0  .0  .0  .01 .01 .3  .3  .3  .3  .01 .01 .0  .0  .0  .0  .0  .0  .0  .0

.0  .0  .0  .0  .0  .0  .0  .0  .0  .0  .01 .03 .03 .01 .0  .0  .0  .0  .0  .0  .0  .0  .0  .0
```
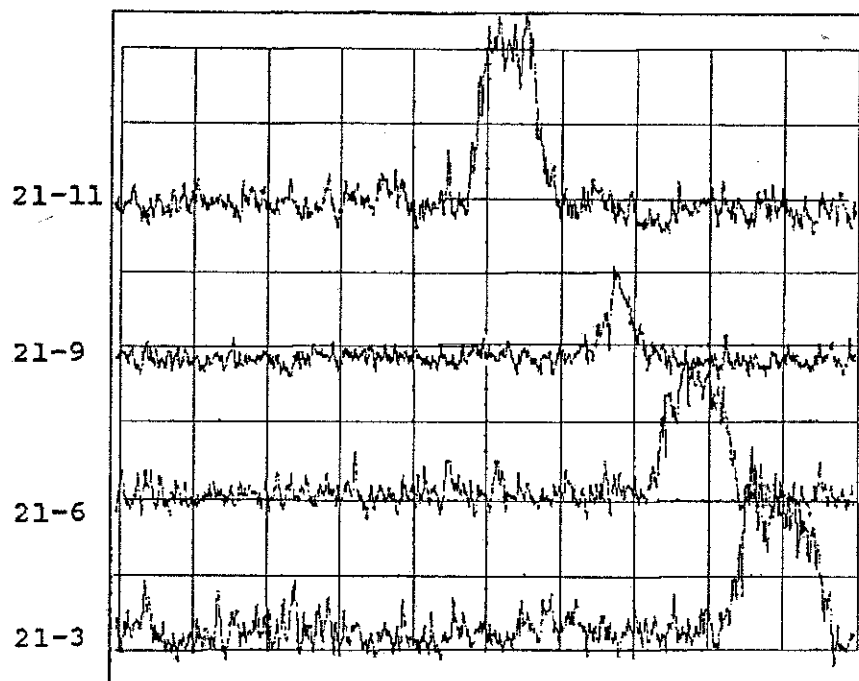
Figure A.2—The smoothed relative response of the tube-cone collector measured in the lab. The values range (in inches) from (-3,-3) to (3,3). The scale is .25" spacing between measurements.

Figure A.3—Scope traces of FE1 PMT signals from a set of laser shots fired on Nov. 23, 1987. The sampled tubes (from Mirror 21) are listed on the left. The geometry for this set (in FE1 coordinates) is R_p=15.6 km, ψ=54.6°. The scales are 5 μsec/division (X-axis) and .2 V/division (Y-axis). The vertical placement of the signals is arbitrary as is the absolute time. The relative time between incoming signals however is correct.
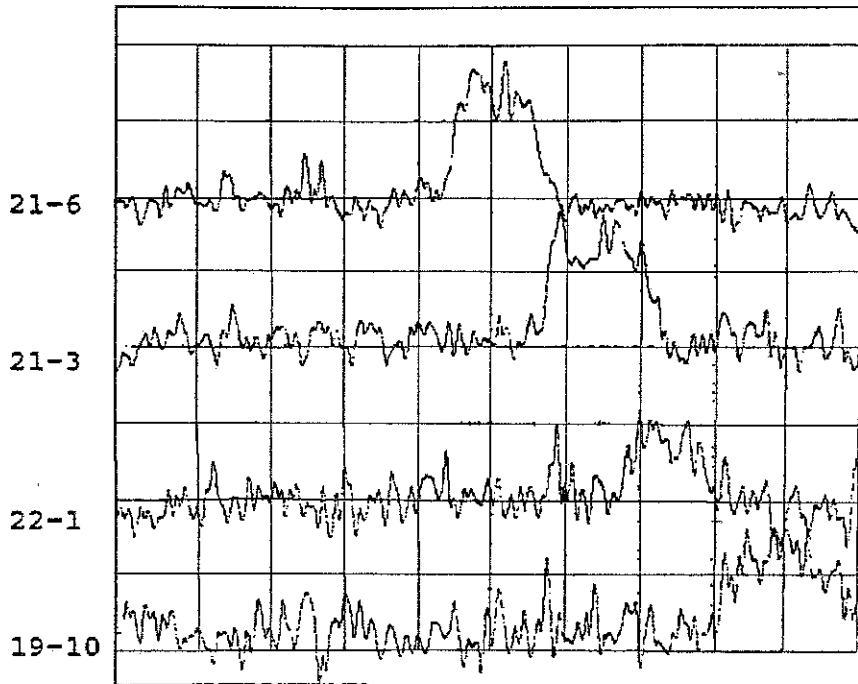
Figure A.4— Scope traces of PMT signals from a set of laser shots with identical geometry as **(A.3)**. The sampled tubes are listed on the left and includes one from the previous scope traces (21-6). The scales are 4 μsec/division (X-axis) and .2 V/division for the top 2 traces and .1 V/division for the bottom 2 traces (Y-axis). As in **(A.3)**, the vertical placement and absolute time of the signals are arbitrary. The relative time between incoming signals however is correct.
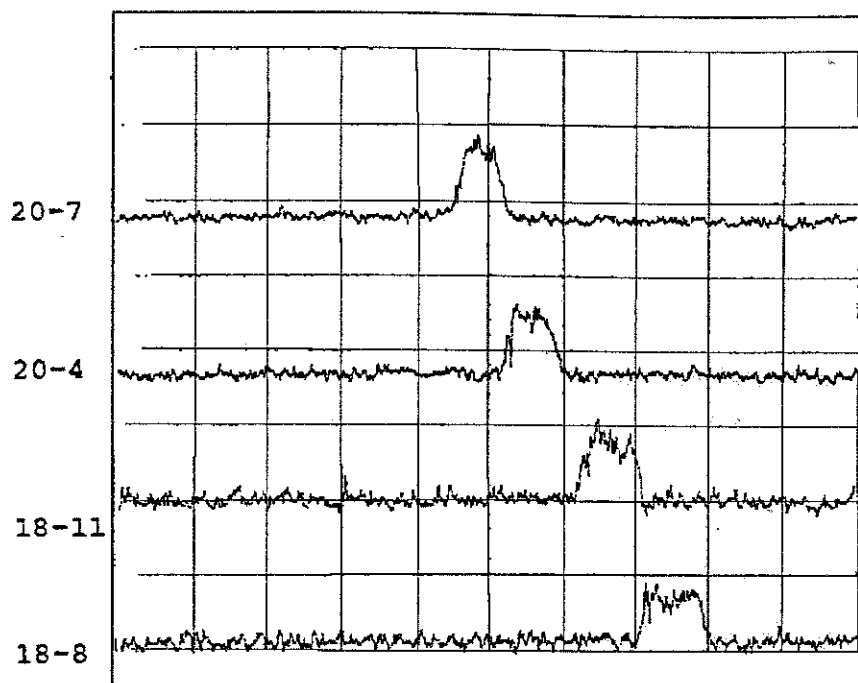
Figure A.5—Scope traces of PMT signals from a set of laser shots. The data were taken Nov. 23, 1987, and the sampled tubes are listed on the left. The geometry for this set (in FE1 coordinates) is R_p=13.3 km, ψ=44.4°. The scales are 5. μsec/division (X-axis) and .5 V/division (Y-axis).

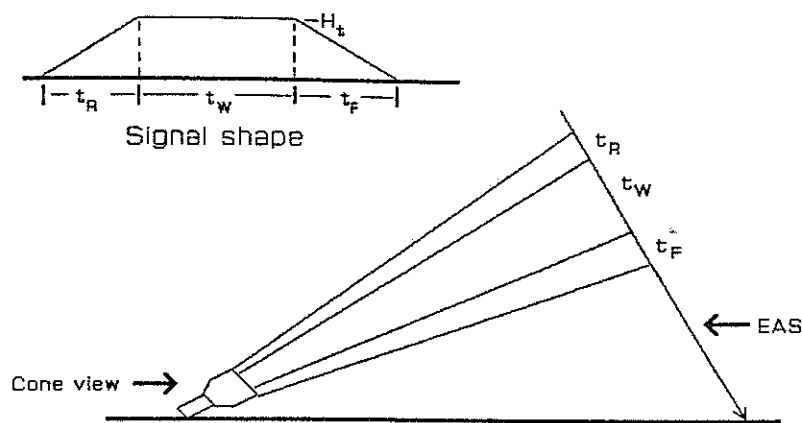**Figure A.6**—The model for the tube output is a trapezoid with rise-time t_R, width-time t_w, and fall-time t_F.

A.4   Time Delay from the OMB Filter

Signals plotted in Figures A.3-5 are those signals entering into the ommatidial board. The signal passes through an amplifier and filtered before it reaches the discriminator (Figure 4.4). The amplifier and filter will change the pulse shape which will affect when the channel fires. The delay time depends on the frequency distribution of the incoming pulse, which depends on the shower geometry, and also on which channel is being considered. Channel 4 filters "harder" than Channel 2, because it has been optimized for signals from more distant showers.

Let us assume the simple outline model described above: the signal has a linear rise (> 80 nsec), a constant width

period, and a linear fall (Figure A.6). The signal fall is not so critical to the triggering time, Presumably it occurs after the tube has fired, though it is important to the estimation of the pulse height, because this part also contributes to the total signal integral. We assume that the signal falls to zero over a time > 80 nsec.

A.4.1 The Pulse Height

To determine when the tube crosses threshold, an estimate of the signal pulse height is needed. This is calculated from the trapezoidal shape and the channel integral. The recorded channel integral is given by

$$I_c = g_{OMB} \cdot H_t \cdot (t_R/2 + t_W + t_F/2) + P_{ed} \qquad (A.1)$$

where g_{OMB} is the ommatidial board gain (channel number dependent), H_t is the plateau signal pulse height, t_R is the signal rise time, t_W is the signal width time, t_F is the signal fall time, and P_{ed} is the Channel pedestal. It is assumed the fall time is the same as the rise time ($t_R = t_F$). The pulse height determined from (A.1) is further amplified by the signal gains of preamps listed in Table A.1. The integrate gains are kept constant to within 5% on a daily basis as a standard diagnostic procedure, while the pedestals for each tube and channel are written to file nightly and the values are used during analysis in the

Table A.1. Ommatidial board parameters which affect the triggering time delay. Included are gains and and filtering time constants for the three triggering channels for the different Calendar dates.

Date	Channel τ_{RC} (nsec)			Amplifier Gain		
	2	3	4	2	3	4
11,81–2,83	150	381	1020	1.0	2.0	3.2
2,83–1,86	150	381	1020	1.0	2.0	2.0
1,86–2,86	150	381	1020	1.0	2.0	3.31
2,86–8,88	150	700	1700	1.0	2.0	3.31
>8,15,88 (FE1)	150	700	1700	0.0	4.7	6.56

calculation of the pulse height. Average pedestal values are 97, 110, and 50 mV for channels 2-4 respectively.

In August, 1988, Channel 2 was removed at FE1 and the input signals were further amplified. In Dec. 1987, the RC filters were removed and replaced with Bessel filters. Values quoted are the "equivalent" RC values.

A.4.2 The Slewing Time

Calculation of t_R, t_W is deferred to Section A.5. The response of the electronic filter is now modelled.

The slewing time is here defined as the time difference between when the source signal enters the electronic filter and when the filtered pulse rises above threshold (the recorded time). The time slewing correction results from two factors. The time is delayed because it takes time for the (unfiltered) pulse to rise up to the threshold value, plus there is a delay from the electronic filter which delays and reduces the signal voltage as it filters out the background.

Without the filter (and without the noise), the delay time would simply be when the linearly increasing voltage crosses threshold as it ramps up to its peak voltage. For the filtered pulses, the voltage equation must be solved to find a better estimate of the time delay. For simplicity, the pulse is divided up into three different time regions demarcated by t_R, t_W, t_F.

For all of the FE2 and most of the FE1 running time, the filters are simple RC filters. The characteristic RC time constants (τ_{RC}) for the different triggering channels are listed in Table A.1. They too are not allowed to vary by more than 5%.

A.4.2.1 $t_{slew} < t_R$

The voltage equation for the signal during the rising section ($t < t_R$) is given by

$$R \cdot \dot{Q}(t) + Q(t)/C = H_t \cdot t/t_R \qquad (A.2)$$

whose solution (by the method of Laplace Transforms) is

$$V(t) = H_t \cdot [t - \tau_{RC} + \tau_{RC} \cdot \exp(-t/\tau_{RC})]/t_R \qquad (A.3)$$

Thus, the filtered signal will reach the discriminator threshold in time t_{slew} given by the equation

$$T_{hresh} \cdot t_R/(H_t \cdot g_{AMP}) + \tau_{RC} = t_{slew} + \tau_{RC} \cdot \exp(-t_{slew}/\tau_{RC}) \qquad (A.4)$$

where g_{AMP} is the OMB amplifier gain preceding the filter.
Values of g_{AMP} are listed in Table A.1. Expression (A.4)
must be solved iteratively. It is simple to check to see if
the threshold voltage is reached before t_R. One enters t_R
into Equation (A.3) above and sees if the filtered voltage
exceeds the threshold. If so, the "slewing" time is
bracketed and now readily found iteratively. Otherwise, the
pulse must be followed further into the "width" or "plateau"
section.

A.4.2.2 $t_R < t_{slew} < t_W$

The driving term for this period is given by

$$V(t) = H_t \cdot [t - U_{tR}(t) \cdot (t - t_R)]/t_R \qquad \text{(A.5)}$$

where $U_{tR}(t)$ is the unit step function beginning at $t = t_R$.
Equation (A.2) with this new driving term has the solution
(again by Laplace Transforms)

$$V(t) = H_t \cdot (1 + \tau_{RC} \cdot \exp(-t/\tau_{RC}) \cdot (1 - \exp(-t_R/\tau_{RC})/t_R) \ . \qquad \text{(A.6)}$$

Setting $V(t) = T_{hresh}/g_{AMP}$ and rearranging to give an
expression for t_{slew},

$$t_{slew} = \ln \left(\frac{\tau_{RC} \cdot (1 - \exp(-t_R/\tau_{RC}))}{t_R \cdot (T_{hresh}/(H_t \cdot g_{AMP} - 1)} \right) \ . \qquad \text{(A.7)}$$

If the threshold is not exceeded during the "width" section,
the pulse is followed into the "fall" section.

A.4.2.3 $t_R + t_W < t_{slew} < t_R + t_W + t_F$

Assuming $t_R = t_F$, the source is given by

$$V(t) = H_t \cdot [t - U_{tR}(t) \cdot (t - t_R) + U_{tW+tR}(t) \cdot (t_W + t_R - t)]/t_R$$
(A.8)

The solution voltage for this section is given by

$$V(t)/H_t = 2 + (t_W - t + \tau_{RC} + \tau_{RC} \cdot \exp(-t/\tau_{RC}) \cdot$$

$$(1 - \exp(-t_R/\tau_{RC}) - \exp(-(t_R+t_W)/\tau_{RC}))/t_R] \quad . \quad (A.9)$$

This expression is messy, but, usually, the only time this formula is used is when t_W is small, and regardless, it is easily accessable by computer. Again, the slewing time is found from (A.9) by setting $V(t)=T_{hresh}/g_{AMP}$ and solving for the time iteratively.

The peak voltage occurs in this final section. Setting $\partial V(t)/\partial t = 0$, the time of the filtered peak signal voltage can be found:

$$t_{peak} = \tau_{RC} \ln[(\exp(t_R/\tau_{RC}) \cdot (1 + \exp(t_W/\tau_{RC})) - 1] \quad .$$

(A.10)

The maximum voltage can be found by inserting this expression for the time in Equation (A.9) above.

Trouble can arise when the signals are near threshold. If the pedestal is slightly incorrect, or the estimated values of characteristic times are miscalculated by either a poor estimate either of either R_p, ψ or of the plane parameters (or both), then it is possible that the modelled signal never crosses threshold! For these tubes, the signal peak time is used for the timing correction. Signals near threshold happen frequently, since for almost every EAS

detected by the Fly's Eye, the photons from ionization increases into and out of the FE signal sensitivity as the shower develops.

A.5 The Circular Cone Model

So far, we have discussed how the signal is modelled after it reaches the OMB. We now discuss how the signal transit times t_R, t_W (it is assumed that $t_F = t_R$) are calculated. The track geometry is needed to find exactly where and for how long the EAS projection crosses and remains inside the cone aperture. This is estimated from the current best geometric fit. The length of the signal times are functions of the radial distance to the shower, R_i, and the angular aperture of the cone. The aperture width is a function of the angle the shower is offset from the tube center (ϕ_{plane}). ϕ_{plane} is the angle between the shower plane normal vector X_n and the tube center direction vector X_i.

$$\phi_{plane} = \cos^{-1}(X_n \cdot X_i) \qquad (A.11)$$

Values for ϕ_{plane} range typically from 87°-93° with 90° being the angle when the plane passes through the tube center. ϕ_{plane} is used to find the angles χ_R, χ_W, the viewing angles of the rising response and uniform response sections of the cone. χ_R and χ_W are then converted into times by the current guess of the shower geometry giving t_R and t_W.

A.5.1 The Model

For simplicity, it is assumed that the cone response is circularly symmetric. Empirically, this is not a too unrealistic assumption, but it must introduce some error at some level in the timing correction.

The values for χ_R, χ_w as functions of ϕ_{plane} were found by estimating the approximate rising response and uniform response angles for a variety of lines crossing the cone at the same distance from the tube center. Good parameterizations for the angles are kurtic gaussians of form

$$\chi_R = \chi_{R0} \cdot \exp(- \alpha_R \cdot \cos^2(\phi_{plane}) - \beta_R \cdot \cos^4(\phi_{plane}))$$

$$\chi_w = \chi_{w0} \cdot \exp(- \alpha_w \cdot \cos^2(\phi_{plane}) - \beta_w \cdot \cos^4(\phi_{plane}))$$

$$\chi_{shift} = \chi_{s0} \cdot \exp(- \alpha_s \cdot \cos^2(\phi_{plane}) - \beta_s \cdot \cos^4(\phi_{plane}))$$

$$(A.12)$$

where the empirically determined values of parameters α, β are given in Table A.2. The values of α, β were found by averaging the values estimated from the tube-cone response measured in the lab which is presented in Figure A.2. The average is over projected azimuthal angles.

Recall from Chapter 5 that the angles χ_i are measured from the projection of the tube center onto the shower plane. The actual point where the shower crosses the cone aperture is generally much earlier than it is from this

Table A.2. Parameters of the winston cone model for the rise, width and shift. $\chi_i = \chi_0 \cdot \exp(-\alpha \cdot \cos^2(\phi_{plane}) - \beta \cdot \cos^4(\phi_{plane}))$.

angle	χ_0	α	β
χ_R	0.80	.131	.026
χ_W	3.91	.043	.0491
χ_{shift}	2.78	.023	.0154

crossing point that the time correction is calculated. So, a correction must be made to account for this angle. Again, an average value for this angle, χ_{shift}, was averaged from the χ_{shift} found for many different projected azimuthal angles of Figure A.2 data.

From geometry, the following times are calculated:

$$t_R = \text{MAX}(\ [R_p \cdot (\tan((\chi_0 - \chi_i - \chi_{shift} + \chi_R)/2)$$
$$- \tan((\chi_0 - \chi_i - \chi_{shift})/2))/c] \ , \ [80 \text{ nsec}] \ )$$

$$t_W = R_p \cdot (\tan((\chi_0 - \chi_i - \chi_{shift} + \chi_R)/2)$$
$$- \tan((\chi_0 - \chi_i - \chi_{shift} + \chi_R + \chi_W)/2))/c \ .$$

$$(A.13)$$

These times are then used in Equations (A.1)-(A.10) above to determine the actual time delay from when the signal pulse enters the cone aperture to when the time is latched. χ_{shift} is incorporated directly as a correction to χ_i which is described in Chapter 5.

A.5.2 Model Tests from Laser Shots

Laser shots are quite useful for checking signal modelling, because the geometric parameters are known. To demonstrate this model is a good fit to the data, model pulses for the signals from the laser shots in Figure A.3-5 are shown in Figure A.7-A.9. In particular, both wide and narrow pulses near the tube center (tube 21-11) and at the edge of the Winston Cone Aperture (tube 21-9) are well modelled.

Further evidence of the model efficacy is shown in Figures A.10 and A.11, which demonstrate the increasing delay in firing times with decreasing signal amplitude. The figures are scatterplots of recorded Channel Integral versus recorded firing time for series of laser shots done at the same geometry (and, hence, constant t_R and t_W). The solid curve gives the model prediction. The times are relative to another tube in the laser's path in the same set of shots. The time corrections for the reference tube is small for all shots in the sample because due to the relatively large signal it received.

An improvement from slewing corrections is a reduction in the difference between the measured and expected entrance angle where the EAS path enters the tube-cone aperture. The quantity

$$\chi_{resid} = \chi_i(\mathbf{X}_i, \mathbf{X}_n) - \chi_i^*(t_i, t_{slew}; R_p, \psi) \tag{A.14}$$
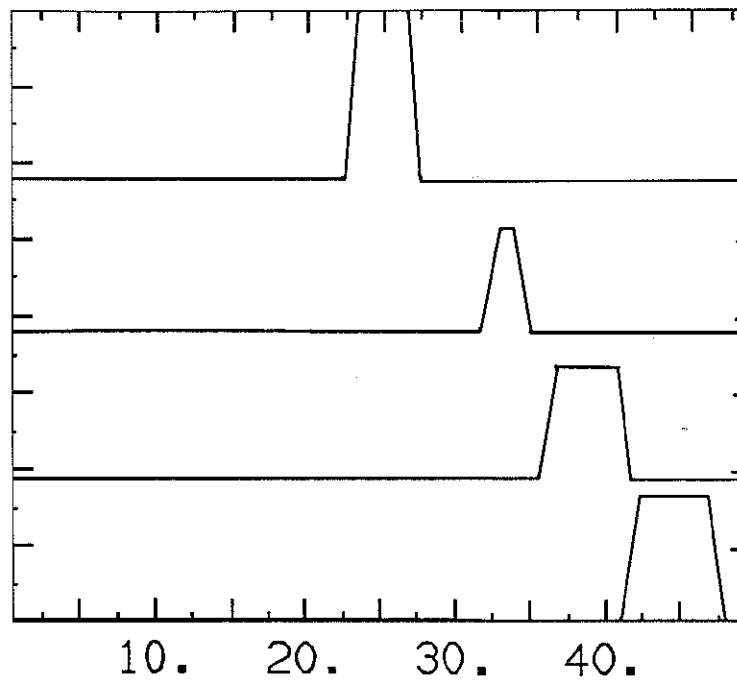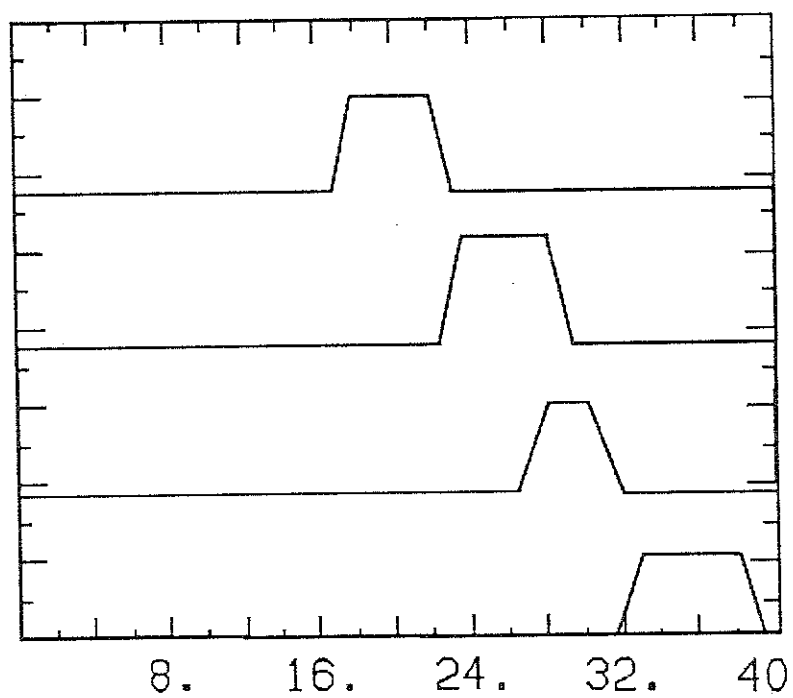
Figure A.7—Model for PMT signals shown in A.3.

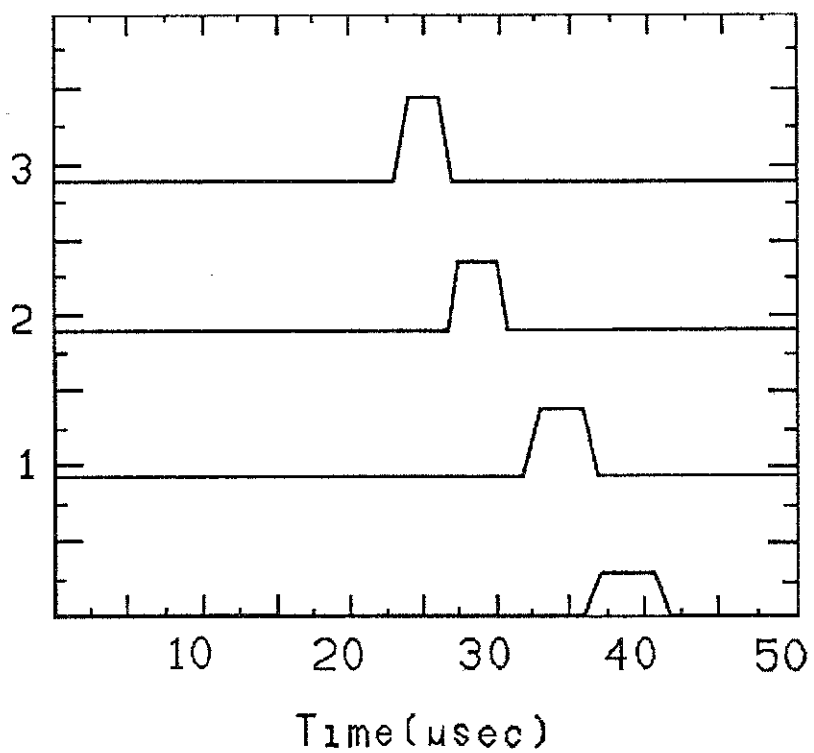Figure A.8—Model for PMT signals shown in A.4.

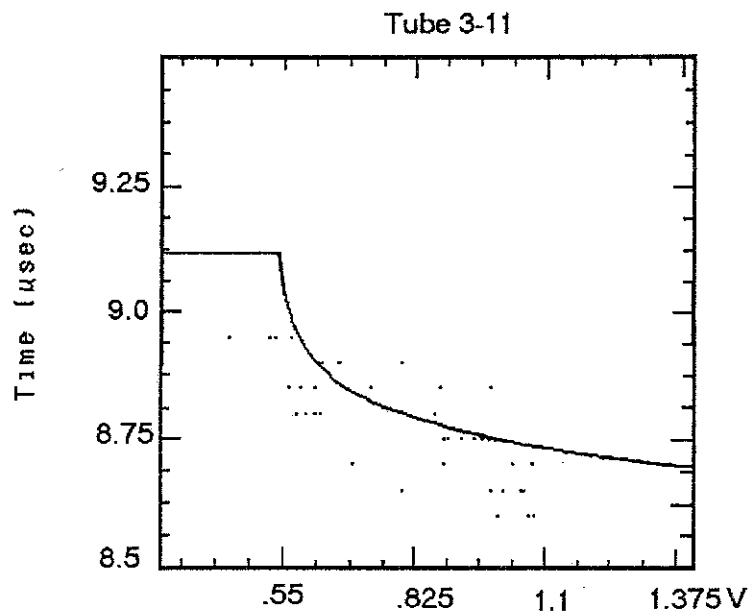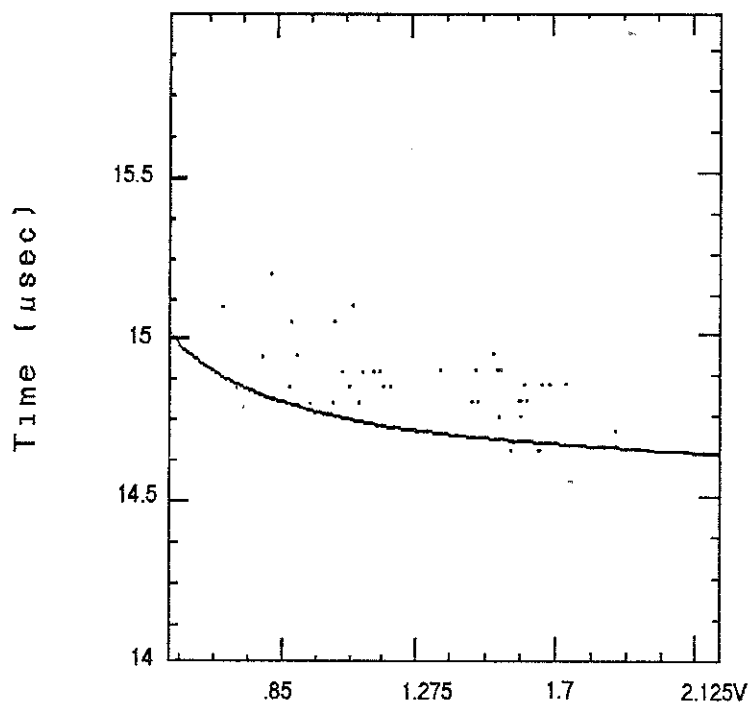**Figure A.9**—Model for PMT signals shown in A.5.

Figure A.10—Scatterplot of Channel 2 Integral vs. Channel triggering time from laser shots at fixed geometry. There is a delay in firing time for smaller Integrals (hence smaller pulse heights). The curve shows the predicted firing time as a function of Channel 2 Integral. The solid line near 9.1 μsec is the time of peak filtered amplitude.

Tube 22-12

Figure A.11—Scatterplot of Channel 2 Integral vs. Channel triggering time from laser shots at fixed geometry. There is a delay in firing time for smaller Integrals (hence smaller pulse heights). The curve shows the predicted firing time as a function of Channel 2 Integral.

is smaller with the timing and angular corrections (see Chapter 5 for calculation of χ_i, χ_i^*). Figure A.12 histograms the value of χ_{resid} for laser shots made during a run in Nov, 1987. The improvement in the angular jitter is from 1.3° to 0.8°.

As discussed in Chapter 4, the time resolution degrades with decreasing signal amplitude. However, this is not seen when one looks over many geometries. The residual error remains essentially constant for different values of (H_t − T_{hresh}/g_{AMP}). In other words, the "fundamental" resolution has not been reached. Further improvement could be made if the true response of each system was better modelled, though this would be a formidable task. It is difficult to envision improvements that are better than the actual mirror spot size some of which are around the 1° level.

A.5.4 Comparison with Flasher Data

The geometric parameters also improve with the new timing corrections. This is demonstrated by flashers. As plotted in Chapter 5, the distribution of $(R_p-R_p(fit))/R_p$ with slewing corrections has virtually no offset, and a width of 5.5% where the $\psi-\psi(fit)$ distribution has a 1.3° width with a small offset of −.3°. If no timing corrections are made, the same R_p distribution has a shift of 1% and a width of 6.4%, but the average and width of the difference in actual and the same fitted ψ distribution is 1.6° and 1.6° width. Thus, modest gains have been made.
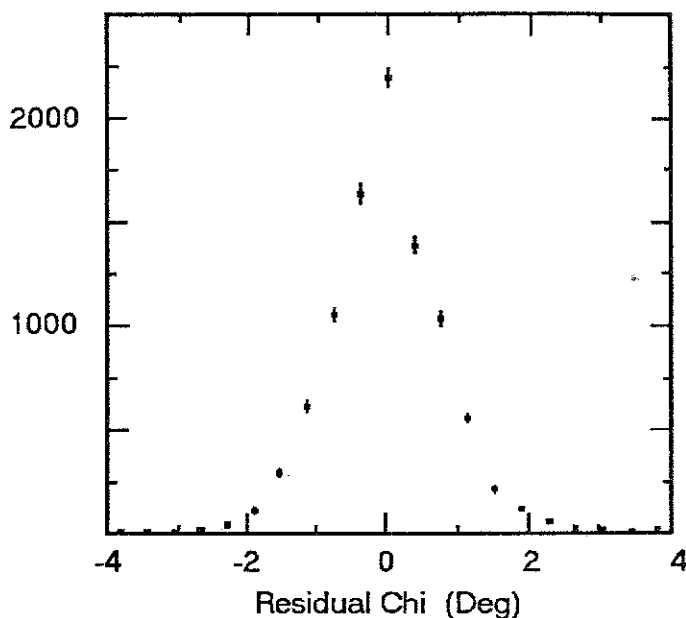
Figure A.12—χ_{resid} for laser shots taken on Oct. 17, 1987. The calculation of χ_{resid} uses the actual R_p, ψ, ϕ_n, θ_n and not the fitted values. The residual distribution shows no improvement with increasing signal amplitude.

A.5.4 Comparison with Stereo Data

Another important comparison is made with stereo data. Figures A.13 - A.15 show N_{max}, X_{max}, X_{width} distributions before and after slewing corrections. The tails in the distributions are tighter with the corrections. From the graphs, it is seen that the systematic shifts between monocular reconstruction and stereo reconstruction are reduced, though there are still small shifts caused by geometric shifts (see Chapter 5). The origins of these remaining shifts are unknown.
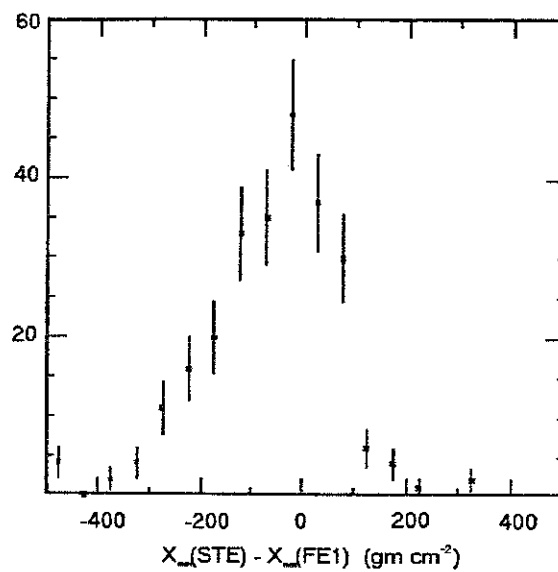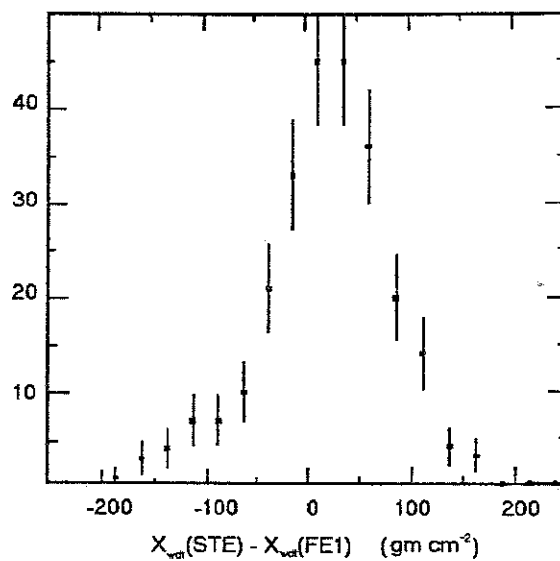
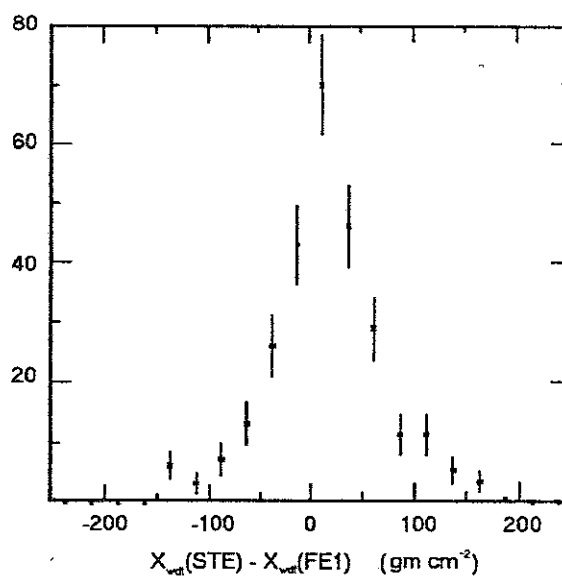(a)
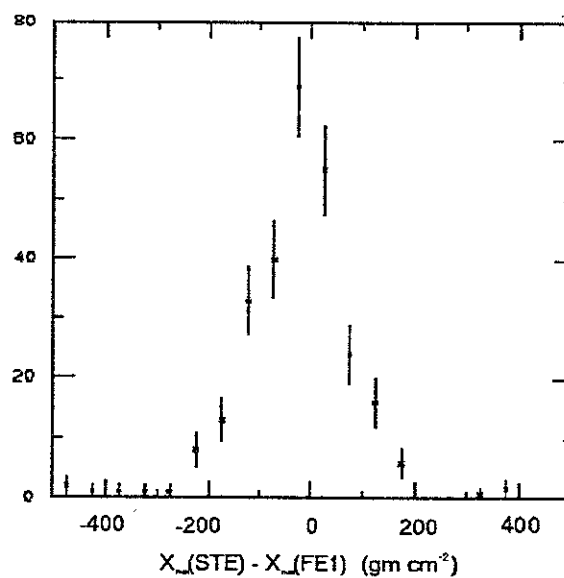
(b)

Figure A.13—Difference in values of X_{max} from stereo and FE1
(a) without the timing corrections. Data are from 11, 1987.
(b) Difference with the timing corrections. The tails are
slightly reduced over uncorrected data.

(a)

(b)

Figure A.14—Difference in values of X_{width} from stereo and FE1 **(a)** without the timing corrections. **(b)** Difference in values of X_{width} with the timing corrections. Data are from 11, 1987. The tails are slightly reduced over non-corrected data.
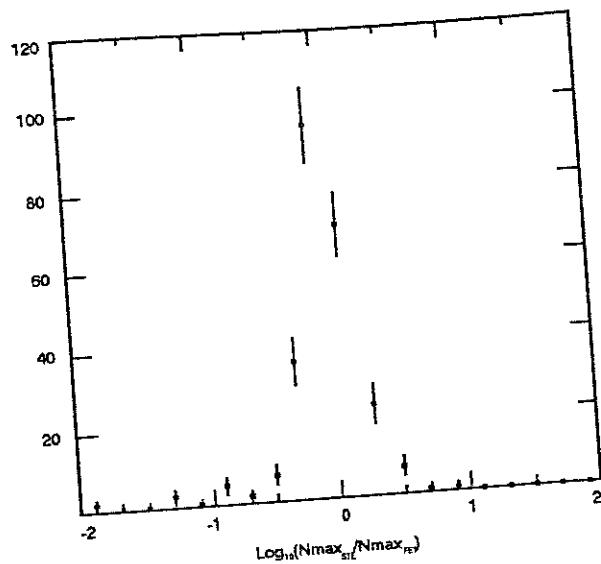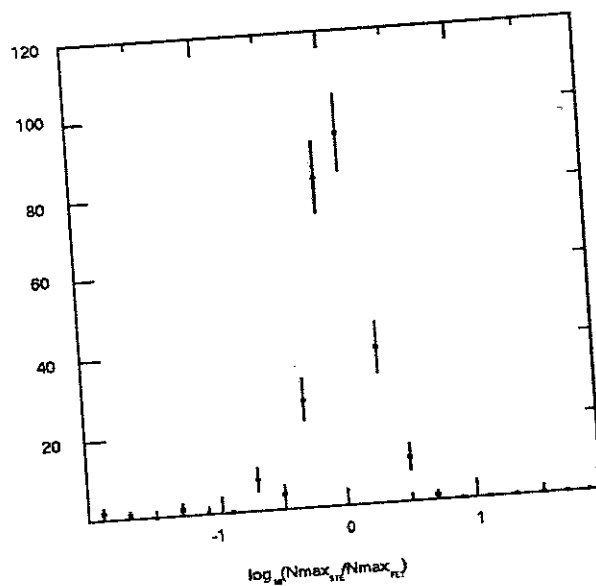
(a)

(b)

Figure A.15—Difference in values of N_{max} from stereo and FE1 (a) without the timing corrections. **(b)** Difference in values of N_{max} with the timing corrections. Data are from 11, 1987. The tails are slightly reduced over non-corrected data.

REFERENCES

[1] Baltrusaitis, R.M., et al., Nucl. Inst. Meth. **A240**, p410, (1985).

[2] Baltrusaitis, R.M., et al., Phys. Rev. Lett. **54**, p75, (1985).

[3] Baltrusaitis, R.M., et al., Proc. 20th ICRC (Moscow), **1**, p409, (1987).

[4] Sokolsky, Intro. to Ultrahigh Energy Cosmic Ray Physics, (Addison Wesley), Chapter 2, (1989).

[5] Kirov, et al., Proc. 17th ICRC (Paris), **2**, p109.

[6] Nagano, et al., J. Phys. G, **10**, p1295 (1984).

[7] Acharya, et al., Proc. 17th ICRC (Paris) **9**, p162 (1981).

[8] Bagge et al., Proc. 15th ICRC (Plovdiv), **12**, p24 (1977).

[9] Khristiansen, et al., Proc 20th ICRC (Moscow), OG5.1-14, (1987).

[10] Aliev, et al., Proc. 19th ICRC (La Jolla), **7**, p191 (1985).

[11] Linsley, Proc. 19th ICRC (La Jolla), **2**, p154 (1985).

[12] Lund, Proc. 20th ICRC (Moscow), **8**, p45 (1987).

[13] Burnett et al., Proc. 21st ICRC (Adelaide), **3**, p101, (1990).

[14] Hillas, Proc. 17th ICRC (Paris) **13**, p69, (1981).

[15] Hillas, Proc. 16th ICRC (Kyoto) **8**, p7, (1979).

[16] Lapointe, et al., Can. J. Phys. **46**, S68 (1968).

[17] Kakimoto, et al., Proc. 17th ICRC (Paris), **11**, p254, (1981).

[18] Baltrusaitis, et al., Proc. 20th ICRC (Moscow), **1**, p409, (1987). ; Baltrusaitis, et al., Phys. Rev. Lett., **54**, p75, (1985).

[19] Khristiansen, G. B., Proc. 19th ICRC (La Jolla), **9**, (1985) ; Glushkov, et al., Proc. 20th ICRC (Moscow), **5**, p494 (1987).

[20] Teshima, M., et al., Proc. 20th ICRC (Moscow), **1**, p404, (1987) ; Teshima, et al., Proc. 21st ICRC (Adelaide), (1990).

[21] Brooke, G. et al., Proc. 19th ICRC (La Jolla), **2**, p150, (1985) ; Cunningham, et al., Astrophys. J., **236**, L71 (1980).

[22] Winn et al., J. Phys. G, **12**, p653, (1986).

[23] J. Linsley, Proc. 19th ICRC (La Jolla), **9**, p475, (1985).

[24] Glushkov, et al., Proc 21st ICRC, **9**, p122, (1990).

[25] P. Sokolsky, Intro. to Ultrahigh Energy Cosmic Ray Physics, (Addison Wesley), Chapter 8, (1989).

[26] Clay, Aust. J. Phys., **40**, p423, (1987)

[27] Cassiday et al., Astrophys. J, (1990), to be published ; Cassiday et al., Proc. 21st ICRC (Adelaide), (1990).

[28] J. Wdowczyk and A. W. Wolfendale, J. Phys. G, **10**, p1453, (1984).

[29] Baltrusaitis, et al., Astrophys. J., **303**, p333, (1986) ; Baltrusaitis, et al., Proc. 20th ICRC (Moscow), **8**, p54, (1987).

[30] Eames, et al., Proc. 19th ICRC (La Jolla), **2**, p254, (1985).

[31] T. Weeks, Physics Reports, **160**, no1,2, (1988).

[32] Nagle, Gaisser, and Protheroe, Ann. Rev. Nucl. Part. Sci., **38**, p609, (1988).

[33] Cassiday et al., Phys. Rev. Lett. **62**, p383, (1989).

[34] Teshima, M., et al., Proc. 21st ICRC, **OG4.1-23**, Adelaide, (1990); Teshima, et al., Phys. Rev. Lett. 64, p1628, (1990).

[35] Lawrence, et al., Phys. Rev. Lett., **63**, (1989) p11.

[36] Simpson, J.A., Ann. Rev. Nucl. Part. Sci., **33**, p323, (1983).

[37] Cassiday et al., Proc. 21st ICRC, Adelaide, **3**, p154, (1990) ; Cassiday et al., Astrop. J., **356**, p669 (1990).

[38] A. A. Penzias and R. W. Wilson, Astrophys. J., **142**, p419, (1965).

[39] P. G. Roll and D. T. Wilkinson, Phys. Rev. Lett., **16**, p405, (1966).

[40] K. Greisen, Phys. Rev. Lett., **16**, p748 (1966).

[41] G. T. Zatsepin and V. A. Kuz'min, Zh. Exsperim. i Teor. Fiz.-Pis'ma Redakt. **4**, p114, (1966). [translation: JETP Lett., **4**, p78, (1966).]

[42] F. W. Stecker, Phys. Rev. Lett., **21**, p1016, (1968).

[43] C. T. Hill and D. N. Schramm, Phys. Rev. D., **31**, p564, (1985).

[44] V. S. Berezinsky and S. I. Grigor'eva, Astron. and Astrophy., **199**, p1, (1988).

[45] J. L. Puget, F. W. Stecker, and J.H. Bredekamp, Astrophys. J., **205**, p638, (1976) (and references therein).

[46] Jokipii, J., and Morphil, G., Astrophys. J., **312**, p170 (1987).

[47] A. M. Hillas, Ann. Rev. Astron. Astrophys. **22**, (1984).

[48] P. Sokolsky, Intro. to Ultrahigh Energy Cosmic Ray Physics, (Addison Wesley), Chapter 7, (1989).

[49] Wdowczyk, J., and Wolfendale, A. W., Ann. Rev. of Nucl. Part. Sci., 1989.

[50] A. Harding, Proc. Workshop on Physics and Exp. Tech. of HE Neutrinos and VHE and UHE Gamma Ray Astrophysics, (ed: G.B. Yodh and D.C. Wold) (1990).

[51] P. Auger et al., Rev. Mod. Phys. **11**, 288-291 (1939) and references therein.

[52] Efimov et al., Proc. 18th ICRC, **EA3-15**, p176, (1983). ; Grigoriev and Efimov, Proc. 18th ICRC, **EA4-4**, p204, (1983).

[53] Baltrusaitis, et al., Phys. Rev. Lett., **52**, p1380, 1984 ; Cassiday et al., Astroph. J., **356**, p669 (1990).

[54] Gaisser and Hillas, Proc. 15th ICRC, Plovdiv, Bulgaria **8**, (1977) p353.

[55] Baltrusaitus et al., Proc. 19th ICRC, La Jolla, **7**, p159.

[56] Gaisser and Yodh, Ann. Rev. Nucl. Part. Sci., **30**, (1980), p475.

[57] Clay and Gerhardy, Austrail. J. Phys., **35**, p59, (1982).

[58] Review of Particle Properties, Phy. Lett. B, **204**, (1988).

[59] Greisen, Proc. 9th ICRC, (1965) p609.

[60] Dedenko and Zheleznykh, Proc. 21st ICRC, **4**, p364 (1990).

[61] Cassiday, et. al, Astrophys. J., **356**, p669 (1990).

[62] Hillas, J. Phys G, **8**, 1982, p1461.

[63] L. Landau and I. Pomeranchuk, Dokl. Akad. Nauk. (USSR) **92**, 535 ; **92**, 735 (1973).

[64] A. B. Migdal, Phys. Rev. **103**, 1811 (1956)

[65] Dedenko and Kolomatsky (Moscow) Preprint.

[66] Rossi, High Energy Particles (prentice-Hall: Englewood Cliffs NJ) (1953).

[67] Particle Data Group, Phys. Lett. B., **204**, 1988, p66.

[68] J. Linsley, 19th ICRC, **7**, p167 (1985).

[69] T.K. Gaisser, Proc. Air Shower Workshop, U of Utah, p57, May 15, 1979 (T.K. Gaisser ed.)

[70] Greisen, Ann. Rev. Nucl. Part. Sci. (1960) **10**, p71.

[71] Kamata and Nishimura, Prog. Theor. Phys., **7**, p185 (1952).

[72] Greisen, Prog. Cos. Ray Physics **3**, (1956) p18.

[73] Greisen (1960), op. cit., p71.

[74] Galbraith and Jelley, Nature, 171, 349-50 (1953)

[75] G. W. Clark, et al., Phys. Rev., **122**, 1961, p637.

[76] J. Linsley, Proc. 19th ICRC, La Jolla, 1985, **9**, p475.

[77] Hillas, Marsden, Hollows and Hunter, Proc. 12th ICRC, **3**, Hobart (1971) p11.

[78] Linsley, Proc. 19th ICRC, **9**, p475 (1985), La Jolla.

[79] Edge et al., J. Phys. A, **6**, p1612 (1973) ; Edge et al., J. Phys. G, **4**, p133 (1978).

[80] Horton et al., J. Phys. G, **12**, p653 (1986).

[81] Khristiansen, Proc. 19th ICRC, La Jolla, **9**, p487, (1985).

[82] M Teshima, et. al, Nucl. Instrum. Methods, **A278**, p399 (1986a).

[83] H Y Dai et al., J. Phys. G, **14**, (1988), p793-805.

[84] Cassiday, et al., Proc. 21st ICRC, **9**, p118 (1990).

[85] Jelley, Cherenkov Radiation.

[86] K. Greisen, Ann. Rev. Nucl. Sci. **10**, (1960)

[87] J. Delvaille, et al., J. Phys. Soc. Japan, **17**, Suppl. A-III, p. 76, (1962).

[88] K. Suga, Proc. 5th Interamerican Seminar on Cosmic Rays, La Paz, Bolivia, vol. **II**, p. XLIX, (1962).

[89] A. E. Chudakov, Proceedings of the 5th Interamerican Seminar on Cosmic Rays, La Paz, Bolivia, vol. II, p.XLIX (1962).

[90] L. G. Porter, et al., Nucl. Instr. Meth, **87**, p87, (1970)

[91] H. E. Bergeson, et al., Phys. Rev. Lett., **39**, p. 847. (1977)

[92] A. N. Bunner, PhD Thesis, Cornell U., Ithaca, NY (1964).

[93] R.W. Nicholls, E.M. Reeves and D.A. Bromley, Proc. Phys. Soc., **74**, (1959) p87.

[94] R.H. Hughes, J.,L. Philpot and C.Y. Fan, Phys. Rev., **123**, p2084, (1961).

[95] O.I. Dozhenko and A.A. Pomanskii, Zh. Eksp. Teor. Fiz. **45**, 268 (1963)[Sov. Phys. JETP **18**, 187 (1964)].

[96] J. Linsley, Proc. 19th ICRC, **7**, p164 (1985).

[97] A.N. Bunner, PhD Thesis, Cornell University, Ithaca, NY (1964).

[98] Ibid, p75.

[99] Ibid, p75.

[100] R. M. Baltrusaitis et al., Nucl. Inst. Meth., **A264**, (1988) p 87.

[101] Baltrusaitis, et al., Proc. 20th ICRC, (1987), **Vol 2**, p 428.

[102] Dave Steck, Master's thesis (unpublished), University of Utah (1986).

[103] J.W. Elbert, private communication.

[104] D. Sinclair, Nucl. Inst. Meth, **A278**, 583 (1989).

[105] This and the next section are based on a series of notes written by George Cassiday detailing the calibration procedures.

[106] Baltrusaitis, et al., J. Phys G. (1985)

[107] Ong et al., Nucl. Phys B., **14A**, p273, (1990).

[108] This section based in part on unpublished notes by George L. Cassiday. (UU-Note, 1984)

[109] Dalquist, Bjorck, Anderson, Numerical Methods, (Prentice Hall), p209, (1974).

[110] Bevington, Data Analysis for Scientists and Engineers, McGraw-Hill p204, (1969).

[111] Press et al., Numerical Recipes, (Cambridge Press), p290, (1986).

[112] This section based in part on unpublished notes by J. Elbert and P. Sokolsky. (UU-Note, 1980)

[113] Haymes, Introduction to Space Science, (John Wiley, N.Y.), pp54-90 (1971).

[114] J.W. Elbert, T. Stanev and S. Torii, Proc. 18th ICRC, Bangalore, **6**, (1983), p227.

[115] Flowers, E.C., et al., Journ. Appl. Meteor., **8**, p955 (1969).

[116] Eltermann, L., Atmospheric attenuation model, Air Force Publication # AFCRL 64-740, (1964).

[117] Linsley, Proc. 18th ICRC, Bangalore, Rapporteur, (1983).

[118] Baltrusaitis, et al., Proc. 19th ICRC, **7**, p159, (1985).

[119] Cassiday, et al., Proc. 21th ICRC, **9**, p118, (1990).